Mechanochemical fabrication of ZnO nanoparticle inks for eco-friendly low-cost thin film environmental sensors

By

Gibson Asumani Boakye

B.Sc., Kwame Nkrumah University of Science and Technology, 2022

A Thesis Submitted in Partial Fulfillment of the

Requirements for the Degree of

MASTER OF APPLIED SCIENCE

in the Department of Electrical & Computer Engineering

University of Victoria

We acknowledge and respect the Lək̓ʷəŋən (Songhees and Xʷsepsəm/Esquimalt) Peoples on whose territory the university stands, and the Lək̓ʷəŋən and W̱SÁNEĆ Peoples whose historical relationships with the land continue to this day.

Supervisory Committee

Mechanochemical fabrication of ZnO nanoparticle inks for eco-friendly low-cost thin film environmental sensors

By

Gibson Asumani Boakye

B.Sc., Kwame Nkrumah University of Science and Technology, 2022

Supervisory Committee

Dr. Christo Papadopoulos, (Department of Electrical & Computer Engineering)

Supervisor

Dr. Tao Lu, (Department of Electrical & Computer Engineering)

Departmental Member

Abstract

Supervisory Committee

Dr. Christo Papadopoulos, (Department of Electrical & Computer Engineering)

Supervisor

Dr. Tao Lu, (Department of Electrical & Computer Engineering)

Departmental Member

The increasing demand for low-cost, scalable, and energy-efficient sensing technologies has driven significant interest in nanomaterial-based thin film sensors. This thesis presents the fabrication and characterization of zinc oxide (ZnO) nanoinks via a low processing temperature mechanochemical planetary ball milling (PBM) approach for the fabrication of eco-friendly, flexible, and low-cost gas sensors. The study focuses on establishing a low input energy, simple and scalable solution-based process that enables the direct conversion of bulk ZnO powder into functional nanoinks suitable for thin film deposition. ZnO nanoinks were prepared through wet ball milling under varying conditions, including milling speed 200 rpm to 1000 rpm, time 10 minutes to 120 minutes, and solvent type (DI water, ethylene glycol and Isopropyl alcohol), to investigate their influence on nanoparticle size, morphology, and dispersion. Thin films were subsequently fabricated by deposited the nanoinks onto a wide range of low-cost substrates including glass slide, filter, plain and lined paper, plastic polymer, foil, ceramic and flexible materials using an adjustable blade applicator technique to form films with controlled thickness (15 μm to 50 μm) and uniformity. The versatility of substrate selection highlights the potential for low-cost and flexible sensor fabrication. Material characterization was conducted using techniques such as scanning electron microscopy (SEM), transmission electron microscopy (TEM), atomic force microscopy (AFM), Raman spectroscopy, ultraviolet–visible (UV–Vis) spectroscopy, and energy dispersive X-ray spectroscopy (EDX), confirming the formation of nanoscale ZnO. Variations in milling conditions were observed to affect particle size, dispersion, and film morphology. Initial gas sensing measurements of the fabricated ZnO thin films on different substrates was evaluated under various conditions, including different gas species (Hydrogen, dry air and argon), gas concentrations (low and high), and different flow systems (static and continuous flow) at room temperature. The sensors demonstrated measurable and reproducible responses across both low and high gas concentrations, with response magnitude increasing as gas concentration increased. These results represent a proof-of-concept for room-temperature sensing using solution-processed ZnO films. The data indicated that sensors milled at 200 rpm had response times of 610–750 seconds under static flow, and 750 rpm sample reaches about 2100 seconds under continuous flow. Recovery times were generally faster with less variations, 560–660 seconds for most samples. Glass-based films generally exhibited quicker response and recovery kinetics than paper-based substrates. The sensing mechanism may be attributed to surface adsorption and desorption processes involving oxygen species, which modulate charge carrier concentration and electrical conductivity upon exposure to target gases. This work demonstrates that PBM-fabricated ZnO nanoinks enable low-cost, scalable fabrication of flexible thin film gas sensors. The preliminary gas sensing results provide insight into how processing conditions influence material properties and sensing behavior, highlighting potential for environmental, industrial, and wearable sensing applications.

Table of Contents

List of Tables

List of Figures

List of Acronyms

AFM – Atomic Force Microscopy

ATP – Adenosine triphosphate

CNTs – Carbon nanotubes

CPU – Central processing unit

CVD – Chemical vapor deposition

DFT – Density-functional theory

DI – Deionized

DOS – Density of states

EDX – Energy-dispersive X-ray

EG – Ethylene Glycol

FESEM – Field Emission Scanning Electron Microscopy

FET – Field effect transistor

ICs – Integrated circuits

IPA – Isopropyl Alcohol

ITO – Indium Tin Oxide

ITRS – International Technology Roadmap for Semiconductors

JFET – Junction field-effect transistors

LOD – Limit of Detection

LSI – Large scale integration

MBE – Molecular Beam Epitaxy

MEMS – Micro-electromechanical systems

MFC – Mass flow controller

MOS – Metal-oxide-semiconductor

MOSFET – Metal-oxide-semiconductor field effect transistor

No_x – Nitrogen oxides

NT – Nanotubes

PBM – Planetary Ball Milling

PLD – Pulsed Layer Deposition

PVD – Physical vapor deposition

QD – Quantum dot

RH – Relative humidity

RMS – Root-mean-square

SCS – Semiconductor Characterization System

SD – Sputter deposition

SEM – Scanning Electron Microscope

SMO – Semiconductor Metal Oxide

SMU – Source measure unit

STM – Scanning tunneling microscope

TEM – Tunneling Electron Microscopy

UV – Ultraviolet light

UV-Vis – Ultraviolet and Visible light

VOCs – Volatile organic compounds

WHO – World health organization

0D – Zero-dimensional

1D – One-dimensional

2D – Two-dimensional

3D – Three-dimensional

Acknowledgements

I would like to sincerely thank my supervisor, Dr. Chris Papadopoulos, for his continuous guidance, support, and mentorship throughout my graduate studies. His dedication and encouragement played a crucial role in making this journey both meaningful and rewarding.

I am also grateful to Dr. Tao Lu for serving on my supervisory committee and for his valuable time, insights, and constructive feedback.

I would like to extend my appreciation to my fellow researcher, Dr. Anusha Venkataraman, for her support, collaboration, feedbacks and assistance in this research.

Lastly, I am deeply thankful to my family for their unwavering support, patience, and encouragement, which made this work possible.

This research is supported with funds from WorkSafeBC. The views, findings, opinions and conclusions expressed herein do not represent the views of WorkSafeBC.

Chapter 1

1. Introduction

1.1 Background and Motivation

Nanotechnology has become a central area of research in modern materials science due to its ability to enable the design and development of materials with enhanced or entirely new functional properties. Materials structured at the nanoscale often exhibit significantly different physical, chemical, optical, and electrical characteristics compared to their bulk counterparts. These unique properties arise largely from their reduced dimensions and increased surface-to-volume ratios, making nanostructured materials particularly attractive for applications in electronics, energy devices, environmental monitoring, and chemical sensing [1, 2]. Although nanotechnology has experienced rapid development over the past several decades, the conceptual understanding of nanoscale materials can be traced back several centuries. Early scientific observations by researchers such as Robert Boyle and Michael Faraday explored the behavior of extremely small particles and their influence on optical properties, particularly in metallic nanoparticles and stained glass [3, 4]. A major conceptual milestone occurred in 1959 when Richard Feynman delivered his influential lecture “There’s Plenty of Room at the Bottom,” in which he envisioned the possibility of manipulating matter at the atomic scale and creating structures only a few atoms wide [5]. Significant nanotechnological progress followed in the late twentieth century with the development of advanced nanofabrication and characterization techniques, including electron beam lithography and high-resolution microscopy, which enabled scientists to directly observe and engineer nanoscale structures [6]. In parallel, advances in microelectronics drove the transition toward nanoelectronics, beginning with the invention of the transistor in 1947 and the integrated circuit in the late 1950s [7]. Between 1970 and 2025, the electronics industry has experienced a rapid technological advancement that has led to a substantial reduction in component dimensions, decreasing from approximately 10 µm to nearly 2 nm as shown in (figure 1.1). This miniaturization was enabled by continual improvements in semiconductor device technology, including the development and integration of increasingly compact components such as diodes and various transistor architectures, including field-effect transistors (FETs), junction field-effect transistors (JFETs), and metal oxide semiconductor field-effect transistors (MOSFETs).

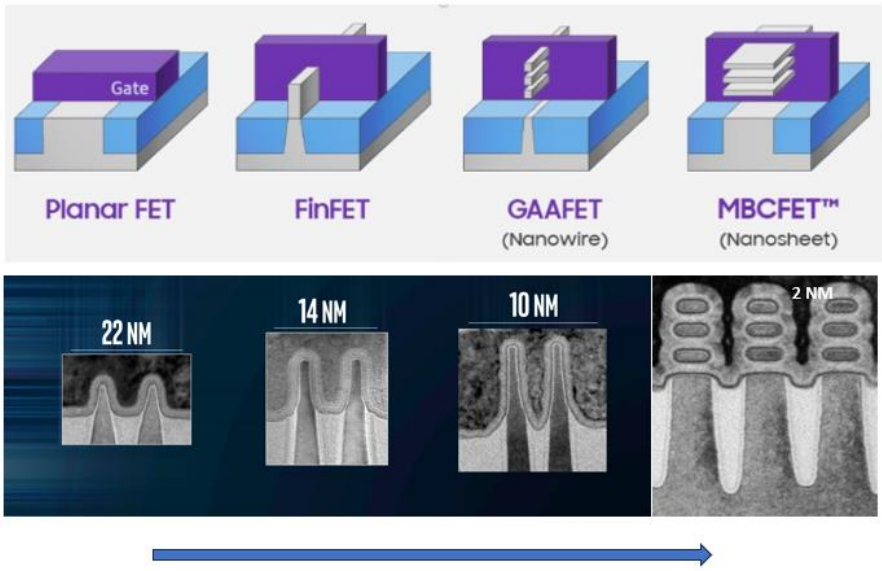

Figure 1.1: Progression of nanoscale transistor structures in modern semiconductor fabrication from 22 nm to 2 nm. Adapted from [8-10]

The evolution of integrated circuit (IC) technology further accelerated this trend by allowing multiple electronic components to be fabricated on a single chip. As fabrication techniques improved, IC technology progressed toward large-scale integration (LSI), enabling millions and eventually billions of transistors to be incorporated into extremely small semiconductor devices. This continuous scaling not only enhanced computational performance and device efficiency but also reduced manufacturing costs, contributing to the widespread adoption of personal computers in both professional and household environments. Recent data on the global nanotechnology market size accounted for USD 8.78 billion in 2025 and is anticipated to grow significantly over the next decade to reach around USD 115.41 billion by 2034 as shown in (figure 1.2), as a result, the development of functional nanomaterials has become an important focus in advancing next-generation technologies.

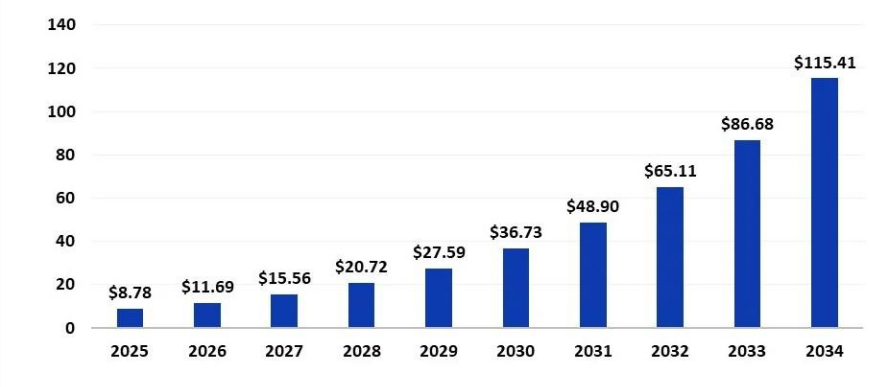

Figure.1.2: Global nanotechnology market size forecast from 2025 to 2034. Adapted from [11].

Despite these advantages, one of the key challenges in the field of nanotechnology is the development of fabrication techniques that are scalable and cost-effective and sustainable. Many conventional nanomaterial fabrication methods rely on complex chemical processes, high temperatures, specialized or sophisticated equipment. Methods such as chemical vapor deposition (CVD), molecular beam epitaxy (MBE), sputter deposition (SD) and pulsed laser deposition (PLD) [12, 13] can produce high-quality nanostructured materials but often require expensive instrumentation and controlled environments, which limits their suitability for large-scale manufacturing [14]. Also, the environmental impact of nanomaterial fabrication from these approaches have become an increasingly important consideration in materials research [15], as conventional fabrication techniques often require toxic materials and solvents, high temperatures, or complex chemical reactions that generate chemical waste. As a result, there is growing interest in green fabrication methods that reduce environmental impact while maintaining high material performance. Solution-based green fabrication emerged as a sustainable and scalable fabrication method that can produce nanomaterials in large quantities while maintaining control over their structural and functional properties. Such approaches are particularly important for applications that require thin film fabrication or integration into practical devices [16, 17]. Among the various fabrication techniques, planetary ball milling (PBM) has emerged as a practical and efficient green approach for producing nanostructured materials on a large scale [18]. This mechanochemical technique relies primarily on mechanical energy rather than chemical reagents to induce reactions and structural transformations by reducing bulk materials into nanoscale particles through repeated energetic impacts between grinding media and powder particles. Ball milling offers several advantages, including simplicity, relatively low cost, and compatibility with large-scale production. In addition, the wet milling as green fabrication process can produce homogeneous nanoparticle suspensions that can be directly used as nanoinks for solution-based thin film fabrication techniques [19]. Also, the need for reliable sensing technologies has increased significantly in recent years and gas sensors play a critical role in environmental monitoring, industrial process control, and safety systems, where rapid and accurate detection of hazardous gases is essential because pollutants such as nitrogen oxides (NOx), carbon monoxide (CO), volatile organic compounds (VOCs), and hydrogen pose significant risks to both environmental and human health [20].

According to recent reports, over 90% of the world's population is exposed to air pollution levels exceeding World Health Organization (WHO) safety limits (5 μg m^{-3}) [21] and accounted for 8.1 million deaths globally in 2021, becoming the second leading risk factor for death, including for children under five years [22], highlighting the need for distributed sensor networks that are low-cost, sustainable, reliable and capable of continuously monitoring gas concentrations in urban and industrial environments to help prevent these unfortunate fatalities. There are generally two main approaches to fabricating nanostructured materials: the "bottom-up" method and the "top-down" method as illustrated in (figure 1.3). The bottom-up approach builds structures by assembling small components such as nanoparticles or molecular clusters into larger, functional arrangements under carefully controlled conditions. Conversely, the top-down approach begins

with a larger unit and systematically reduces it in size until the desired nanostructure is achieved [23]. Interestingly, the top-down strategy relies on a limited set of fabrication techniques, many of which have been adapted from established practices in other industries. However, the majority of nanostructure fabrication methods fall under the bottom-up category. In these processes, the basic building blocks are first fabricated using specific techniques and then organized into composites, coatings, layers, or even consolidated into bulk materials. Ultimately, these two strategies are not mutually exclusive, as many advanced fabrication processes successfully combine both bottom-up and top-down approaches to achieve optimal results [24]. The development of nanostructured materials for sensing applications is particularly promising because their high surface area and tunable morphology can significantly enhance gas adsorption and surface reactions, leading to improved sensitivity and faster response times. Consequently, combining scalable nanomaterial fabrication techniques with thin film sensor technologies provides a promising pathway for the development of low-cost, sustainable and efficient sensing devices.

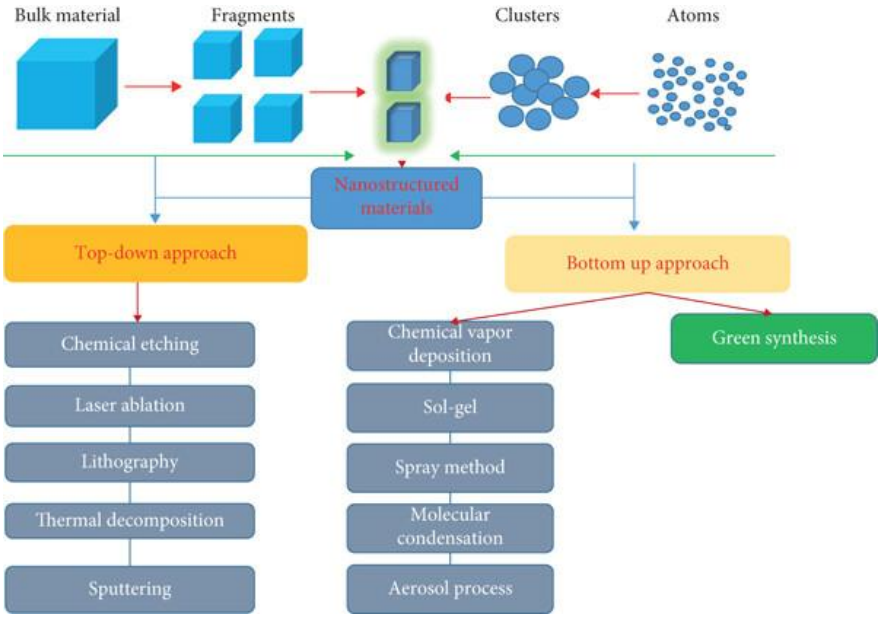

Figure 1.3: Diagram depicting the top-down and bottom-up approaches used in creating nanostructures. Adapted from [25].

1.1.1 Nanomaterials

Nanomaterials are broadly defined as materials that possess at least one structural dimension in the range of approximately 1–100 nanometers (nm) [26]. At this extremely small scale, materials exhibit physical and chemical properties that differ significantly from those of their bulk counterparts. These differences arise primarily from two key nanoscale phenomena: surface effects and quantum confinement. Owing to these unique characteristics, nanomaterials have

become essential components in many emerging technologies, including electronics, sensing devices, catalysis, energy systems, and advanced functional materials [27, 28]. One of the most significant features of nanomaterials is their exceptionally large surface-to-volume ratio. As particle size decreases, the surface-to-volume ratio increases according to an inverse radius dependence (1/r) [29], meaning a much larger fraction of atoms are exposed at the surface rather than remaining within the bulk. In bulk materials, most atoms are located within the interior of the structure and therefore do not actively participate in surface interactions. In contrast, the high proportion of surface atoms in nanomaterials greatly enhances their interaction with the surrounding environment. This characteristic is particularly advantageous in applications that rely on surface reactions, such as catalysis and gas sensing. A larger active surface area provides more adsorption sites for molecules, enabling stronger and more efficient interactions between the sensing material and target analytes [30].

Another phenomenon that strongly influences nanoscale behavior is quantum confinement. When the dimensions of a material approach the nanoscale, the motion of charge carriers such as electrons and holes becomes spatially confined. This confinement alters the electronic band structure, which can lead to changes in electrical conductivity, optical absorption, and emission properties. As a result, nanomaterials can exhibit tunable optical and electronic characteristics that are not present in bulk materials [31]. Nanomaterials can exist in several structural forms depending on their dimensionality. Zero-dimensional (0D) nanostructures include nanoparticles and quantum dots, in which all three spatial dimensions are confined to the nanoscale. One-dimensional (1D) nanostructures, such as nanowires, nanotubes, and nanorods, have one dimension significantly longer than the other two. Two-dimensional (2D) nanostructures, including thin films and nanosheets, possess nanoscale thickness while extending laterally over much larger dimensions. Three-dimensional (3D) is just the bulk crystal, extending into all three spatial domains as illustrated in (figure 1.4) below. Each of these structural forms exhibits distinct properties that can be tailored for specific technological applications [32].

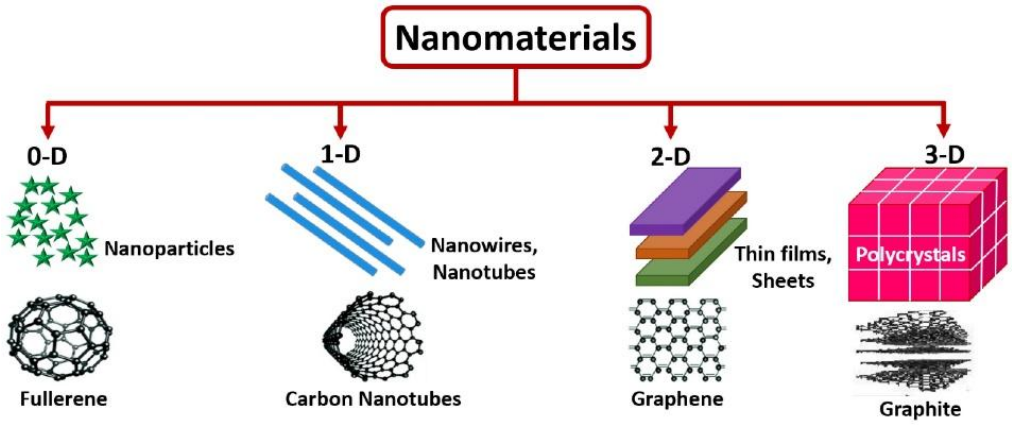

Figure 1.4: Illustration of nanostructure dimensionality, highlighting 0D nanoparticles, 1D nanowires, 2D nanosheets, and 3D nanostructured materials. Adapted from [33].

1.1.2 Nanomaterials Properties and Applications

Among the various properties influenced by nanoscale dimensions, electrical properties are one of the most extensively studied [34]. At the nanoscale, charge transport mechanisms deviate from classical behavior due to phenomena such as electron confinement, tunneling, and increased scattering at surfaces and grain boundaries [35]. These effects can lead to either enhancement or suppression of electrical conductivity depending on the material system and structural characteristics. Defects, impurities, and crystallographic imperfections play a critical role in determining the electrical performance of nanomaterials. In the case of zinc oxide (ZnO), intrinsic defects such as oxygen vacancies and zinc interstitials act as donors, contributing free electrons that result in n-type conductivity [36]. The presence and distribution of these defects can be manipulated through fabrication methods and processing conditions, allowing for the tuning of electrical properties to suit specific applications, including gas sensing and electronic devices.

Optical behavior of nanomaterials is similarly influenced by size reduction and surface effects. In semiconductor nanomaterials, the confinement of charge carriers within dimensions comparable to their de Broglie wavelength gives rise to quantum confinement effects. This results in the discretization of energy levels and an increase in the effective band gap as particle size decreases. Consequently, nanomaterials can exhibit size-dependent optical absorption and emission characteristics. For instance, smaller nanoparticles tend to emit light at shorter wavelengths (higher energy), while larger particles emit at longer wavelengths (lower energy) as shown in (figure 1.5) [37]. This tunability of optical properties is particularly useful in applications such as light-emitting devices, photodetectors, and biomedical imaging. In metallic nanostructures, collective oscillations of conduction electrons, known as surface plasmon resonance, are also highly sensitive to particle size, shape, and surrounding dielectric environment, leading to distinct optical signatures that can be exploited in sensing and photonic applications.

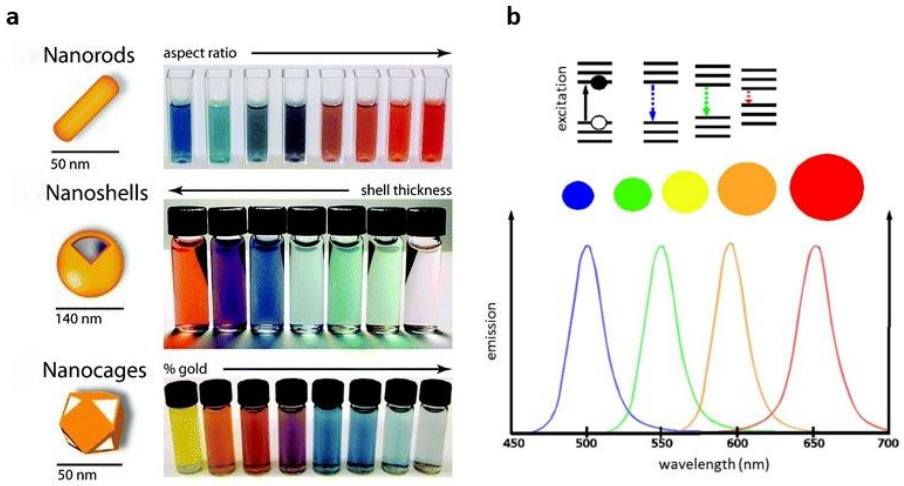

Figure 1.5: (a) Fluorescence emission of different gold nanoparticle sizes commonly applied in biomedical applications [37]. Emission spectra of various sizes quantum dots (semiconductor nanoparticles). Adapted from [38].

From a chemical standpoint, the high surface area of nanomaterials significantly enhances their reactivity and catalytic activity. A larger number of active sites are available for interaction with reactant molecules, which can lead to improved efficiency in catalytic processes [39]. Surface atoms, having unsaturated coordination, are more chemically active and can facilitate reactions that are less favorable in bulk materials. For example, gold, which is typically considered chemically inert in its bulk form, exhibits remarkable catalytic activity when prepared as nanoparticles as shown in (figure 1.6) [40]. This enhanced reactivity is influenced by factors such as particle size, surface morphology, and the presence of defects or dopants.

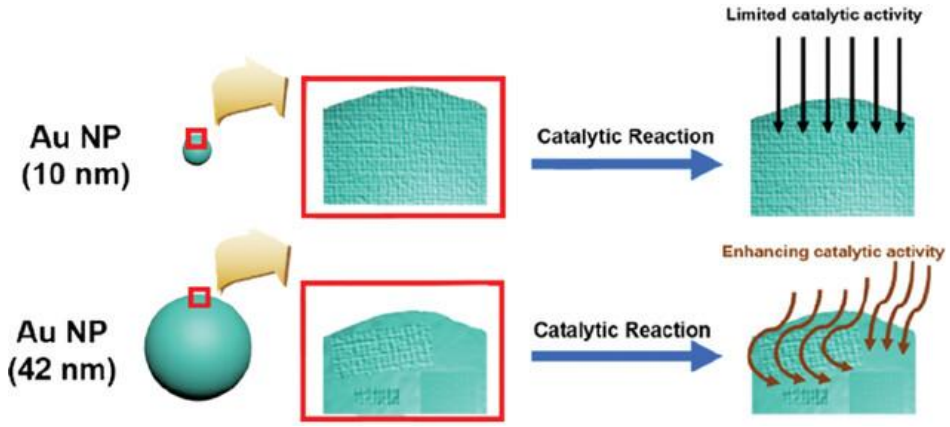

Figure 1.6: Size-dependent catalytic activity of gold nanoparticles: enhanced performance in larger AuNPs (42 nm) Compared to Smaller Ones (10 nm). Adapted from [40]

Beyond catalytic activity, surface properties of nanomaterials also influence the interaction of nanomaterials with biological systems. The adsorption of ions and biomolecules onto nanoparticle surfaces can alter cellular responses, making surface chemistry a key determinant of toxicity and biocompatibility [41]. In particular, surface charge significantly affects colloidal behavior, governing aggregation or agglomeration processes that modify the effective size and shape of nanoparticles in biological environments. These changes, in turn, influence how nanoparticles interact with cells and tissues. For example, studies on mesoporous silicon nanoparticles have demonstrated that surface functionalization and charge strongly affect immune and cellular responses [42]. Negatively charged hydrophilic or hydrophobic nanoparticles have been found to induce lower levels of Adenosine triphosphate (ATP) depletion and genotoxicity compared to positively charged, amine-functionalized counterparts.

Structurally, nanomaterials exhibit behaviors that differ markedly from bulk materials due to the influence of reduced dimensions and increased surface energy. Parameters such as particle size,

morphology, and crystallinity become critical in defining material properties [43]. As particle size decreases, quantum size effects become more pronounced, leading to changes in electronic structure and stability. Additionally, nanomaterials may display reduced melting points compared to their bulk counterparts, a phenomenon attributed to the higher proportion of surface atoms with lower coordination numbers. This reduction in melting temperature can influence processing conditions and thermal stability. Furthermore, the nanoscale can enable the formation of metastable or entirely new phases that are not observed in bulk materials, expanding the range of achievable material properties and functionalities. (Figure 1.7) illustrates the formation of branch-like and cluster-like ZnO nanorods at varying concentrations [44]. It highlights that adjusting growth conditions enables precise control over nanostructure morphology. These variations in size and shape significantly affect the optical properties of ZnO, making them highly relevant for applications in solar cells and electrochemical systems.

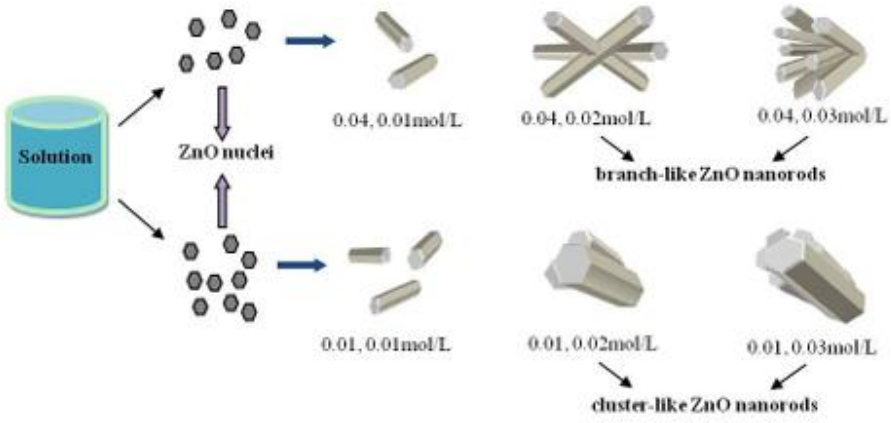

Figure 1.7: Schematic representation of the growth mechanism leading to the formation of branch-like and cluster-like ZnO nanorods at varying concentrations. Adapted from [44]

Magnetic properties undergo profound transformations at the nanoscale, primarily due to altered magnetic coupling between neighboring atoms, surface effects, and finite-size phenomena. As a result, materials that are non-magnetic in their bulk form can exhibit magnetic behavior when reduced to nanoscale dimensions. This shift is closely tied to changes in atomic arrangement and the increasing influence of surface atoms, which collectively modify the overall magnetic response [45]. For example, magnetic nanoparticles used in biomedical applications are typically composed of single-domain crystals, with core sizes ranging from approximately 5 to 30 nm. At this scale, the formation of multiple magnetic domains common in bulk ferromagnetic materials becomes energetically unfavorable. Instead, each nanoparticle behaves as a single magnetic entity, often described as a giant magnetic moment [46]. This intrinsic single-domain nature represents a fundamental departure from bulk materials and plays a crucial role in enabling advanced theranostic functionalities. One of the most distinctive magnetic phenomena emerging at this scale is superparamagnetism [47]. This behavior occurs when the thermal energy becomes

comparable to the magnetic anisotropy energy barrier, allowing the magnetic moment of a nanoparticle to spontaneously flip direction as shown in (figure 1.8). Consequently, the magnetization of the particle can randomly reorient in the absence of an external magnetic field. The onset of superparamagnetism is highly dependent on both particle size and temperature, highlighting the importance of nanoscale control in tuning magnetic behavior. In the superparamagnetic state, nanoparticles exhibit uniform magnetization and high magnetic susceptibility under an applied magnetic field, enabling strong and rapid magnetic responses. However, unlike bulk ferromagnets, they show no remanent magnetization or coercivity once the external field is removed, causing their net magnetization to quickly decay to zero [48]. This reversible magnetic behavior is particularly advantageous for applications such as magnetic resonance imaging (MRI), targeted drug delivery, and high-density data storage, where controlled and non-permanent magnetization is essential.

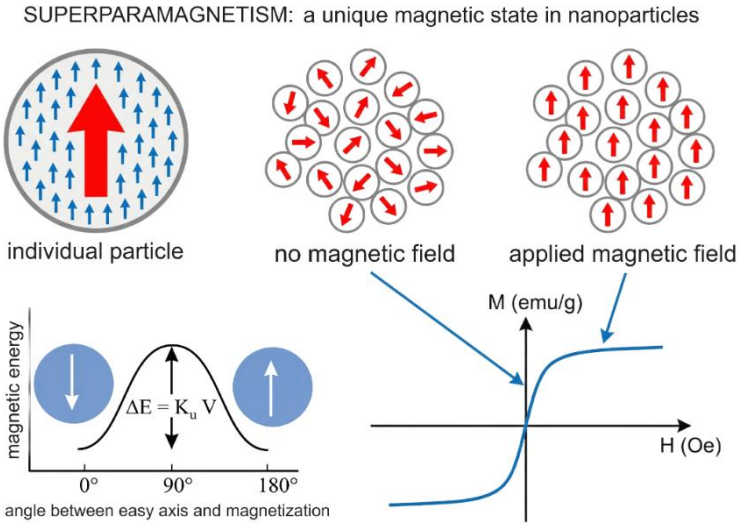

Figure 1.8: Superparamagnetic behavior and magnetic response of single-domain nanoparticles. Adapted from [49]

These unique characteristics of nanomaterials have enabled their integration into a wide range of technological fields and are particularly important in applications involving optoelectronic devices, photodetectors and diodes, and nanoscale electronic components. In electronics, nanoscale materials are used to fabricate smaller, faster, and more energy-efficient devices. Among these diverse applications, one of the most rapidly developing areas is the use of nanomaterials in chemical and gas sensing technologies [50]. In sensing applications, the structure and morphology of the sensing material play a critical role in determining overall sensor performance. Because sensing processes typically occur at the material surface, nanostructured materials offer a significant advantage due to their high surface area and enhanced surface reactivity. When gas molecules interact with the surface of a nanostructured semiconductor, they can alter the concentration of charge carriers within the material, producing measurable changes in electrical conductivity. These conductivity variations form the fundamental operating principle

of many semiconductor-based gas sensors. The particle size, morphology, and surface structure of nanomaterials strongly influence key sensor characteristics such as sensitivity, response time, and selectivity. Smaller particle sizes increase the number of active adsorption sites, while porous or rough surfaces facilitate improved gas diffusion and interaction with the sensing layer. Furthermore, nanoscale materials can promote faster charge carrier transport and enhanced surface reactions, which contribute to improved sensing performance. Consequently, controlling the structure, size, and morphology of nanomaterials during fabrication and processing is essential for optimizing their functional properties. The ability to engineer nanomaterials with tailored characteristics has made them central to the development of advanced sensing devices and other high-performance technologies.

Beyond sensing, nanomaterials exhibit remarkable optical, electrical, magnetic, and catalytic properties that enable their widespread use across industrial and scientific domains. Their applications extend into energy systems, catalysis, flexible electronics, environmental remediation, and biomedical technologies [51]. In energy-related applications, nanostructured materials significantly enhance the efficiency of devices such as fuel and solar cells, batteries, and supercapacitors [52]. Fuel cells, for instance, convert chemical energy directly into electrical energy through electrochemical reactions, often using catalysts like platinum, although alternative nano catalysts including transition metal oxides, iron-based materials, and carbon-based systems are being explored to reduce cost while maintaining performance. Similarly, nanomaterials improve energy storage by enabling higher power and energy densities, particularly in supercapacitors where charge separation occurs at electrode–electrolyte interfaces. In the biomedical field, magnetic and functional nanoparticles are utilized for imaging, drug delivery, biosensors and diagnostic applications, benefiting from their controllable size and surface properties [53-55].

In the field of flexible electronics, nanomaterials address the limitations of conventional rigid materials such as silicon. While silicon remains fundamental to modern electronics, its mechanical rigidity restricts its use in bendable devices. Nanomaterials such as carbon nanotubes, graphene, conductive polymers, and metallic nanowires offer superior flexibility, conductivity, and mechanical resilience [56]. These materials enable the development of next-generation devices, including foldable displays, wearable sensors, electronic paper, and transparent electronic systems. Their lightweight and low-cost characteristics further enhance their suitability for large-area and consumer applications.

Nanomaterials also play a transformative role in catalysis. Due to their extremely high surface area, nanocatalysts provide abundant active sites for chemical reactions, lowering activation energy and increasing reaction rates [57]. This makes them highly effective in applications such as water purification, biodiesel production, photocatalysis, and wastewater treatment. For example, nanostructured metal oxides like ZnO can facilitate the degradation of organic pollutants under light irradiation, demonstrating their potential in sustainable environmental technologies [58].

Environmental pollution mitigation represents another critical area where nanomaterials demonstrate significant impact. Nanostructured photocatalysts such as ZnO, SiO_2 and TiO_2 are widely used to remove pollutants from air and water through catalytic degradation processes [59]. Their high reactivity allows them to interact efficiently with toxic substances, enabling applications in wastewater treatment, air purification, and self-cleaning materials. Additionally, graphene-based nanomaterials have shown strong potential for removing both organic and inorganic contaminants due to their exceptional adsorption properties.

These various applications and relevance of nanomaterials is particularly evident in semiconductor technology, where continuous device miniaturization has played a central role in improving performance. This trend follows Moore's Law, which predicts the periodic doubling of the number of components on integrated circuits [60]. As device dimensions approach the nanoscale, semiconductor systems achieve higher computational capacity, improved efficiency, and enhanced performance, as illustrated in (figure 1.9)

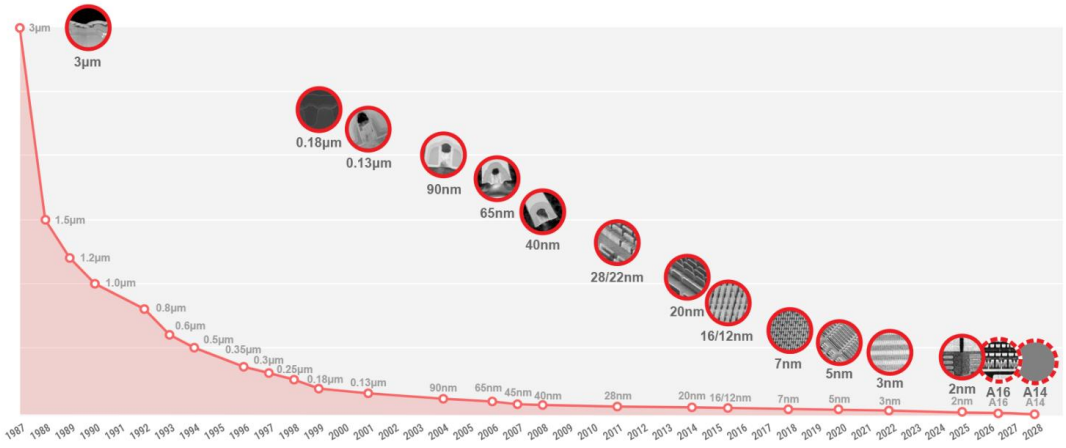

Figure 1.9: CPU technology node progression: from micron-scale to nanometer transistors. Adapted from [61].

Overall, nanomaterials are driving innovation in advanced technologies while also creating opportunities for improvements in conventional industries. With continued advances in fabrication techniques and expanding application areas, the large-scale production of nanomaterials is expected to play an increasingly important role in shaping the future of the chemical industry and many other technological sectors.

1.1.3 Thin Film Sensors and Nanostructures

Thin film sensors have become an important class of sensing devices due to their versatility, sensitivity, and compatibility with modern microfabrication technologies. These sensors typically consist of a thin layer of functional material deposited onto a substrate, where the interaction between the sensing material and the surrounding environment produces measurable changes in electrical, optical, or chemical properties [62]. Additive manufacturing techniques have emerged as promising approaches for the fabrication of functional thin film sensors. Unlike conventional microfabrication methods, additive processes deposit materials only where needed, minimizing material waste and reducing manufacturing complexity [63]. Techniques such as inkjet printing, aerosol jet printing, and blade coating enable the deposition of functional inks onto flexible substrates for the fabrication of electronic devices [64]. Among the various types of thin film sensors, semiconductor metal oxide (SMO) sensors have attracted significant attention because of their ability to detect a wide range of gases and their relatively simple device structures. SMO-based thin film sensors are widely used in applications such as environmental monitoring, industrial safety systems, gas leak detection, and photodetection. Semiconductor metal oxides such as zinc oxide (ZnO), tin oxide (SnO_2), titanium dioxide (TiO_2), and tungsten oxide (WO_3) are commonly used sensing materials because of their semiconducting properties and strong interaction with gas molecules [65, 66]. When these materials are exposed to gases in the surrounding environment, surface reactions occur that alter the electrical conductivity of the sensing layer. In (figure 1.10), at ambient conditions, oxygen is adsorbed by the surface of the SMO thin film from the atmosphere and the adsorbed oxygen acquires electrons from the conduction band and forms oxygen ions (O_2^-) and when target gas such as ammonia gas (NH_3) is introduced onto the SMO film, the surface oxygen ions react with the ammonia gas to release free electrons (e^-) which reduce the resistance of the film and increases conductivity as represented by the following reactions (equation 1 and 2);

$$O_2 + e^- \rightarrow O_2^-(\text{ads}) \quad (1)$$

$$2NH_3 + 3O^- \rightarrow N_2 + 3H_2O + 3e^- \quad (2)$$

This change in conductivity can be measured as a variation in current or resistance, allowing the presence and concentration of target gases to be detected [67]. This is one widely accepted model, as actual behavior may depend on temperature, surface states, and material structure. The ability of SMO sensors to convert chemical interactions into measurable electrical signals makes them highly suitable for monitoring toxic, combustible, and environmentally harmful gases.

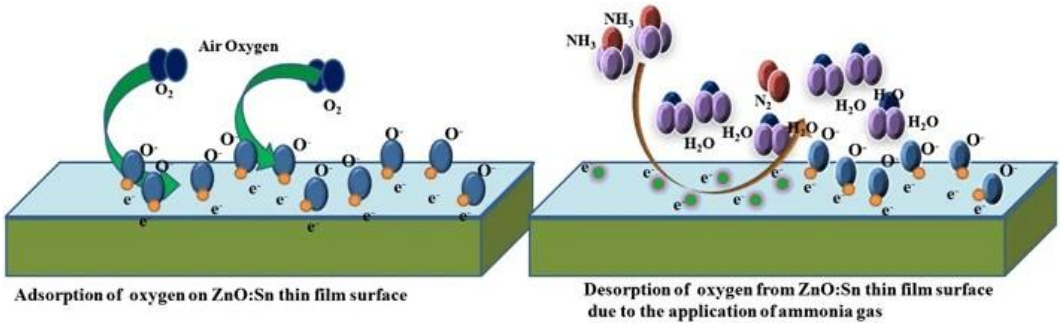

Figure 1.10: Schematic illustration of the oxygen adsorption process and ammonia gas sensing mechanism. Adapted from [67]

Thin film SMO sensors play a particularly important role in environmental monitoring, where accurate detection of pollutants such as carbon monoxide, nitrogen oxides, hydrogen, and volatile organic compounds is necessary to ensure air quality and protect public health. In industrial environments, gas sensors are used to detect hazardous or combustible gases in order to prevent accidents and ensure safe operation of equipment and facilities [68]. Similarly, in chemical processing plants and laboratories, continuous gas monitoring systems help maintain safe working conditions by providing early detection of leaks or dangerous concentrations of gases [69]. These applications require sensors that are not only sensitive but also reliable, stable, and capable of operating under varying environmental conditions.

Recent studies have demonstrated that nanostructured metal oxide sensors exhibit good gas sensing performance due to their high surface area and enhanced surface reactions. For example, ZnO nanoink-based thin film sensors fabricated via planetary ball milling have been reported to detect hydrogen, argon and methane at low concentrations demonstrating selective sensing capabilities of SMO [70]. Similarly, Kanth et al., also developed a nanostructured Pd–PdO thin film NO_2 sensor capable of detecting nitrogen dioxide at sub-ppm concentrations with a detection limit of approximately 80 ppb at room temperature. The films exhibited sensing responses of approximately 60 % for 500 ppb NO_2 and nearly 100 % for 10 ppm NO_2, demonstrating the sensitivity performance of Pd–PdO nanostructured films for low-concentration toxic gas detection [71]. In addition, Sung et al. developed metal-oxide-decorated mesoporous silica chemiresistors capable of detecting hydrogen sulfide in the 1–100 ppm range, with response values increasing from approximately 1.75–5.66 at 10 ppm to 5.56–12.13 at 100 ppm, demonstrating the effectiveness of porous structures for enhanced gas sensing performance [72].

In addition to gas detection, thin film semiconductor sensors are also widely used in photodetection applications. Photodetectors are devices that convert light signals into electrical signals and are essential in technologies such as optical communication systems, imaging devices, environmental sensing, and ultraviolet detection [73]. Semiconductor metal oxides such as ZnO are particularly attractive for photodetection because of their wide band gap, high transparency in the visible region, and strong response to ultraviolet light [74, 75]. When light with sufficient energy is absorbed by the semiconductor material, electron–hole pairs are generated on the

surface of the film, leading to changes in electrical conductivity that can be detected and measured. As illustrated in (figure 1.11), in dark conditions, oxygen molecules adsorb on the SMO surface and capture electrons from the conduction band, forming negatively charged oxygen ions (O_2^-) and creating a depletion region. When the SMO thin film is exposed to light of appropriate energy ($h\nu$ (light) > Eg (SMO)), electron–hole pairs are generated. These photogenerated carriers migrate to the surface and neutralize the adsorbed oxygen ions through photo desorption, reducing the depletion layer and increasing electrical conductivity. As light's illumination continues, electrons accumulate and the photocurrent rises until it reaches a saturation state.

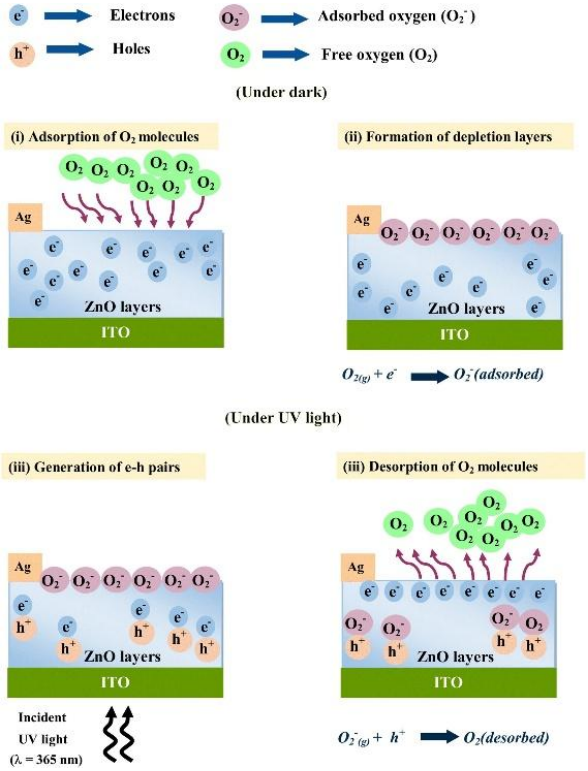

Figure 1.11: Conceptual schematic depicting surface adsorption of oxygen molecules in dark conditions and their desorption under light of appropriate wavelength (UV light). Adapted from [76]

This photoresponse forms the basis of thin film photodetectors and photo diodes. The performance of thin film photodetection sensors is typically evaluated using sensing parameters, including sensitivity, selectivity to different wavelengths in the light spectrum and detection at different light source power [77, 78]. The use of nanostructured materials in thin film sensors has significantly improved sensor performance. Nanostructured materials possess a much larger surface-to-volume ratio compared to bulk materials, providing more active sites for light interaction and surface reactions. As a result, photons from light source can interact more effectively with the sensing surface, leading to stronger electrical responses and improved sensitivity. Furthermore, the morphology, particle size, and surface characteristics of nanostructured thin films play a crucial role in determining their sensing behavior.

Gimenez et al [75]. developed a simple ZnO-coated paper photoconductive UV sensor that exhibited a photoresponse under ultraviolet illumination. The device showed dark currents on the order of ~10^{-8} A, which increased by approximately 60 times when exposed to UV light at a distance of 10 cm and up to ~280 times at 5 cm, while ZnO films deposited on paper generated photocurrents roughly ten times larger than those on glass substrates. The sensor also demonstrated spectral sensitivity beginning near ~410 nm, with peaks around 380 nm and 340 nm. Also, Rahman et al. developed a p-NiO/n-ZnO heterojunction infrared photodetector fabricated by spray pyrolysis on glass substrates, demonstrating effective IR photodetection due to interfacial defect states at the oxide junction. The device exhibited a low dark current of approximately 0.02 μA, while IR illumination at 1.1–2.6 mW cm^{-2} produced a significant increase in photocurrent with increasing bias. At an applied bias of ±30 V, the device achieved responsivities of approximately 9.3 mA W^{-1} in forward bias and 17 mA W^{-1} in reverse bias [79]. Overall, thin film semiconductor metal oxide sensors represent a promising platform for developing sensitive, reliable, and cost-effective sensing devices. By combining the advantages of nanostructured materials with scalable and sustainable thin film fabrication techniques, it is possible to design sensors with enhanced performance suitable for a wide range of environmental, industrial gas sensing and photodetection applications.

1.2. Overview of Thesis and Contributions

This thesis presents the fabrication, characterization, and application of mechanochemically fabricated ZnO nanoinks for low-cost, environmentally friendly thin-film gas sensor devices. The work focuses on understanding how planetary ball milling (PBM) parameters influence nanostructure formation and how these structural variations translate into functional sensing performance. The overall organization of the thesis is structured into five chapters:

Following this introductory chapter, which provides background on nanomaterials, thin-film sensors, and the motivation for solution-based fabrication approaches, Chapter 2 presents a detailed description of the fabrication process of ZnO nanostructures using planetary ball milling. This chapter outlines the mechanochemical fabrication principles, the influence of key milling parameters such as speed, time, and solvent choice, and the preparation of ZnO nanoinks. Additionally, it includes the thin-film deposition process using an adjustable blade applicator and discusses the various material characterization techniques employed, including SEM, TEM, AFM, Raman spectroscopy, UV-Vis spectroscopy, and EDX analysis. Chapter 3 focuses on the fabrication of ZnO thin-film gas sensor devices and their multifunctional applications. It introduces the device architecture, including electrode configurations such as pencil-drawn interdigitated electrodes and conductive paints. The chapter also describes the experimental gas sensing setup and key performance metrics, including sensitivity, selectivity, response time, recovery time, and limit of detection. The relationship between nanostructure properties and sensor performance is discussed in detail. Chapter 4 presents the experimental results and discussion. It provides

analysis of film morphology, particle size distribution, and structural properties based on various characterization techniques. Furthermore, this chapter investigates the gas sensing behavior of the fabricated devices under different conditions, including varying gas concentrations, environmental factors, light, temperature and substrate types. The underlying gas sensing mechanisms, including adsorption–desorption processes and the role of defect states, are also discussed. Finally, Chapter 5 summarizes the key findings of the thesis and highlights the contributions of this work. It also outlines potential future research directions, including photodetection applications, material optimization through doping and composites, and improvements in device fabrication and sensing systems.

Contributions

Conferences

1. G. Boakye, A. Venkataraman, C. Papadopoulos, “Low-cost sensors printed using mechanochemically synthesized nanoinks”, in *Institute of Electrical and Electronics Engineers Nanotechnology Materials and Devices Conference (IEEE-NMDC)*, 2025 [80]
2. Anusha Venkataraman, Gibson Boakye, Chris Papadopoulos, “Eco-friendly fabrication of nanoparticle thin films on paper via mechanochemical processing for low-cost printed sensors”, in *American Chemical Society (ACS),* Fall Meeting, 2026. (submitted)
3. G. Boakye, A. Venkataraman, C. Papadopoulos, “Thin film gas sensors on paper substrates via mechanochemical solution-based processing”, in *Electrochemical Society (ECS),* Summer meeting, 2026. Accepted (abstract withdrawn).
4. Gibson Boakye, Sahil Dawka, Raju Sapkota, Anusha Venkataraman, Chris Papadopoulos, “Printed optoelectronic devices and sensors based on mechanochemically synthesized nanoparticle inks”, in NANO 2026, Fall Meeting. (submitted)

Journal articles

1. G. Boakye, A. Venkataraman, C. Papadopoulos, “Eco-friendly, low-cost and flexible gas sensors via a scalable pathway using printed electronics and PBM-mechanochemically fabricated ZnO nanoinks”, *Journal of Physics: Materials*, 2026. (to be submitted)

Other work

1. Boakye, G. A, et al, “Nanoscale plastic pollution: sources, identification and potential mitigation”, *2025 Nanotechnology 36 422001* [81]

Chapter 2

2. Fabrication of ZnO Nanostructures and Experimental Methods

2.1. Introduction

Zinc oxide (ZnO) is a versatile material known for its semiconducting, piezoelectric, and pyroelectric properties. As an II–VI compound semiconductor, it has attracted considerable interest because of its notable electrical, optical, structural, and chemical characteristics. ZnO commonly exhibits n-type conductivity, primarily due to intrinsic defects such as oxygen vacancies [82]. One of its most defining characteristics is its wide direct bandgap of approximately 3.37 eV at room temperature (300 K), which places its optical absorption edge in the ultraviolet (UV) region. In addition to this wide bandgap, ZnO exhibits a relatively large exciton binding energy of about 60 meV, which is substantially higher than that of many conventional semiconductors such as GaN (25 meV) and ZnSe (22 meV) [83]. This high exciton binding energy enables stable excitonic emission at and above room temperature, making ZnO highly suitable for optoelectronic applications including UV photodetectors, light-emitting diodes, and laser devices. From a structural perspective, ZnO most commonly crystallizes in the hexagonal wurtzite structure (space group $P6_3mc$), which is thermodynamically stable under ambient conditions. The wurtzite unit cell is defined by two lattice parameters, a and c, with an ideal ratio of $c/a \approx 1.633$ ($\sqrt{8/3}$). Typical experimental values are approximately $a \approx 3.25$ Å and $c \approx 5.2$ Å [84]. The structure consists of alternating planes of tetrahedrally coordinated Zn^{2+} and O^{2-} ions stacked along the c-axis. This arrangement results in a non-centrosymmetric and polar crystal structure, giving rise to spontaneous polarization along the [0001] direction. The lack of inversion symmetry leads to strong piezoelectric and pyroelectric properties, making ZnO particularly attractive for electromechanical devices, sensors, and energy harvesting applications. In addition to the wurtzite phase, ZnO can also exist in zinc blende (cubic) and rocksalt (cubic) crystal structures as illustrated in (figure 2.1) [85]. The zinc blende phase is metastable and can be stabilized under specific growth conditions, such as epitaxial deposition on cubic substrates. In contrast, the rocksalt phase is typically formed only under high-pressure conditions (on the order of several gigapascals). However, for most practical applications, particularly in nanostructures and thin films, the wurtzite phase dominates due to its inherent stability.

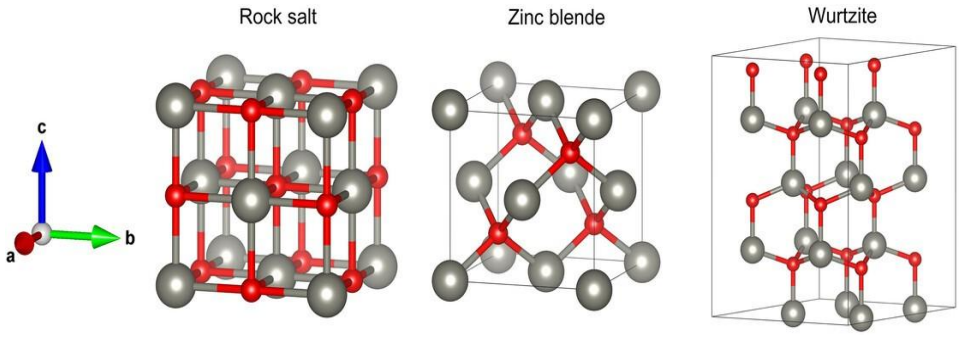

Figure 2.1: ZnO crystallizes in three distinct structures: rock salt, zinc blende, and wurtzite. Adapted from [85].

ZnO is also notable for its rich defect chemistry, which plays a crucial role in determining its electrical and sensing properties. Intrinsic defects such as oxygen vacancies (V_o), zinc interstitials (Zn_i), and oxygen interstitials (O_i) can significantly influence carrier concentration and conductivity. Typically, ZnO exhibits n-type conductivity, often attributed to these native defects or unintentional hydrogen incorporation [86]. These defect states introduce energy levels within the bandgap, which can act as donors and enhance electrical conductivity. At the same time, they contribute to luminescence phenomena, including visible emissions associated with defect-related transitions. The electronic band structure of ZnO has been extensively studied using theoretical methods such as local density approximation (LDA) combined with self-interaction corrected pseudopotentials (SIC-PP) [87]. These calculations confirm that both the valence band maximum (VBM) and the conduction band minimum (CBM) occur at the Γ point (k = 0), verifying the direct bandgap nature of ZnO. The valence band is primarily composed of oxygen 2p orbitals, while the conduction band is dominated by zinc 4s (often approximated as 3s in simplified models) states, with deeper energy levels associated with Zn 3d electrons. Theoretical calculations typically predict a bandgap of approximately 3.7–3.8 eV, which is in reasonable agreement with experimentally measured values of ~3.3–3.4 eV, considering known limitations of LDA-based methods as shown in (figure 2.2b).

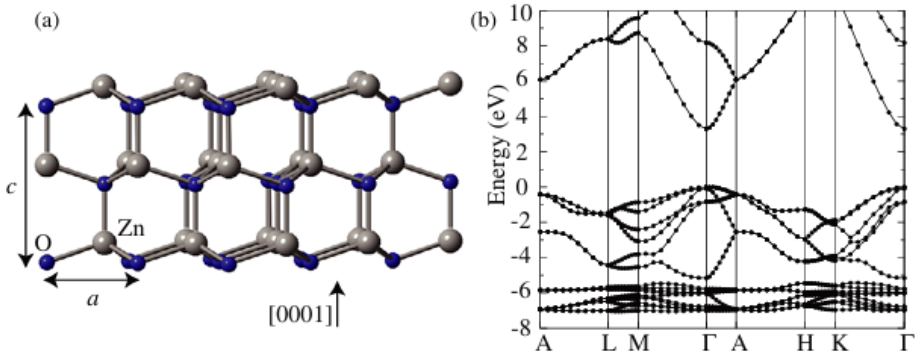

Figure 2.2: (a) shows the wurtzite crystal structure of ZnO with the lattice parameters a and c, and (b) shows the band structure of ZnO calculated with the HSE hybrid functional. Adapted from [88]

Another important advantage of ZnO lies in its ability to form a diverse range of nanostructures, including nanoparticles (1–100 nm), nanorods, nanowires, nanorings, nanoflowers, and tetrapods as shown in (figure 2.3). These nanostructures exhibit significantly enhanced surface-to-volume ratios, which are critical for applications such as gas sensing, where surface interactions dominate device performance. The high surface area facilitates adsorption of gas molecules and enhances sensitivity. Additionally, the polar surfaces of ZnO, particularly the (0001) and (000-1) planes, contribute to anisotropic growth and unique surface reactivity [89].

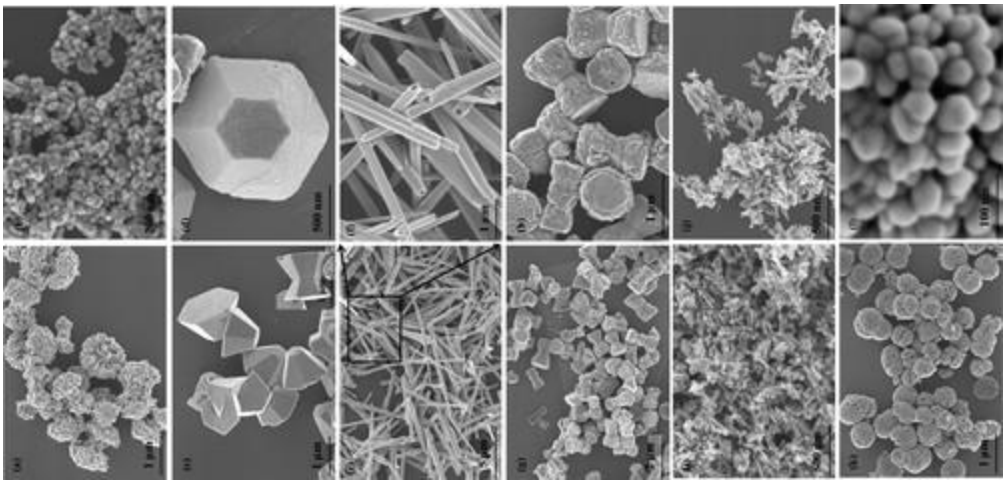

Figure 2.3: FE-SEM images of as-synthesized samples of ZnO forming diverse range of nanostructures. Adapted from [90].

ZnO is also highly attractive from a practical and economic standpoint as it is the second most common metal oxide in the Earth's crust, naturally occurs as the mineral zincite and typically appears as a white powder with very low solubility in water [91]. It is composed of abundant, non-toxic, and inexpensive elements (zinc and oxygen), making it one of the most cost-effective semiconductor materials available. Its chemical stability, resistance to harsh environments, and compatibility with low-temperature processing further enhance its suitability for large-fabrications and has been widely used as an additive in a plethora of materials and products including ceramics, glass, cement, rubber, lubricants, paints, ointments, adhesives, plastics, sealants, pigments, foods, batteries, ferrites and fire retardants as illustrated in (figure 2.4) [92]. These combined properties make ZnO an ideal candidate for gas sensing applications, particularly in resistive-type sensors. The sensing mechanism is largely governed by the adsorption of oxygen molecules on the ZnO surface, which capture free electrons and form ionic species such as O_2^-, O^-, and O^{2-}, depending on temperature. This process creates a surface depletion layer and increases the material's resistance. Upon exposure to reducing gases (e.g., hydrogen), these adsorbed oxygen species react with the gas molecules, releasing trapped electrons back into the

conduction band and decreasing resistance [93]. The magnitude of this change depends strongly on factors such as particle size, surface defects, and morphology. In this context, controlling the nanostructure and defect density of ZnO is critical for optimizing sensor performance. Mechanochemical fabrication methods, such as planetary ball milling, offer a scalable and low-cost approach to tailoring these properties. By varying milling parameters, it is possible to influence particle size (typically ranging from tens to hundreds of nanometers), surface roughness, and defect concentration, thereby tuning the electrical and sensing behavior of ZnO.

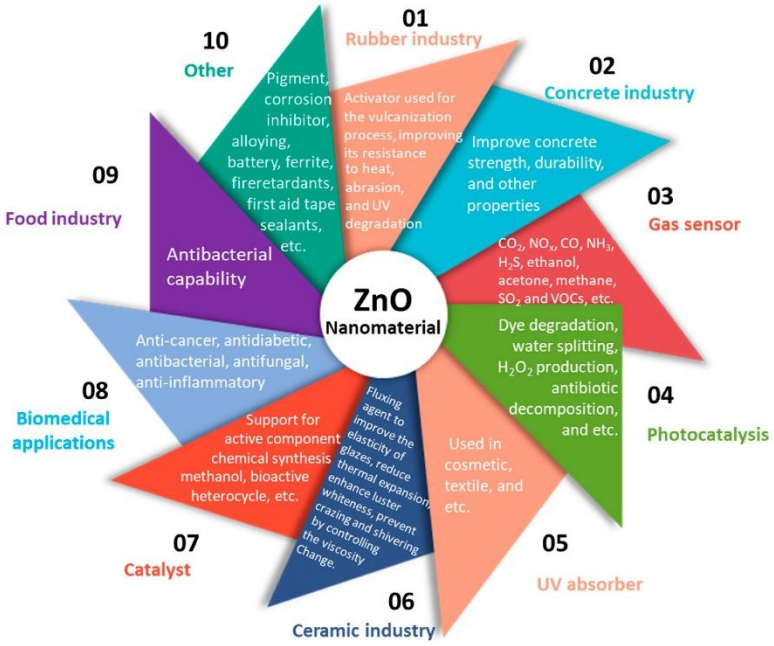

Figure 2.4: Various uses for ZnO nanomaterials and a succinct explanation of each use. Adapted from [92].

This chapter focuses on the fabrication of ZnO nanostructures using planetary ball milling and their subsequent transformation into functional thin films. A detailed investigation of the relationships between processing parameters, material properties, and potential device performance is presented through characterization techniques. These insights form the foundation for the development of efficient, low-cost ZnO-based gas sensors discussed in later chapters.

2.2 Experimental Set-Up and Materials

2.2.1 Planetary Ball Milling Fabrication Method

Planetary ball milling (PBM) is widely recognized as a top-down approach capable of reducing coarse particles into fine and ultra-fine nanometer-scale powders through repeated mechanical impacts [94]. Its ability to operate under both dry and wet conditions, combined with its relatively

short processing time, low processing temperatures, high reproducibility, and safe handling, makes it one of the most preferred laboratory-scale nanofabrication methods. Furthermore, PBM due to its low input energy, has been extensively adopted in industrial sectors such as chemical processing, pharmaceuticals, and food production, where precise control over particle size is essential for optimizing material performance [95]. At its core, planetary ball milling operates through the application of energetic collisions between grinding media (balls) and powder particles. These collisions induce repeated fracturing, cold welding, and re-agglomeration processes, ultimately leading to particle size reduction. Importantly, the energy transferred during these collisions is sufficiently high to not only break particles but also to alter their internal chemical structure through bond breaking and reformation. As a result, PBM is categorized as a mechanochemical fabrication technique, capable of producing a wide range of advanced materials including nanocrystalline powders, nanocomposites, amorphous phases, and mechanically alloyed systems. The planetary ball mill consists of a rotating disk on which typically two to four grinding jars are mounted. Each jar rotates about its own axis while simultaneously revolving around a central axis in the opposite direction as illustrated in (figure 2.5b) [96]. This dual rotational motion generates significant centrifugal forces, resulting in high impact energies of the milling balls. These forces enable efficient grinding and energy transfer to the powder particles trapped between colliding balls. The inelastic nature of these collisions ensures that kinetic energy is effectively dissipated into the powder, enhancing the grinding efficiency.

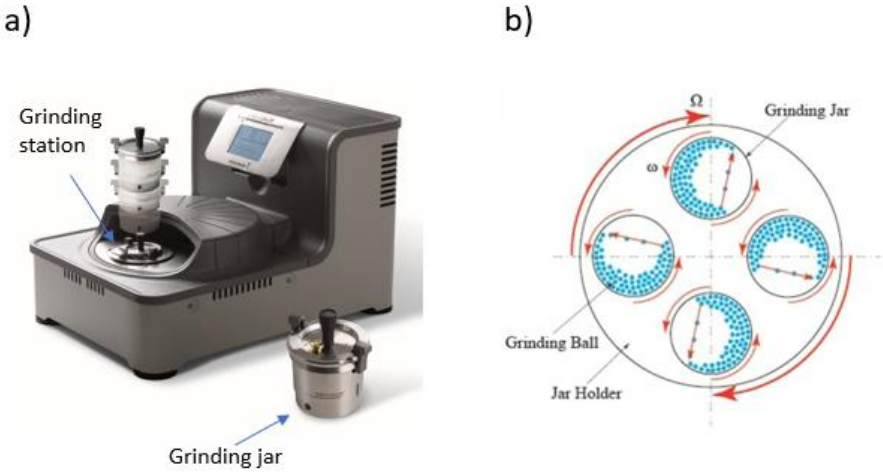

Figure 2.5: (a) Fritsch Pulverisette 7 (PBM) premium line with two grinding chambers [97]. (b) Schematic of a planetary ball mill with four grinding chambers rotating in opposite direction to sun disc. Adapted from [96].

The motion of the grinding balls within the milling jars is complex and highly dependent on operational parameters such as rotational speed, filling ratio, and powder load. As these parameters vary, the motion transitions through different regimes, namely sliding, cascading, cataracting, and rolling (centrifuging) as illustrated in (figure 2.6) [98]. During sliding motion,

grinding balls move along the inner surface of the milling jar with limited detachment, resulting in low-energy frictional interactions rather than impactful collisions, and consequently contributing minimally to effective particle size reduction. In the cascading regime, balls are carried up the wall of the jar and fall back onto the powder bed with moderate energy. In the cataracting regime, which is generally preferred for energetic milling, balls are projected from the wall and impact the powder or opposite wall with high intensity, maximizing energy transfer. In contrast, in the rolling or centrifuging regime, balls adhere to the inner wall due to excessive centrifugal force, resulting in minimal relative motion and reduced grinding efficiency. Therefore, optimizing the operational conditions to maintain a cataracting motion is critical for achieving effective particle size reduction.

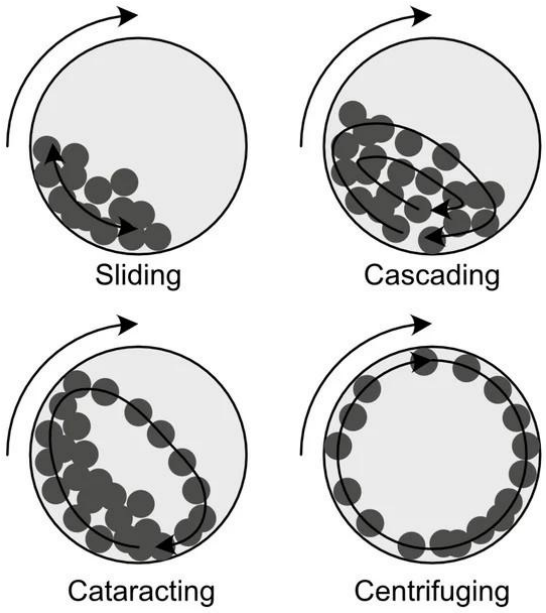

Figure 2.6: Motion of grinding beads: Sliding, Cascading, Cataracting and Rolling. Adapted from [98].

The effectiveness of the ball milling method is highly dependent on several critical parameters, which determine the energy input, coating quality, and reproducibility [70, 99]. One of the most important is the ball-to-powder ratio (BPR), which determines the frequency and intensity of collisions. A low BPR results in insufficient impact events and reduced grinding efficiency, while an excessively high BPR may hinder effective motion and increase wear. Similarly, the rotational speed of the mill directly affects the kinetic energy of the balls. While increasing the speed enhances impact energy, excessively high speeds can lead to centrifugation of the balls, halting the milling process and potentially causing excessive heating, which may alter the material properties or induce phase transformations. The milling time is another critical parameter that influences particle size and material composition. Initially, particle size decreases rapidly with increasing milling time; however, beyond a certain duration, the rate of size reduction diminishes,

reaching a steady-state equilibrium. Prolonged milling may also lead to increased contamination due to wear of the milling media and jars, which can affect the purity and chemical composition of the final product. The choice of grinding media is equally important. Typically, milling balls are made from hard and inert materials such as stainless steel or ceramics (e.g., zirconia) to ensure effective energy transfer while minimizing unwanted chemical reactions. The density and size of the balls influence the impact energy, with larger and denser balls generating higher collision forces. However, the use of excessively large or irregularly sized balls can lead to uneven grinding and increased abrasion. Therefore, selecting an appropriate combination of ball size, material, and quantity is essential for optimizing the milling process. An important distinction in PBM is between dry and wet grinding. In dry milling, powder particles are milled without any liquid medium, allowing direct transfer of impact energy, which is effective for particle size reduction and mechanical alloying. However, dry milling often leads to particle agglomeration and poor heat dissipation. In contrast, wet milling involves the addition of a solvent or dispersant, which provides several advantages including improved heat management, enhanced homogeneity, reduced agglomeration, and easier recovery of milled particles. Solvents such as ethylene glycol, isopropyl alcohol (IPA), and deionized water are commonly used, and they also facilitate the formation of stable nanoink suspensions for subsequent thin-film fabrication. Nevertheless, wet milling may introduce complexities such as unintended chemical reactions or surface modifications, which can influence the functional properties of the material. Additional factors affecting the PBM process include the use of dispersants or process control agents, milling atmosphere (e.g., air, inert gas, or vacuum), and temperature. Dispersants help reduce particle agglomeration by lowering surface energy, while controlled atmospheres can prevent oxidation or contamination. Temperature influences diffusion processes and phase stability, further affecting the final material properties.

2.2.2 Materials and Experimental Milling Conditions

Materials

Two different ZnO powder purity grades were used (99% purity, Anachemia and 99.9% purity, Fisher), isopropanol (IPA; Laboratory grade, Fisher), and ethylene glycol (EG; 99% purity, BDH) and deionized water (DI water) were used as received.

PBM Experiment

PBM was used in this research as the primary nano-grinding and mechanochemical fabrication technique due to its versatility, efficiency, and suitability for producing nanostructured materials as discussed in (section 2.2.1) above. The milling conditions (speed; 200 rpm to 1000 rpm and time; 10 minutes to 120 minutes) were varied while maintaining all other processing parameters constant for a given material batch, ensuring a controlled investigation of its influence on particle

size reduction and material properties. The grinding process was performed using a Fritsch Pulverisette 7 planetary ball mill (premium line), as illustrated in (figure 2.5a). This system is equipped with two grinding stations and is well-suited for the efficient and wear-resistant milling of hard, medium, and brittle materials, achieving fine particle sizes. The milling was conducted in silicon nitride jars with a capacity of 80 mL, selected to minimize contamination and ensure chemical stability during processing. Zirconia beads (Zr) with a diameter of 2 mm (total mass of about 100 g) were used as the grinding media due to their hardness and inert nature. A typical ball-to-powder ratio of approximately 20:1 was employed. For each batch, around 7 g of zinc oxide (ZnO) powder was milled in the presence of approximately 10 to 15 mL of liquid medium, such as ethylene glycol (EG), Isopropyl alcohol (IPA) or deionized (DI) water. This liquid-assisted grinding approach, often referred to as colloidal grinding, was used to enhance dispersion, reduce agglomeration, and promote the formation of stable nanoink suspensions suitable for subsequent thin-film deposition.

Milling Process

To ensure safe operation of the planetary ball mill, it was essential that the grinding jar and the corresponding counterweight jar were carefully balanced using a mechanical scale. Any imbalance in mass could lead to excessive vibrations and potentially hazardous conditions during high-speed milling. The preparation of the milling setup followed a specific sequence. Initially, the grinding beads were loaded into the empty jar, followed by the ZnO powder and subsequently the selected solvent. Care was taken during handling and assembly of the milling jars to prevent contamination or improper sealing. Once filled, the jars were securely closed by tightly locking the lids and further sealed with parafilm to prevent leakage during operation. After assembly, the milling parameters were programmed into the planetary ball mill's programmable interface, including rotation speed, total grinding duration, number of grinding cycles and intermittent pause intervals. A typical grinding batch set parameters is (Speed = 200 rpm; Grinding time = 5 mins; Pause = 5 mins; Cycles = 2; Revers = off) and summarized in (table 1.1) is the sequence for this work. The inclusion of pause (rest) periods was particularly important, as significant heat is generated inside the grinding chamber due to friction and repeated balls. These rest intervals allowed the system to dissipate heat, thereby preventing excessive temperature rise that could affect material properties or damage the equipment. During each pause, the jars were inspected for any signs of leakage, and built-up internal pressure was carefully released. This step is crucial because interactions between the ZnO powder and solvent during milling can lead to pressure accumulation inside the sealed jars. Controlled pressure release helps prevent potential hazards such as jar rupture or mechanical failure. Furthermore, for conditions involving higher rotational speeds or extended milling durations, longer rest intervals and multiple grinding cycles were adopted to ensure both operational safety and process stability.

Trials	Speed (rpm)	Duration (mins)	Rest time (mins)	Dispersant
EG sequence	200 rpm to 1000 rpm	10 mins to 120 mins	5 mins to 12 mins	Ethylene glycol (EG)
IPA sequence	200 rpm to 600 rpm	10 mins to 30 mins	5 mins to 10 mins	Isopropyl alcohol (IPA)
DI sequence	200 rpm to 600 rpm	10 mins to 30 mins	5 mins to 10 mins	DI water (DI)

Table 1.1: Parameters of the grinding trials used in this study for various substrates.

Extraction Process

Upon completion of the grinding cycle, the milled suspension was carefully extracted using a specialized emptying device provided by the manufacturer. The extraction setup consisted of several components, including a syringe, syringe pump tip, funnel lid, O-rings, seals, adapter and stainless-steel mesh. After removing the handle from the grinding jar, an O-ring was first positioned at the top to ensure proper sealing. Subsequently, the adapter, a thin seal, stainless-steel mesh (mesh has a size of 0.8 mm), and a thick seal were assembled sequentially. Once the assembly was complete, the syringe was securely attached to the funnel lid. The jar containing the milled suspension was then inverted and gently shaken in a vertical motion to dislodge any material adhering to the inner surfaces. The suspension, along with entrapped air, was drawn into the syringe and expelled through repeated pumping cycles, typically 2–5 times, to facilitate effective extraction. Since the initial extraction does not completely recover all the material, additional solvent is introduced into the emptied syringe and transferred back into the grinding jar. This step helped resuspend the remaining particles, and the extraction process was repeated multiple times, typically between five and seven cycles, to maximize recovery. Each extracted fraction was collected in separate vials, with progressively decreasing particle concentrations, and was labeled accordingly for further analysis and processing. As illustrated in (figure 2.7) below, one of our PBM grinding experiments in which ZnO was milled in EG solvent for 10 minutes at 400 rpm and later extracted into 4-dram vials.

a) b)

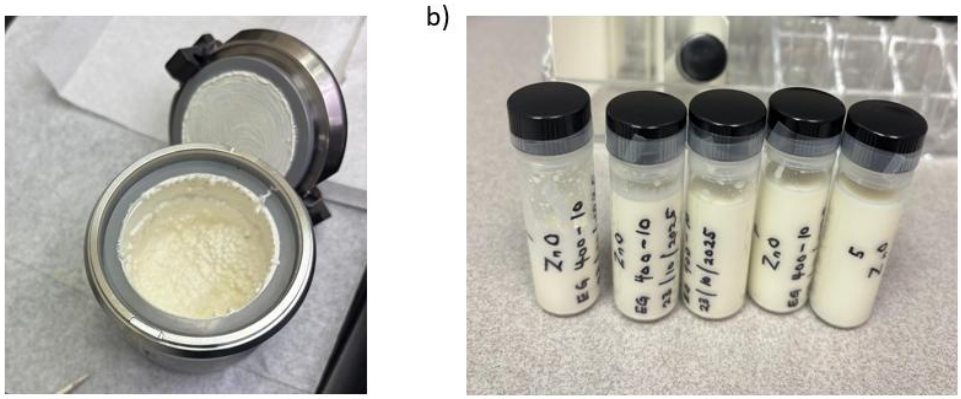

Figure 2.7: (a) ZnO material after completion of grinding cycle (EG 400-10). (b) The suspension's extraction showing different suspension densities (left to right shows decreased density order).

2.2.3 Preparation of ZnO Thin Films

Nanoink Concentration Control

The concentration of grounded ZnO nanoinks was controlled through a combination of re-dispersion, centrifugation, and solvent volume adjustment processes to obtain inks with tailored solid content suitable for thin-film deposition. Initially, all prepared samples underwent shaking for approximately 2 minutes, followed by ultrasonication for at least 10 minutes under semi-wave conditions (sonication parameters varied depending on homogeneity of nano ink in the vial). This step ensured proper dispersion of ZnO nanoparticles within the solvent and minimized agglomeration prior to further processing. Subsequently, the samples were subjected to centrifugation under varying conditions to separate particles based on size and density (typically, 10,000 rpm for 10 minutes was used). After centrifugation, all the supernatant was carefully removed using disposable and micro pipets, leaving behind a sediment composed of relatively larger or more concentrated ZnO particles. The amount of retained sediment was controlled depending on the desired final concentration of the nanoink. To prepare inks of specific concentrations, a controlled volume of solvent (IPA, EG or DI water), ranging from 0.1 mL to 1 mL, was added back to the sediment. Each solvent has different physicochemical properties, such as viscosity and density, which influence dispersion stability and ink behavior during deposition. After solvent addition, the samples were again shaken and sonicated to ensure homogeneous redistribution of ZnO particles, resulting in stable nanoink. The concentration of each nanoink was quantified in terms of weight percentage (wt%), calculated using the ratio of the mass of ZnO sediment to the total mass of the solution (sediment plus solvent) as illustrated in the (equation 3 and 4) below;

$$\text{Wt \%} = \frac{\text{mass of solute (g)}}{\text{mass of solution (g)}} \times 100 \quad (3)$$

$$\text{Wt \%} = \frac{\text{mass of ZnO sediment (g)}}{\text{mass of ZnO sediment (g)} + \text{mass of solvent (g)}} \times 100 \quad (4)$$

Accurate measurements were ensured by accounting for the average mass of empty epi tubes used, which was determined to be approximately 0.9851 g. This allowed precise determination of the sediment mass after removal of the supernatant. The experimental results demonstrated a wide range of achievable concentrations, spanning from as low as ~1.6 wt% for highly diluted suspensions to above 80 wt% for highly concentrated suspensions. These variations highlight the strong dependence of nanoink concentration on centrifugation parameters, solvent type, and sediment recovery strategy. The concentration control method was then optimized to produce functional and homogeneous nanoinks with concentrations between (55 to 80 wt%). Overall, this concentration control methodology enabled the preparation of ZnO nanoinks with tunable solid loadings, which is critical for optimizing film thickness, uniformity, and functional performance in subsequent ink deposition and thin-film sensor fabrication.

Thin Film Fabrication Using Adjustable Blade Applicator

Once the desired concentration of ZnO nanoink was obtained, thin films (between 15 µm to 50 µm) were fabricated using an adjustable blade applicator, which is a widely adopted technique for producing uniform coatings over large substrate areas [100]. This method relies on the controlled spreading of a nanoparticle-based suspension (nanoink) across a substrate surface, enabling precise regulation of film thickness and uniformity. Typically, the coating solution consists of dispersed ZnO nanoparticles along with suitable solvents and, where necessary, additives to enhance stability, adhesion, and film formation. The fundamental principle of this technique involves maintaining a fixed gap between the applicator blade and the substrate surface. As the blade moves relative to the substrate, the nanoink is uniformly spread, forming a wet film that subsequently dries to produce a solid thin layer. In this work, an adjustable film applicator equipped with dual micrometers (KTQ-II (50 mm)) was used to precisely control the blade-to-substrate distance. This setup allows fine adjustment of the wet film thickness over a wide range, typically from tens to several thousand micrometers, depending on the application requirements. To ensure accurate thickness control, calibrated gauges (ranging from approximately 20 to 1000 µm) were used to set the gap between the blade and the substrate. The micrometers were adjusted until the blade made uniform contact with the gauge along its length, ensuring a consistent coating thickness. After calibration, the gauge was removed, and the coating process was initiated. The applicator was then drawn across the substrate using a steady

and controlled motion to minimize streak formation and thickness variations. Drops around 5-10 µL of the ZnO nanoink was carefully deposited at one end of the substrate using a micropipette, after which the applicator blade was drawn across the surface to print the ink uniformly as shown in (figure 2.8).

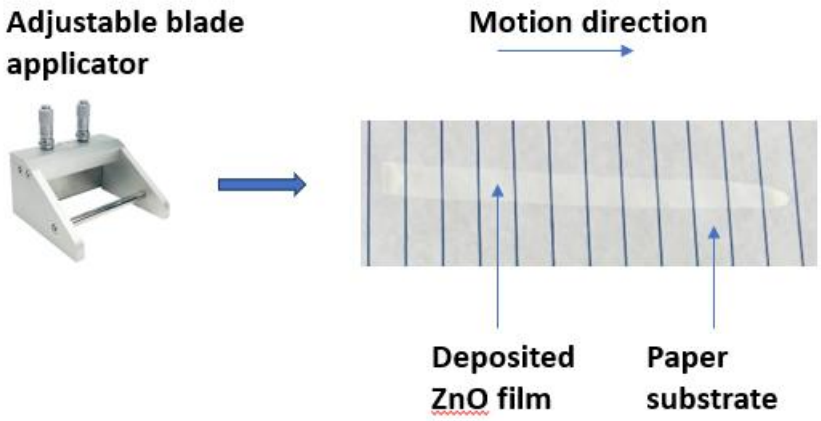

Figure 2.8: Printing of ZnO ink on flexible substrate (paper) via adjustable blade applicator.

The quality of the resulting film depended not only on the set gap but also on operational factors such as the speed of application, applied pressure, and consistency of motion. Manual operation may introduce slight variations; therefore, maintaining consistent technique was essential for reproducibility. Substrate preparation played a critical role in achieving high-quality films. Glass substrates were thoroughly cleaned and, where necessary, treated to improve surface wettability and adhesion. The substrates were placed on a level surface or secured using holders to prevent movement during coating. Maintaining a leveled platform was essential to avoid thickness gradients caused by gravitational flow of the liquid film. Following deposition, the films were subjected to controlled drying conditions (room temperature, oven and hotplate) depending on the substrate type. The drying process significantly influences the final morphology and uniformity of the film. For solvents such as isopropyl alcohol, rapid evaporation allowed drying at approximately 130 °C for 5 to 10 minutes, whereas viscous solvents like ethylene glycol required longer or higher-temperature drying to ensure complete solvent removal.

Various low-cost substrate types used

A key advantage of the solution-based ZnO nanoink approach employed in this work lies in its compatibility with a wide range of low-cost and unconventional substrates. Unlike traditional microfabrication techniques that rely on expensive and rigid platforms, the adjustable blade

applicator method enables uniform thin-film deposition on both rigid and flexible materials, thereby significantly expanding the applicability of the fabricated sensors. Some of the substrates employed in this work are as follows;

Rigid substrates such as glass slides, ceramics and silicon wafers which provide smooth, chemically stable, and thermally robust surfaces, making them ideal for controlled studies of film morphology and intrinsic sensing performance. These substrates minimize surface roughness effects and allow for better reproducibility, which is essential during material characterization. Similarly, anodized alumina offers a highly ordered porous structure that can enhance surface area and improve gas adsorption, potentially leading to increased sensor sensitivity. In contrast, flexible and disposable substrates including aluminum foil, sticky notes, plain paper, lined paper, filter paper, and cardboard highlight the low-cost and scalable nature of the fabrication process. Paper-based substrates are particularly attractive due to their porosity, lightweight nature, and widespread availability. For instance, filter paper provides a fibrous and highly porous network that promotes increased surface interaction between the ZnO nanostructures and target gas molecules. However, this same porosity can also introduce variability in film uniformity and electrical pathways. Plain and lined papers serve as ultra-low-cost platforms, with the added advantage of enabling direct electrode patterning using pencil-drawn interdigitated electrodes, as explored in this work. Foil substrates offer mechanical flexibility combined with moderate conductivity, which can be advantageous for certain sensor configurations. Cardboard, while less uniform, demonstrates the feasibility of deploying sensors on recyclable and biodegradable materials. Sticky notes introduce an adhesive backing, enabling easy integration onto various surfaces for potential real-world sensing applications. Plastic polymer substrates, such as transparencies, provide a balance between flexibility, optical transparency, and smoother surfaces compared to paper. These substrates are particularly useful for applications requiring lightweight and semi-flexible devices, although their thermal limitations must be considered during processing. Overall, our use of these diverse low-cost substrates underscores the versatility of the ZnO nanoink deposition technique. It enables the development of scalable, disposable, and application-specific gas sensors while also allowing a better investigation of how substrate properties such as roughness, porosity, and flexibility affect thin-film morphology and sensing performance.

2.2.4 ASTM D3359 adhesion tape test

The ASTM D3359 adhesion tape test is a standardized method used to evaluate the adhesion strength of thin films and coatings on various substrates [101]. This test involves making a series of cuts on the coated surface, typically in a cross-hatch or ‘X’ pattern, followed by the application and removal of a pressure-sensitive adhesive tape. The extent of coating removal after tape peeling is then assessed and classified according to a rating scale ranging from 0B to 5B, where 5B indicates no coating detachment (excellent adhesion) and 0B represents significant coating

removal (poor adhesion). The test can be performed using either Method A (X-cut) or Method B (cross-hatch), depending on coating thickness and application requirements. In the context of ZnO thin films (film thickness ≤125 µm), this technique provides a simple and effective means of assessing film-substrate adhesion, which is critical for ensuring mechanical stability, durability, and consistent sensor performance. Strong adhesion is particularly important for flexible and low-cost substrates such as paper and polymers, where poor bonding may lead to film delamination during handling or operation. In our research, we present initial results on adhesion tape test trials for a few samples (glass slide, cardboard and yellow sticky note) as shown in (figure 2.9 (a), (b) and (c) respectively). Even though these are just initial tests, these samples show moderate adhesion on the various substrate types (~1B to 3B).

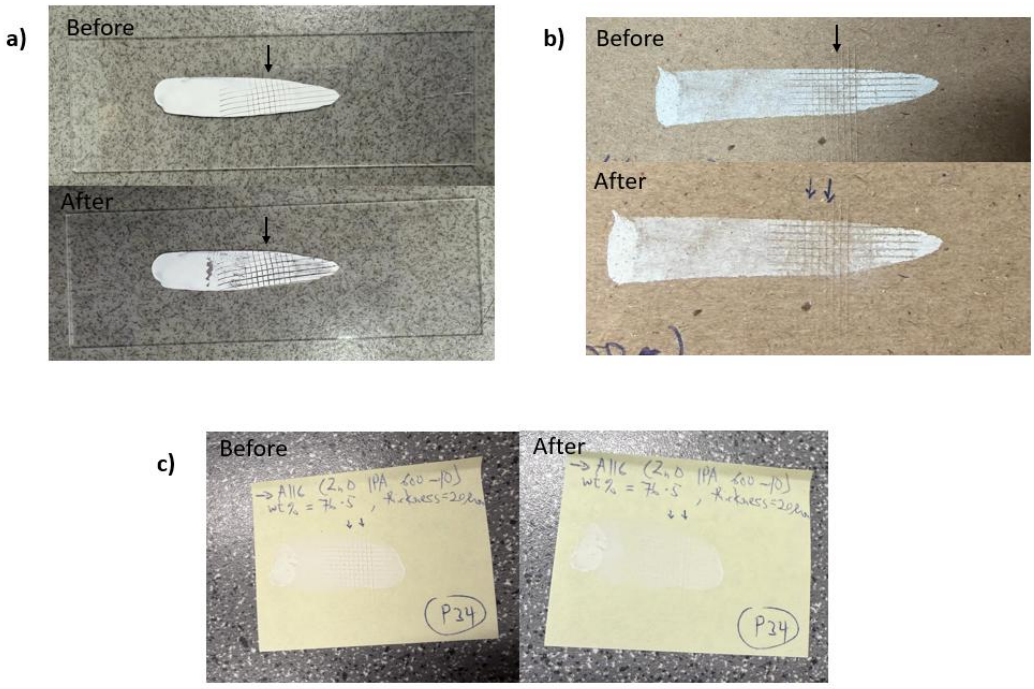

Figure 2.9: Before and after ASTM D3359 tape adhesion test of ZnO thin films on (a) glass slide, (b) cardboard substrate, and (c) sticky note.

2.2.5 Material Characterization Techniques

To analyze the structural, morphological, and compositional properties of the fabricated ZnO nano inks and thin films in this research, a range of material characterization techniques was employed to determine the influences on the properties of ZnO. Surface topography and nanoscale morphology were examined using a Nanonics MultiView 1000 atomic force microscope (AFM), integrated with an Olympus BXFM optical microscope, providing detailed insight into

surface roughness and particle distribution. High-resolution imaging of the nanostructures was further achieved through scanning electron microscopy (SEM) and transmission electron microscopy (TEM), with SEM and associated analysis carried out using a HITACHI S-2600 system, enabling visualization of particle size, shape, and film uniformity. In addition, Raman spectroscopy was performed using a Renishaw inVia Raman microscope, with spectra collected under ambient conditions using a 632.8 nm He-Ne laser, to investigate vibrational modes, crystallinity, and defect states of the ZnO nanomaterials. Ultraviolet–visible (UV-Vis) spectroscopy was utilized to evaluate optical properties such as absorption behavior and bandgap estimation. Furthermore, energy dispersive X-ray spectroscopy (EDX), was used to determine elemental composition and confirm material purity. Collectively, these instruments and techniques provide a better understanding of the physical, chemical, and optical characteristics of the ZnO thin films.

Raman Spectroscopy

In Zinc Oxide Raman spectroscopy, some phonon modes appear strongly, some are weakly polarized, and others are forbidden because Raman scattering, polarization geometry and Raman selection rules are governed by the conservation of energy and momentum [102]. ZnO has a wurtzite hexagonal crystal structure belonging to the C_{6v} symmetry group, which determines which vibrational modes are Raman-active, infrared-active, or silent. Raman-active modes are lattice vibrations that produce a change in the polarizability of the crystal and can therefore be detected in Raman scattering measurements. Infrared-active modes are vibrations that induce a change in dipole moment and are observable through infrared absorption spectroscopy, while silent modes are neither Raman-active nor infrared-active because they do not produce significant changes in either polarizability or dipole moment under normal selection rules [103]. Figure 1. shows energy band modulation by polarization, the bold dashed lines indicate the energy band in the absence of polarization. In ZnO, the appearance and intensity of these phonon modes are also strongly dependent on the polarization configuration and crystal orientation during measurement.

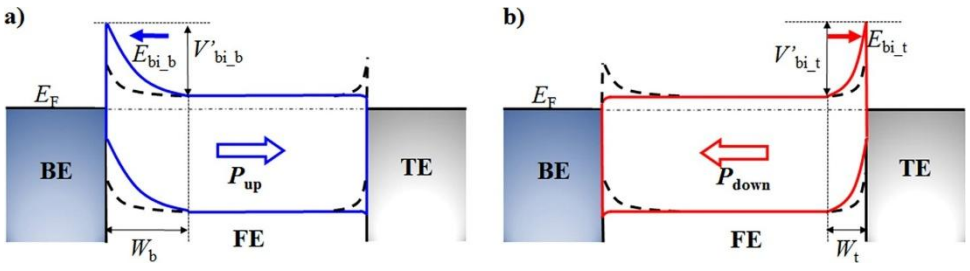

Figure 2.10: Effect of polarization on Schottky barrier formation and band bending for thin ferroelectric films. (a) shows upward polarization facilitating charge transport in one direction, while (b) shows downward polarization reversing the band bending and transport direction. Adapted from [104].

Based on group theory analysis, the vibrational spectrum consists of two A_1, two E_1, two E_2, and two B_1 modes [105]. Among these, the B_1 modes are Raman inactive, while the remaining modes contribute to the Raman response. The fundamental optical phonon frequencies for ZnO are typically observed at approximately 99 cm^{-1} for E_2(low), 437 cm^{-1} for E_2(high), 380 cm^{-1} for A_1(TO), 574 cm^{-1} for A_1(LO), 407 cm^{-1} for E_1(TO), and 583 cm^{-1} for E_1(LO). The low-frequency E_2 mode is primarily associated with vibrations of the heavier zinc sublattice, whereas the high-frequency E_2 mode arises from oxygen atom vibrations. Additionally, second-order vibrational modes appear around 208, 334, and within the range of 1050–1200 cm^{-1}. For highly oriented ZnO thin films under normal incidence of light, Raman selection rules permit only the A_1(LO) and E_2 modes to be observed, while other modes remain forbidden. Experimental Raman spectra of ZnO films deposited at varying substrate temperatures align well with these theoretical predictions, showing peaks near 99 cm^{-1} for E_2(low), 438 cm^{-1} for E_2(high), approximately 380 cm^{-1} for A_1(TO), and 579 cm^{-1} for A_1(LO). The presence of the prominent E_2(high) peak is an indicator of the wurtzite crystal phase. Also, an increase in ZnO powder purity enables improved control over crystal growth, leading to finer grains, more uniform structures, and better-developed crystallinity. This is reflected in the observed decrease in vibrational peak intensity ratios with decreasing crystallite size, consistent with reported trends in Raman studies [106].

Transmission Electron Microscopy (TEM)

Transmission electron microscopy (TEM) is a characterization technique used to investigate the internal structure and morphology of ZnO nanomaterials at the nanoscale. By transmitting a high-energy electron beam (typically 20–300 kV) through an ultrathin specimen [107, 108]. TEM enables direct imaging of nanoparticles and thin films with spatial resolutions down to 0.2 nm. This allows for precise evaluation of particle size, morphology, and crystallinity. High-resolution TEM (HRTEM) provides lattice-resolved imaging, where atomic planes and interplanar spacings can be directly measured. For wurtzite ZnO, characteristic lattice fringes are typically observed with d-spacing values of approximately 0.28 nm for the (100) plane, 0.26 nm for the (002) plane, and 0.24 nm for the (101) plane, consistent with standard crystallographic data [109]. These values confirm the formation of a well-defined hexagonal wurtzite structure. In addition, selected area electron diffraction (SAED) patterns exhibit distinct diffraction rings or spots corresponding to the (100), (002), (101), (102), and (110) planes. The presence of concentric rings indicates a polycrystalline structure, while sharp spots suggest localized single-crystalline domains. Quantitative particle size analysis from TEM images often shows an average particle diameter of ~10–100 nm, depending on milling conditions and processing parameters [110]. This nanoscale size distribution is critical for gas sensing applications, as smaller particles provide a higher surface-to-volume ratio, enhancing adsorption of gas molecules and improving sensor sensitivity. Overall, TEM provides both qualitative and quantitative insights into the nanostructure of ZnO thin films. The combination of particle size distribution, lattice spacing measurements, and

diffraction analysis enables a good understanding of how nanoscale features influence the structural and functional performance of ZnO-based sensors.

Scanning Electron Microscopy (SEM)

Scanning electron microscopy (SEM) is also a widely used characterization technique for examining the surface morphology and microstructural features of nanomaterials. In SEM, a focused electron beam (typically operating in the range of 0.3–30 kV) scans across the sample surface, generating secondary and backscattered electrons that provide high-resolution images of surface topography [111]. SEM enables visualization of thin-film uniformity, grain structure, surface roughness, and the distribution of nanostructures over large areas, with spatial resolutions typically on the order of 1–10 nm [112]. For ZnO thin films, SEM images commonly reveal granular or porous morphologies, depending on the fabrication and deposition conditions. The films often consist of interconnected nanoparticles or nanoclusters forming a continuous network. The degree of porosity and interparticle connectivity plays a crucial role in gas sensing performance, as porous structures facilitate gas diffusion and increase the active surface area available for adsorption. Cross-sectional SEM analysis can also be used to estimate film thickness, depending on deposition method and parameters.

Ultraviolet–Visible (UV–Vis) Spectroscopy

Ultraviolet–visible (UV–Vis) spectroscopy is a widely used optical characterization technique for analyzing the absorption and transmission properties of nanomaterials [113]. This technique measures the interaction of electromagnetic radiation, typically in the wavelength range of 200–800 nm, with the material, providing valuable information about its optical behavior, band to band transition and electronic structure. UV–Vis spectroscopy is particularly useful for determining the optical bandgap, absorption edge, and light-harvesting capabilities of semiconductor thin films. For ZnO films, a strong absorption edge is typically observed in the ultraviolet region, around 360–380 nm, corresponding to the intrinsic band to band transition of ZnO [114]. The bandgap energy can be quantitatively estimated using Tauc plots derived from UV–Vis absorption data, where extrapolation of the linear region of $(\alpha h\nu)^2$ versus photon energy ($h\nu$) provides the bandgap value [115]. Variations in the bandgap, typically within the range of can occur due to differences in particle size, defects, and fabrication conditions. In addition, UV–Vis spectra can provide insight into film quality and uniformity. A sharp and well-defined absorption edge indicates good crystallinity and low defect concentration, whereas a broadened edge may suggest structural disorder or the presence of defect states within the bandgap. Furthermore, UV–Vis measurements can be used to assess the optical transparency of thin films, particularly in the visible region (400–700 nm).

Atomic Force Microscopy (AFM)

Atomic Force Microscopy (AFM) is a high-resolution scanning probe technique used to characterize the surface morphology and topography of nanostructured materials [116]. The technique operates based on the interaction forces between a sharp probe tip (typically with a radius of curvature in the nanometer range) and the sample surface. As the tip scans across the surface, interatomic forces including van der Waals, electrostatic, and contact forces cause deflections of the cantilever, which are detected using a laser beam reflected onto a position-sensitive photodetector. These deflections are then converted into a three-dimensional topographical map of the surface with sub-nanometer vertical resolution. AFM measurements are commonly performed in different modes, including contact mode, non-contact mode, and tapping (intermittent contact) mode. Among these, tapping mode is most frequently employed for thin films to minimize surface damage and reduce lateral forces, making it particularly suitable for soft or nanostructured surfaces. The resulting AFM images provide quantitative information on surface roughness parameters such as root mean square (RMS) roughness, average roughness (Ra), and peak-to-valley height, which are critical for evaluating film uniformity and quality [117]. Furthermore, AFM phase imaging can provide additional insight into compositional uniformity and mechanical properties by mapping variations in tip-sample interactions. In well-crystallized films, uniform phase contrast typically indicates homogeneity, while irregularities may suggest defects, porosity, or secondary phases.

Energy-Dispersive X-ray Spectroscopy (EDX)

Energy-Dispersive X-ray Spectroscopy (EDX) is an analytical technique integrated with scanning or transmission electron microscopy (SEM/TEM) to determine the elemental composition and chemical purity of materials [118]. The technique is based on the interaction between a high-energy electron beam and the atoms within the sample. When the incident electrons strike the material, they can eject inner-shell electrons from atoms, creating vacancies that are subsequently filled by electrons from higher energy levels. This electronic transition releases X-ray photons with characteristic energies specific to each element, enabling qualitative and quantitative elemental identification. In the case of ZnO, the EDX spectrum typically exhibits prominent peaks corresponding to zinc (Zn) and oxygen (O). Characteristic emissions include the oxygen Kα peak around ~0.5–0.6 keV and zinc L and K lines near ~1.0 keV and ~8.4–9.6 keV, respectively [119]. The oxygen Kα peak is generally detected at approximately ~0.53 keV. The relative intensities of these peaks provide insight allowing assessment of the Zn:O atomic ratio. Beyond elemental identification, EDX provides quantitative information in terms of atomic percent (at%) and weight percent (wt%), which are crucial for evaluating film stoichiometry. In ideal ZnO, a Zn:O atomic ratio of approximately 1:1 is expected. However, deviations from this ratio can reveal important defect-related phenomena. For instance, oxygen-rich compositions (e.g., Zn:O ≈ 40:60) indicate a deficiency of zinc and an excess of oxygen, which is often attributed to the presence of interstitial oxygen (O_i) defects within the lattice [120]. Such oxygen-rich

stoichiometry contrasts with the more commonly reported n-type ZnO, where oxygen vacancies (V_o) and zinc interstitials dominate. EDX analysis also enables the detection of impurities or residual elements originating from precursors, substrates, or processing conditions.

Chapter Summary

This chapter presents the fundamental background, fabrication methodology, and experimental framework for the development of ZnO nanostructures and thin films for gas sensing applications. A mechanochemical top-down approach using planetary ball milling was employed to fabricate ZnO nanoinks, with variation of milling parameters such as speed, time, and solvent environment to tailor particle size, morphology, and defect concentration. These nanoinks were subsequently used to print thin films using an adjustable blade applicator, enabling controlled deposition on a wide range of low-cost rigid and flexible substrates. Additional procedures, including nanoink concentration tuning, and adhesion testing (ASTM D3359), were carried out to optimize film quality and mechanical stability. To evaluate the resulting materials, multiple characterization techniques were used; Raman spectroscopy, TEM, SEM, UV–Vis spectroscopy, AFM, and EDX—were employed to analyze crystallinity, nanostructure, surface morphology and elemental composition. Together, these techniques provide an understanding of how fabrication conditions influence material properties. The detailed experimental results and analysis corresponding to each characterization technique are presented and discussed in Chapter 4 of this thesis.

Chapter 3

3. ZnO Thin Film Gas Sensors

3.1 Multifunctional Applications of ZnO Thin Films

One of the most prominent applications of ZnO thin films lies in the field of electronics and optoelectronics, where their excellent transparency in the visible region and good electrical conductivity make them suitable candidates for transparent conductive oxides (TCOs) [121]. Traditionally, indium tin oxide (ITO) has been the dominant TCO material used in devices such as flat-panel displays, solar cells, light-emitting diodes (LEDs), and organic light-emitting diodes (OLEDs) [122]. However, the high cost and limited availability of indium have motivated the search for alternative materials. In this context, ZnO thin films, particularly when doped with elements such as aluminum (Al), gallium (Ga), or indium (In), have demonstrated comparable electrical and optical performance. Aluminum-doped ZnO (AZO), for instance, has been reported to exhibit low resistivity on the order of 10^{-5} Ω·cm while maintaining optical transparency exceeding 90%, making it a viable substitute for ITO in many applications [123].

The suitability of ZnO for optoelectronic devices is further enhanced by its direct wide band gap, which allows efficient emission and absorption of ultraviolet (UV) and blue light and is particularly well-suited for devices operating in the UV/blue spectral region. This includes UV photodetectors, laser diodes, and light-emitting devices. The high exciton binding energy of ZnO ensures stable excitonic emission even at room temperature, which is advantageous for achieving high-efficiency light emission. ZnO-based optoelectronics is sometimes combined with heterojunction architectures, where n-type ZnO is combined with p-type materials such as gallium nitride (GaN), silicon (Si), or copper oxide (Cu_2O) to achieving stable and reproducible p-type doping [84]. These heterostructures have demonstrated promising performance, particularly in UV light emission, thereby reinforcing the importance of ZnO thin films in next-generation optoelectronic systems.

In addition to their role in electronics, ZnO thin films have gained significant attention in gas sensing applications due to their high sensitivity, fast response, and compatibility with low-cost fabrication methods [124]. ZnO is an intrinsic n-type semiconductor, and its gas sensing mechanism is primarily based on surface adsorption and reactions. When exposed to air, oxygen molecules adsorb onto the ZnO surface and capture free electrons from the conduction band, forming ionized oxygen species. This process creates a depletion layer near the surface, resulting in increased electrical resistance. Upon exposure to reducing gases such as hydrogen, carbon monoxide, or methane, these gases react with the adsorbed oxygen species, releasing electrons back into the conduction band and thereby decreasing the resistance of the material. The magnitude of this resistance change is directly correlated with the gas concentration, enabling ZnO thin films to function as effective gas sensors. However, conventional ZnO-based gas sensors often require elevated operating temperatures to achieve sufficient sensitivity, as higher

temperatures enhance the kinetics of surface reactions [125]. This requirement introduces several limitations, including increased power consumption, reduced device lifetime, and potential safety risks, especially when detecting flammable gases. To address these challenges, significant research efforts have been directed toward enabling room-temperature sensing. One effective strategy involves nano-structuring ZnO to increase its surface-to-volume ratio, thereby providing a greater number of active sites for gas adsorption. Solution-based fabrication methods, such as those involving nanoinks and thin film deposition, allow precise control over film morphology, porosity, and particle size, which are critical factors influencing sensing performance. Furthermore, the incorporation of dopants and composite materials has been shown to enhance gas sensing properties [126]. For example, doping ZnO with noble metals such as gold (Au), palladium (Pd), and platinum (Pt) introduces catalytic sites that facilitate gas adsorption and improve charge transfer processes. Similarly, forming heterojunctions with other semiconductors, such as SnO_2 or graphene, can enhance sensitivity and selectivity by modifying the electronic structure and charge distribution at the interface. Optical activation using UV or visible light has also emerged as a promising approach to improve sensor performance at low temperatures by increasing carrier generation and promoting surface reactions.

Beyond sensing applications, ZnO thin films play a crucial role in photocatalysis and environmental remediation [127]. Due to their wide band gap and strong oxidizing power, ZnO materials can generate electron–hole pairs when exposed to UV light. These charge carriers participate in redox reactions that lead to the formation of reactive oxygen species (ROS), such as hydroxyl radicals and superoxide ions. These species are highly reactive and can effectively degrade organic pollutants, dyes, and harmful chemicals in water and air. As a result, ZnO thin films are widely used in photocatalytic applications, including wastewater treatment, air purification, and self-cleaning surfaces. The photocatalytic efficiency of ZnO is strongly influenced by its nanostructure and surface properties. Nanostructured ZnO thin films offer a higher surface area and increased density of active sites, which enhance adsorption and reaction rates. Additionally, controlling defects and doping can improve charge separation and reduce electron–hole recombination, thereby increasing photocatalytic performance. ZnO-based photocatalysts have been successfully used to degrade organic dyes such as rhodamine B under UV and solar irradiation, demonstrating their potential for environmental cleanup.

In the field of cosmetics and personal care, ZnO thin films are widely used for their UV-blocking and antibacterial properties. ZnO is an effective inorganic sunscreen agent capable of absorbing and scattering both UV-A and UV-B radiation [128]. Unlike organic UV filters, which may degrade under prolonged exposure to sunlight, ZnO exhibits excellent photostability and does not decompose easily. Furthermore, it is non-toxic, non-irritating, and safe for human skin, making it suitable for use in a wide range of cosmetic products, including sunscreens, lotions, and creams. The UV-blocking capability of ZnO is particularly important given the harmful effects of ultraviolet radiation, which can cause skin damage, premature aging, and increase the risk of skin cancer. In addition to UV protection, ZnO exhibits antimicrobial properties due to its ability to generate reactive oxygen species under light exposure. These properties make ZnO useful not only in

cosmetics but also it suitable for applications in healthcare, coatings, antimicrobial surfaces, textiles, and packaging materials.

Another emerging application of ZnO thin films is in radar absorbing materials and stealth technology [129]. Radar absorbing materials (RAMs) are designed to minimize the reflection of electromagnetic waves, thereby reducing the detectability of objects by radar systems. ZnO nanomaterials exhibit unique dielectric properties and can effectively absorb microwave radiation due to polarization losses and multiple scattering effects. The nanoscale morphology of ZnO enhances electromagnetic wave attenuation by increasing the interaction between the incident waves and the material. ZnO-based thin film absorbers also offer advantages such as low density, and environmental stability. These characteristics make them promising candidates for applications in military and aerospace technologies, where lightweight and efficient radar absorption is critical.

3.2 Gas Sensing Parameters

Main parameters affecting gas sensor performance

The performance of ZnO-based thin film gas sensors is evaluated through a set of well-defined parameters that collectively describe their responsiveness, reliability, and applicability in real-world environments. As illustrated in (figure 3.1) [130], these parameters include gas response (or sensitivity), selectivity, response time, recovery time, limit of detection (LOD), stability, and the influence of external factors such as analyte gas concentration, operating temperature, humidity, light and gas flow conditions. Understanding and optimizing these parameters is essential for the development of high-performance gas sensors, particularly for applications in environmental monitoring, industrial safety, and healthcare.

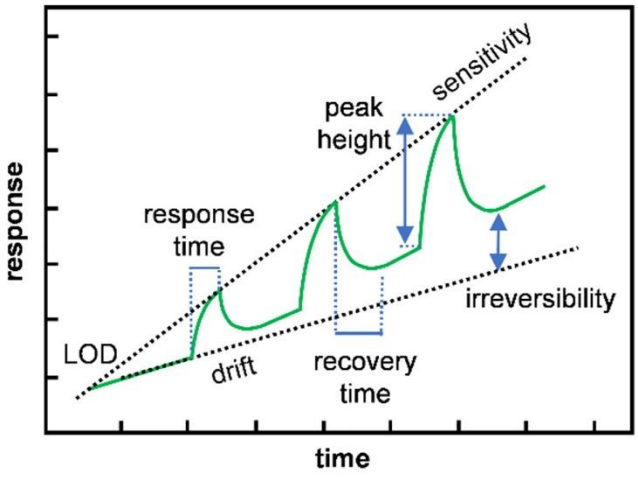

Figure 3.1: Graphical representation of several important performance parameters in a sensor exposed to increasing concentrations of analyte gas. Adapted from [130].

Sensitivity

A fundamental metric in gas sensing is the gas response, which quantifies the change in the electrical signal of the sensor upon exposure to a target gas, and the term sensitivity, often used interchangeably with response. In chemiresistive ZnO sensors, this is typically expressed as the ratio between the resistance or conductivity in air and the resistance or conductivity in the presence of the target gas. For n-type semiconductors such as ZnO, the response is commonly defined as, the ratio of Ra to Rg or, (Ra / Rg) for the reducing gases and the reciprocal for the oxidizing gases [131]. This parameter provides a direct measure of the detectability of a gas at a given concentration. Closely related to response is responsivity, which describes the rate of change of the sensor output with respect to gas concentration, typically expressed in units such as % ppm^{-1} or Ω ppm^{-1} [132]. While response indicates the magnitude of signal change, responsivity reflects how sensitively the device reacts to incremental concentration variations, making it particularly useful for calibration, linearity assessment, and comparison across different sensors or concentration ranges. The magnitude of the gas response is strongly influenced by the microstructural properties of the sensing layer. Factors such as grain size, porosity, and surface morphology play a critical role in determining how effectively gas molecules interact with the film surface and external factors such as temperature, humidity, and light also influence sensitivity. Increased porosity enhances gas diffusion into the sensing layer, allowing more active sites to participate in adsorption and reaction processes. High sensitivity is particularly desirable for detecting low concentrations of gases, especially near threshold limit values (TLV) or lower explosive limits (LEL).

Response time and recovery time

Another key performance metric is the response time, which represents the speed at which the sensor reacts to the introduction of a target gas. It is typically defined as the time required for the sensor signal to reach 90% of its final steady-state value after exposure (denoted as T_{90}) [133]. A shorter response time indicates a faster detection capability, which is critical in applications requiring real-time monitoring. Response time is influenced by several factors, including gas concentration, flow rate, temperature, and the intrinsic properties of the sensing material. Generally, higher gas concentrations lead to faster responses due to the increased availability of reactive species. Similarly, elevated temperatures can accelerate surface reaction kinetics, reducing response time. Complementary to response time is the recovery time, which measures how quickly the sensor returns to its baseline state after the removal of the target gas. It is typically defined as the time required for the sensor signal to recover to 10% ($T_{10,}$ or 90% return to baseline) of its original value. Fast recovery is essential for sensor reusability and continuous monitoring applications.

Analyte concentration

The analyte (gas) concentration itself plays a crucial role in determining sensor behavior [134]. In general, the sensor response increases with increasing gas concentration due to a higher probability of interaction between gas molecules and active sites on the ZnO surface. At low concentrations, a large number of active sites are available, leading to rapid and significant response. However, as concentration increases, these sites become progressively occupied, and the response begins to saturate. At very high concentrations, multilayer adsorption may occur, which can further the effective interaction between gas molecules and the sensing surface and may cause saturation. This saturation behavior highlights the importance of defining an optimal operating range for each sensor.

Temperature

Operating temperature is another critical parameter that significantly affects gas sensing performance [135]. Each metal oxide gas sensor typically exhibits an optimal working temperature at which the response is maximized. As temperature increases, the kinetic energy of gas molecules also increases, enhancing adsorption-desorption rates and facilitating faster surface reactions. This leads to improved sensor response up to a certain point. However, at excessively high temperatures, adsorbed gas molecules may desorb too quickly before reacting, resulting in a decline in sensor response. Therefore, identifying and maintaining the optimal operating temperature is essential for achieving maximum sensitivity and stability. In recent years, there has been a strong emphasis on developing room-temperature sensors to reduce energy consumption and improve safety.

Humidity

Humidity is another factor that can significantly influence sensor performance [136]. Water molecules adsorbed on the ZnO surface can interfere with gas sensing mechanisms in multiple ways. Firstly, they can occupy active sites, reducing the availability of sites for oxygen adsorption and subsequent gas reactions. Secondly, interactions between water molecules and adsorbed oxygen species can release trapped electrons back into the conduction band, thereby decreasing the baseline resistance. As a result, increased humidity often leads to reduced sensitivity and altered sensor response. Understanding and mitigating humidity effects is therefore crucial for reliable sensor operation, especially in real-world environments where humidity levels can vary widely.

Selectivity

Selectivity refers to the ability of a gas sensor to preferentially respond to a specific target gas in the presence of other interfering gases [137]. This is a critical parameter for practical applications, as real-world environments often contain multiple gas species. Selectivity is typically quantified using a selectivity coefficient, defined as the ratio of the sensor response to the target gas relative to that of an interfering gas under identical conditions. Achieving high selectivity with strategies such as doping, surface functionalization, and the formation of heterojunctions have been employed to enhance selectivity by tailoring surface chemistry and electronic properties. The selectivity is measured in terms of selectivity coefficient/factor as a ratio of target gas to another gas [138]. The general expression of the sensor's selectivity is expressed as;

$$\text{Selectivity coefficient (K)} = \frac{\text{Selectivity of the sensor toward interface gas (SA)}}{\text{Selectivity of the sensor toward interface gas(SB)}} \qquad (5)$$

Where, S_A and S_B are the responses of the sensor to a target gas A and an interference gas B, respectively.

Limit of detection

The limit of detection (LOD) defines the lowest concentration of a target gas that can be reliably detected by the sensor [139]. Alternatively, LOD can be defined as the concentration corresponding to a signal three times greater than the baseline noise. A low LOD is essential for applications requiring the detection of trace amounts of gases, such as environmental monitoring and medical diagnostics. The LODs for any target gas in sensors for environmental safety are driven by regulation (e.g. OHSE, WORKSAFEBC, etc) and must be abided by in commercialized systems to promote safety and rapid response to any hazardous environment.

Gas flow system and flow rates

Finally, the gas flow system and flow rates used during testing also influence sensor performance. Two primary configurations are commonly employed: static and continuous flow systems as elaborated in (equation 6 and 7). In a static system, a fixed volume of gas is introduced into a closed chamber containing the sensor, and the concentration of test gas is determined by volumetric dilution [140]. In contrast, a continuous flow system involves a constant flow of gas through the chamber, with the concentration controlled by adjusting the relative flow rates of the target gas and carrier gas using mass flow controllers [141]. Continuous systems provide control over gas concentration and are more representative of real-world conditions. The choice of flow system affects parameters such as response time, recovery time, and overall sensor stability.

Static system (trapped test gas in chamber);

$$C_{final} = C_{stock} \times \frac{V_{inj}}{V_{chamber}} \quad (6)$$

Where;

C_{final} = concentration of test gas in the chamber at equilibrium

C_{stock} = stock concentration in ppm introduced into the chamber through inlet

V_{inj} = volume of test gas (in mL) initially injected into the chamber

$V_{chamber}$ = total volume of test chamber (in mL)

Continuous flow system (constant flow of gas);

$$C_{steady} = C_{stock} \times \frac{V_a}{V_{total}} \quad (7)$$

Where;

C_{steady} = concentration of test gas in the chamber at steady state

C_{stock} = stock concentration of test gas flowing through the chamber

V_a = is the test gas volumetric flow rate

V_{total} = is the total gas volumetric flow rate (test gas + any other gasses).

Stability and reversibility

In addition to these primary parameters, stability and reversibility are crucial for long-term sensor performance [142]. Stability refers to the ability of the sensor to maintain consistent performance over repeated measurements and extended periods. This includes maintaining consistent sensitivity, response time, and baseline characteristics. Poor stability can lead to signal drift, inaccurate readings, and frequent recalibration requirements. Nanostructured materials, while offering high sensitivity, can sometimes suffer from reduced stability due to their high surface reactivity. Techniques such as annealing, doping, and composite formation are often employed to improve stability. Reversibility, on the other hand, refers to the ability of the sensor to return to its original state after exposure to the target gas, ensuring repeatable operation.

3.3. Sensor Device Fabrication

The fabricated ZnO films on a variety of substrates, with thicknesses ranging from approximately 15 µm to 50 µm, were subsequently utilized to develop functional gas sensors by establishing

reliable electrical contacts. The fabrication process primarily focused on integrating the ZnO sensing layer with suitable electrode configurations (as shown in figure 3.2) capable of accurately capturing current/resistance variations upon exposure to target gases.

A range of electrode materials and configurations were explored in this research to assess their effectiveness, cost-efficiency, ease of fabrication, and sustainability for scalable sensor development. ZnO films were either directly used as-deposited or carefully cut into smaller sections from larger coated substrates. These sections were then mounted onto glass slides using adhesive materials such as scotch tape or sticky adhesives. Initially, electrical contacts were established using combinations of copper (Cu) tape and conductive silver paint. Typically, Cu tapes were positioned either directly on the ZnO film or adjacent to it, and silver paint was applied at the interface to ensure good electrical contact between the electrode and the sensing layer. In addition to Cu tape and silver paint combinations, some devices were fabricated using only silver pens (~1.5 Ω) to draw interdigitated electrodes directly across the ZnO film surface. This method simplified the fabrication process. The silver-based conductive materials remain highly attractive due to their excellent electrical conductivity and chemical stability, making them suitable for laboratory-scale sensor development. To further explore low-cost, disposable and flexible alternatives, pencil-drawn interdigitated electrodes (IDEs) were introduced. In this method, graphite pencils of different grades (~7 kΩ for 2.5 cm line), specifically 6B, 4B and HB, were used to manually draw interdigitated patterns on paper substrates such as plain and lined papers, Oxford paper, and filter paper. ZnO thin films were then deposited directly over these patterned electrodes using a thin film applicator, followed by drying either at room temperature or in an oven at moderate temperatures (typically around 75 °C). To establish external electrical connections, carbon paint was applied at the terminal ends of the pencil-drawn electrodes and thermally cured to improve adhesion and conductivity. For more controlled device fabrication, gold (Au) patterned electrodes were employed. Using the thin film applicator, ZnO thin films were subsequently deposited straight onto the gold patterned electrodes. This was followed by drying, inside an oven set to a moderate temperature (typically near 75 °C). The precise patterning of Au interdigitated electrodes ensures uniform fields and reproducible sensor responses. However, the high cost makes this approach less suitable for low-cost or disposable sensor applications.

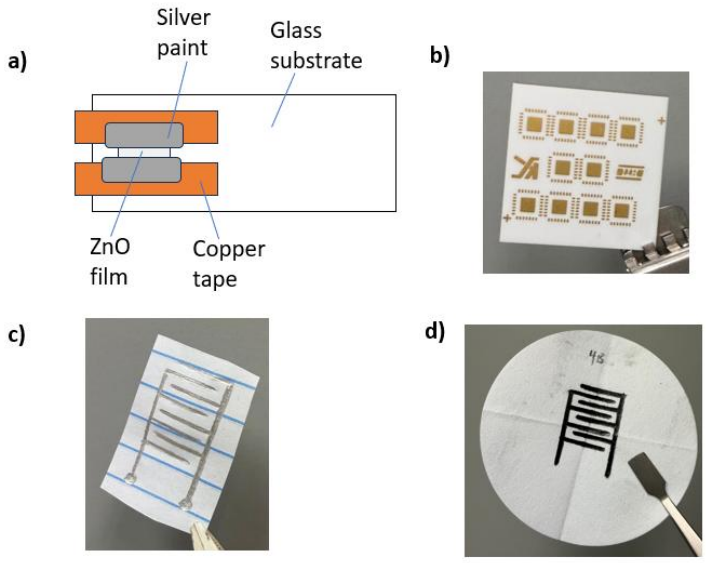

Figure 3.2: The various electrode configurations. a) Schematic diagram of ZnO thin film gas sensor device. b) gold (Au) patterned electrodes on ceramic substrate. c) silver pen drawn interdigitated electrodes on lined paper. d) Pencil (4B) drawn interdigitated electrodes on filter paper.

The choice of electrode material and configuration significantly influences the resistance, signal stability, and sensitivity of the sensor. Interdigitated electrode structures are particularly advantageous due to their ability to maximize the area between the sensing and the electrodes, thereby enhancing the measurable signal changes.

Thin film gas sensor samples

The fabricated thin film gas sensor samples are illustrated in (figure 3.3 (a) and (b)), highlighting the various electrode configuration. In (figure 3.3a), the sensing substrate consists of a filter paper with interdigitated electrodes. The thin film sensing material is deposited across the electrode region which provide a large active area for charge transport and enhance sensitivity to surface reactions. (Figure 3.3b) shows another configuration, where the films are deposited onto small substrates with conductive contacts formed using copper tape and silver paint. This configuration allows for easy electrical connection and controlled exposure to test gases. Overall, these techniques demonstrate a straightforward and reproducible fabrication approach for thin film gas sensors, combining interdigitated electrode design with practical mounting techniques to facilitate electrical measurements and gas exposure studies.

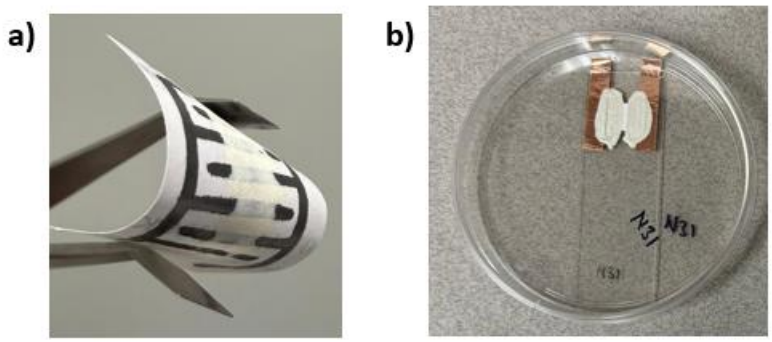

Figure 3.3: Fabricated ZnO thin film sensor devices on various substrates. (a) plain paper (b) glass slide substrate.

3.4 Experimental Gas Testing System

The gas sensing performance of the fabricated ZnO thin film sensors was evaluated using a customized quartz tube furnace–based testing system, to enable both static and continuous gas flow measurements under controlled conditions. The quartz tube served as the sensing chamber and was modified by capping one end (exhaust side) for static system, allowing injected test gases to be retained in the chamber without causing excessive pressure buildup. The sensing setup was integrated with mass flow controllers (MFCs) for precise gas delivery and a source-measure system (Keithley 4200-SCS system) for electrical characterization. All experiments were conducted under ambient room light at ambient temperature (~22 °C) and pressure. The ZnO sensor devices were mounted on a loader and inserted into the furnace. Electrical connections were established in a two-terminal configuration, ensuring stable current–voltage measurements as illustrated in (figure 3.4) below.

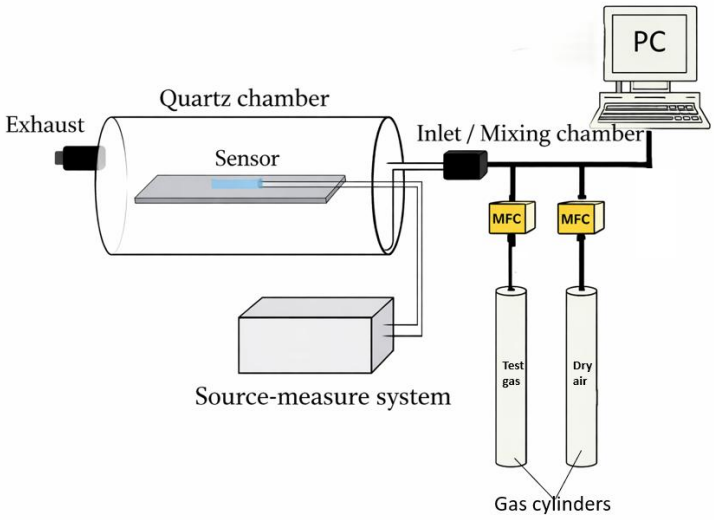

Figure 3.4: Schematic of the gas sensing experimental setup used in this research.

In the static gas testing mode, the chamber was used to trap test gas during exposure while in the continuous flow configuration the chamber containing the gas sensor served as a channel for the flow of test gas. A gas flow recipe (flow rates and time) was programmed on the PC. After each exposure, recovery steps were performed. This sequence enabled evaluation of sensor response and recovery behavior across varied gas concentrations. Electrical measurements were performed using a voltage sweep (from −2.5 V to +2.5 V) with a step size of 0.05 V to measure I-V characteristics of the fabricated sensors. Upon exposure to analyte gas, a constant bias of +5 V was then applied, and the current measured at 30 seconds sampling interval. All the electrical responses were recorded using the Keithley system and depending on gas concentration, flow rates and flow mode, across both configurations, response and recovery signals were consistently observed.

3.5 Chapter Summary

This chapter presented the development and evaluation of solution-based ZnO thin film gas sensors, highlighting their multifunctional properties and practical relevance. Key performance parameters, including sensitivity, response and recovery times, selectivity, and limit of detection, were discussed in detail. The influence of external factors such as gas concentration, operating temperature, humidity, and light was emphasized, as these significantly affect sensor performance. The chapter also outlined various gas sensor fabrication techniques, including conventional metal contacts and low-cost alternatives such as pencil-drawn interdigitated electrodes on flexible substrates. Finally, a description of a customized gas testing system which enabled controlled evaluation and electrical characterization of sensor behavior under static and continuous gas flow conditions.

Chapter 4

4. Results and Discussion

4.1 Film Morphology and Material Characterization

As described in (chapter 2), a series of characterization techniques were employed in our research to perform phase analysis, compositional characterization, structural and surface characterization, to determine the influences of preparation parameters (milling, different solvents, milling time, ZnO powder purity) on the properties of the thin films for gas sensing. UV–Vis measurements were conducted in collaboration with Dr. Anusha Venkataraman at Thompson Rivers University (TRU), and the data presented here were obtained using their instrumentation. SEM, TEM, and EDX data were acquired using instruments at the (UBC) Bioimaging Facility, University of British Columbia. Raman spectroscopy data were obtained using the Centre for Advanced Materials and Related Technology (CAMTEC) facility at the University of Victoria. Below are the results and discussion on the techniques used during this research.

Optical Microscopy

The Olympus optical microscope was used to evaluate the surface morphology, uniformity, and substrate interaction of ZnO thin films prepared under different milling conditions and solvents, as shown in (figure 4.1). The film deposited from ink milled at 400 rpm for 10 minutes in (EG) on a wafer slide (figure 4.1a) exhibits a relatively smooth and continuous surface with a boundary between coated and uncoated regions, indicating good particle dispersion at moderate milling conditions. In contrast, the sample prepared at 750 rpm for 90 minutes in EG on a foil substrate (Figure 4.1b) shows a rougher and more textured morphology, suggesting that higher milling energy and prolonged time lead to finer particles but also increased surface irregularities. The film produced at 200 rpm for 10 minutes in (IPA) on cardboard (Figure 4.1c) displays non-uniform coverage with visible paper fibers and clustered regions, indicating a thin and inconsistent coating that could be due to either low milling energy and the porous nature of the substrate. Meanwhile, the sample milled at 600 rpm for 10 minutes in (DI) water on a glass slide (figure 4.1d) demonstrates a comparatively uniform and smooth surface, though minor edge discontinuities are present. Overall, increasing milling speed improves particle dispersion but may also introduce roughness if excessive, while solvent and substrate selection strongly influence film formation. These morphological differences are significant for gas sensing performance, as surface roughness and uniformity directly affect active sites for gas adsorption and sensor response.

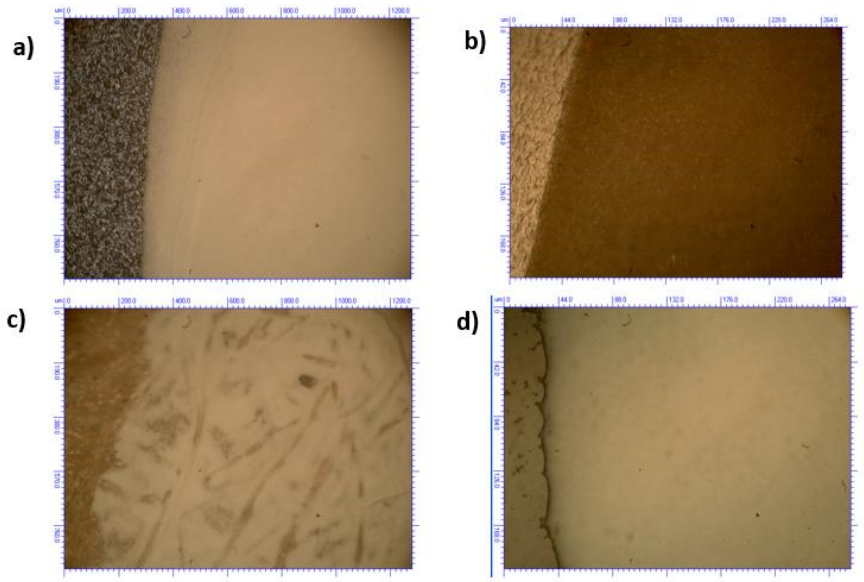

Figure 4.1: Olympus optical microscope images of ZnO thin films on various substrates. a) Films with ink milled at 400 rpm for 10 mins in EG on wafer slide at 10x magnification. b) Films with ink milled at 750 rpm for 90 mins in EG on foil substrate at 50x magnification. c) Films with ink milled at 200 rpm for 10 mins in IPA on cardboard at 10x magnification. d) Films with ink milled at 600 rpm for 10 mins in DI water on glass slide at 50x magnification.

Raman spectroscopy

Raman spectroscopy was employed to investigate the crystal structure, vibrational modes, and defect states of ZnO thin films prepared from bulk powder (green), and PBM-milled suspensions at 200 rpm (red) and 750 rpm (black) in EG as shown in (figure 4.2). The spectra exhibit several characteristic ZnO phonon modes, with differences in peak intensity and broadening as a function of milling speed. All samples show a dominant and sharp peaks at ~437.06 cm^{-1} (E_2 high) and ~99.04 cm^{-1} (E_2 low) which corresponds to the vibration of oxygen atoms and Zn atoms respectively in their lattice positions which is a signature of the wurtzite hexagonal crystal structure of ZnO, confirming that the crystal phase is preserved even after mechanical milling. The bulk sample (green) exhibits the highest peak intensity, indicating strong long-range crystalline order. Additional Raman modes are observed at ~196.13 cm^{-1}, ~332.23 cm^{-1}, ~384.49 cm^{-1}, and ~583.6 cm^{-1}. The modes around 332 cm^{-1} and 384 cm^{-1} are associated with multi-phonon processes (A_1(TO)/E_1(TO) modes) while the higher-frequency peak at ~583.6 cm^{-1} is commonly linked to defect-related vibrations, particularly oxygen vacancies and zinc interstitials. A trend is observed with increasing milling speed. The 200-rpm sample (red) retains relatively sharp and well-defined peaks, similar to the bulk material, indicating minimal structural disorder. In contrast, the 750-rpm sample (black) shows broader peaks and elevated background intensity, particularly in the regions around 300–400 cm^{-1} and ~580 cm^{-1}. In the 750-rpm sample, the

relative intensity of defect-related peaks (e.g., ~583.6 cm^{-1}) is higher compared to the bulk and 200 rpm samples. The intensity ratio of defect-related peak (~583 cm^{-1}) to the ~437.06 cm^{-1} (E_2 high) peak increases from approximately ~0.15 (bulk) to ~0.25 (200 rpm) and up to ~0.35–0.40 (750 rpm), indicating a significant rise in defect density with higher milling energy. This is consistent with the introduction of bulk and surface defects due to mechanical impact during PBM. The Raman analysis confirms that while the wurtzite ZnO crystal structure is maintained, increased milling speed (750 rpm) induces greater structural disorder and defect formation, as evidenced by peak broadening and enhanced defect-related modes. These defects can play a crucial role in gas sensing applications by increasing active sites for gas adsorption and enhancing surface reactivity, thereby providing a pathway to tune sensor performance through controlled milling conditions.

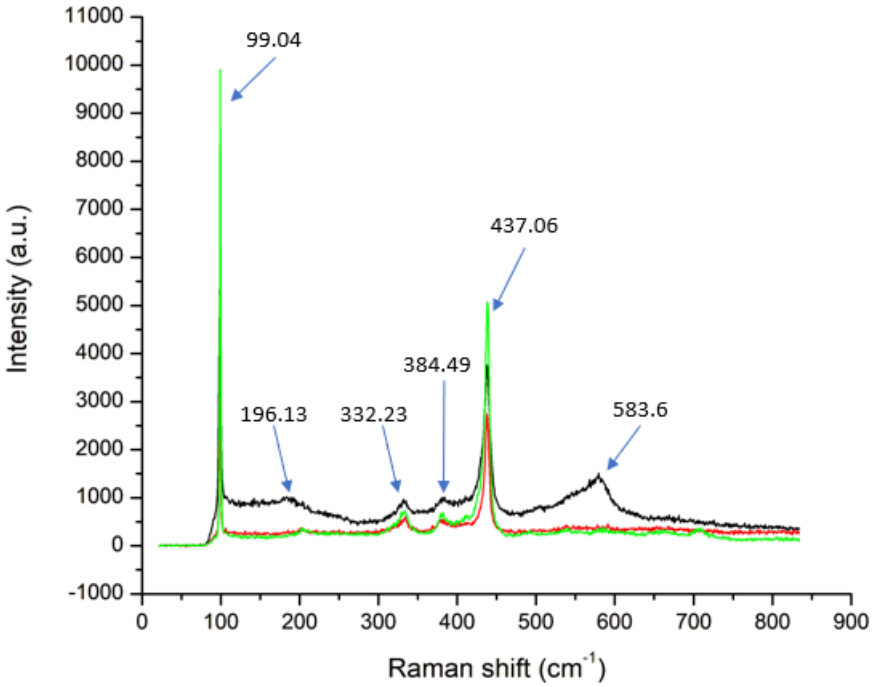

Figure 4.2: Raman spectra of ZnO thin films prepared from suspensions; bulk powder (green), milled at 200 rpm (red) and 750 rpm (black). All the spectra exhibit the first order high and low characteristic peak at 437 cm^{-1} and 99 cm^{-1} respectively, confirming the wurtzite hexagonal crystal structure of ZnO. The higher and broader satellite peaks of the 750-rpm sample indicate defect formation (bulk and surface) compared to the bulk material and 200 rpm samples, which can be used to tune sensor performance.

UV-Vis Spectroscopy

Ultraviolet–visible (UV–Vis) spectroscopy was used to characterize the optical properties of the ZnO nanoparticles (EG 200-10) and to estimate their optical bandgap. The absorption spectrum

(figure 4.3) shows a pronounced absorption edge in the near-UV region, with a distinct peak centered at approximately 380 nm, which is characteristic of ZnO and corresponds to its intrinsic band-to-band electronic transition. The absorbance gradually increases from ~0.45 at 300 nm to a maximum of ~0.68 at 380 nm, followed by a monotonic decrease toward longer wavelengths, reaching ~0.15 at 800 nm. This sharp absorption edge indicates strong excitonic absorption and confirms the high crystallinity of the ZnO nanoparticles. The absence of significant secondary peaks in the visible region suggests minimal defect-related states or impurities, which is consistent with well-processed ZnO via PBM. The optical bandgap (Eg) of the ZnO nanoparticles was estimated to be (3.26 eV) from the peak absorption wavelength using the relation:

$$Eg_{(eV)} = \frac{1240}{wavelength\ (\lambda_{nm})} \tag{8}$$

This value is in close agreement with the reported bandgap of bulk ZnO (~3.3 eV), indicating that the nanoparticles retain their intrinsic semiconductor properties with only minimal quantum confinement effects. The slight deviation may be due to size distribution, surface states, or minor lattice strain induced during PBM processing.

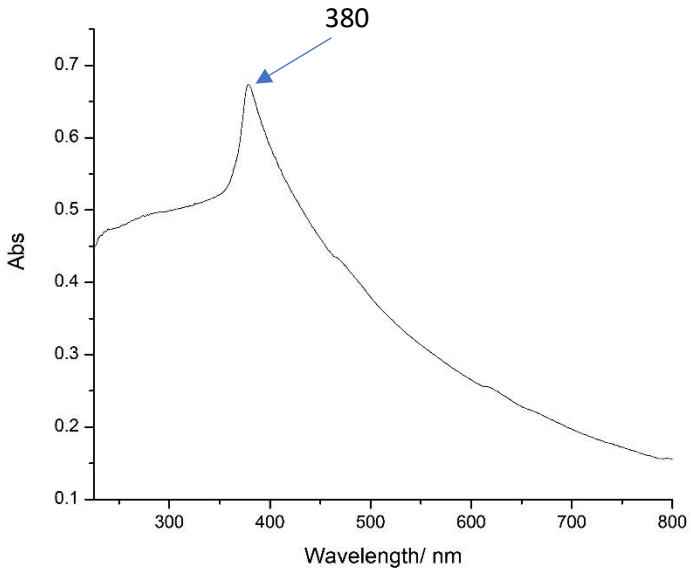

Figure 4.3: UV-Vis absorption spectrum of PBM processed ZnO nanoink (EG 200-10).

The UV–Vis results confirm that the mechanochemically fabricated ZnO nanoparticles exhibit a well-defined optical absorption edge with a bandgap of ~3.26 eV, validating their suitability for optoelectronic and gas sensing applications. The strong UV absorption and low visible-light absorption are particularly advantageous for UV-activated gas sensing mechanisms.

SEM

Scanning electron microscopy (SEM) was used to examine the surface morphology and microstructural features of ZnO thin films fabricated from nanoinks milled under different conditions and deposited on various substrates. This analysis is critical for understanding how milling parameters (speed and time) and substrate type influence the resulting film structure and, consequently, gas sensing performance. As shown in (figure 4.4), SEM images reveal distinct morphological differences between ZnO films prepared under different milling conditions. (Figure 4.4a) corresponds to films milled at 750 rpm and deposited on a paper substrate. The image shows a relatively rough and porous morphology, characterized by irregularly shaped agglomerates and packed nanoparticle clusters. The porous structure is likely enhanced by the intrinsic fibrous nature of the paper substrate, which promotes ink deposition and increased surface roughness. Such a morphology is beneficial for gas sensing applications, as it facilitates enhanced gas diffusion and provides a larger active surface area for adsorption. In contrast, (figure 4.4b) shows ZnO films milled at 200 rpm and deposited on a foil substrate. The morphology in this case appears more compact and structured, with well-defined particle shapes and relatively uniform grain distribution. The particles exhibit a more faceted and crystalline appearance, indicating reduced mechanical fragmentation due to the lower milling speed. This denser morphology may enhance electrical continuity but could limit gas diffusion compared to the more porous structure observed in the high-speed milled sample. Both images indicate that the observed features are within the sub-micron to micron range, with particle sizes generally consistent with nanoscale aggregates. The differences in morphology between the two samples highlight the strong influence of milling parameters and substrate properties on film formation. Higher milling speeds tend to produce smaller, more fragmented particles that aggregate into porous networks, while lower milling speeds preserve larger particle structures, resulting in denser films.

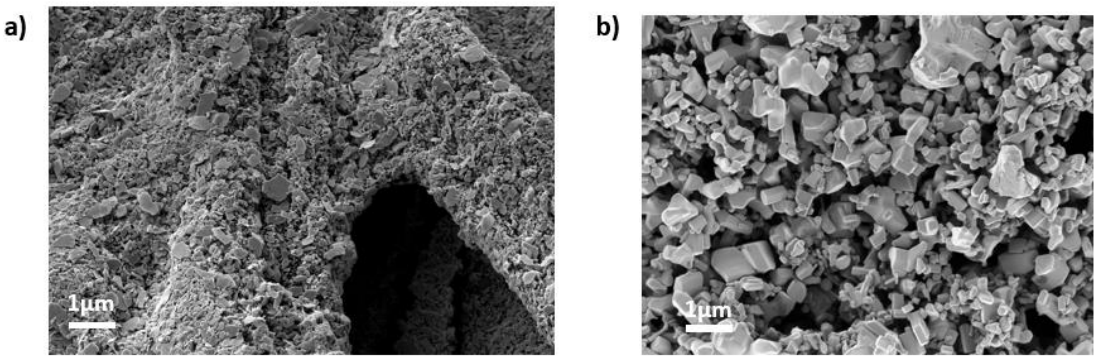

Figure 4.4: SEM images of the morphological structure and surface features of ZnO thin films milled at different speeds and time on various substrate; (a) ZnO-EG 750 rpm for 90 mins on paper substrate (b) ZnO-EG 200 rpm for 10 mins on foil substrate.

TEM

Transmission electron microscopy (TEM) was employed to further investigate the morphology, size distribution, and dispersion quality of ZnO nanoparticles after PBM in different solvent (IPA and DI water). As shown in (figure 4.5), distinct morphological differences are observed between the ZnO PBM-milled inks prepared in IPA (a) and DI water (b), though both also show platelet-like structures. For the ZnO nanoink dispersed in IPA (figure 4.5a), the TEM image reveals relatively well-dispersed nanoparticles with elongated and faceted morphologies. The particles appear less agglomerated, with sharper boundaries between individual grains, suggesting that IPA effectively reduces interparticle attraction during milling and stabilizes the dispersion. The observed particle sizes are generally within the sub-200 nm range and the reduced aggregation in IPA-based inks can be attributed to its lower polarity and viscosity compared to water, which minimizes particle clustering during both milling and subsequent drying. In contrast, the ZnO nanoink prepared in DI water (figure 4.5b) exhibits a higher agglomeration, with particles forming dense, irregular clusters. The individual particle boundaries are less distinct, indicating stronger interparticle interactions and possible re-agglomeration after milling. The clusters appear larger and more compact, which suggests that DI water promotes particle-particle adhesion due to its higher surface tension and hydrogen bonding effects. This aggregation behavior can lead to less uniform films upon deposition and potentially introducing increased porosity.

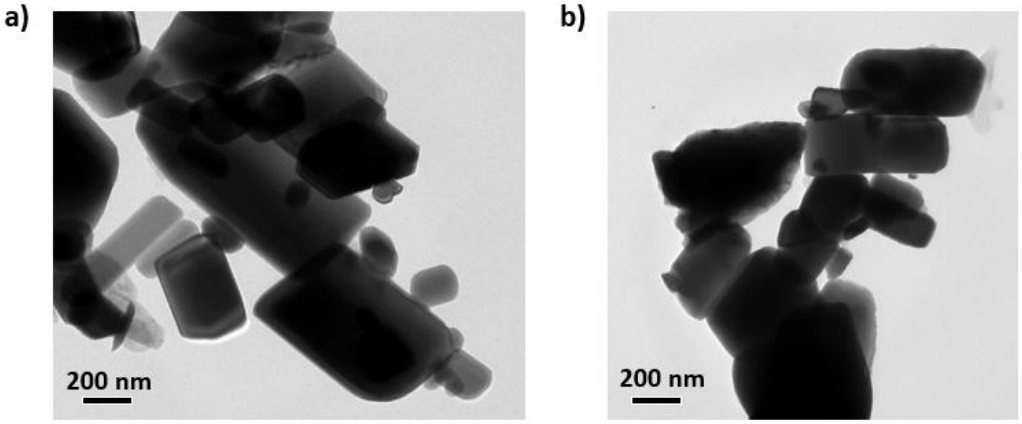

Figure 4.5: TEM of the morphology and size distribution of PBM processed ZnO nanoparticles in different ink suspensions. (a) ZnO in IPA (b) ZnO in DI water.

The TEM analysis confirms that solvent choice during PBM plays a critical role in determining nanoparticle dispersion and morphology. While IPA facilitates better particle separation and size control, DI water leads to increased agglomeration and cluster formation. These differences are

expected to directly influence thin film microstructure and, consequently, gas sensing performance, where a balance between surface area and film continuity is essential.

EDX

Energy dispersive X-ray spectroscopy (EDX) was employed to analyze the elemental composition and chemical purity of the fabricated ZnO thin films on paper substrate. The EDX spectrum obtained for the ZnO thin films milled at 200 rpm, as shown in (figure 4.6) and (table 4.1), exhibits prominent peaks corresponding to zinc (Zn) and oxygen (O), which confirms the formation of ZnO. The most intense peak is observed for Zn, indicating its dominant presence in the film, while a significant O peak further validates the oxide composition. Minor peaks corresponding to carbon (C) are also detected, which can be attributed to the underlying substrate of the film which is paper. Trace or negligible signals from other elements such as nitrogen (N) and selenium (Se) are observed but remain insignificant, suggesting high material purity. Quantitative analysis from the EDX results shows that Zn constitutes approximately 82.19 wt% (52.12 atomic %), while oxygen accounts for about 15.80 wt% (40.94 atomic %). Carbon contributes a minor fraction of approximately 2.01 wt%, while nitrogen and selenium are effectively negligible. The total composition sums to 100 wt%, confirming the reliability of the measurement. The slightly higher Zn content relative to oxygen may indicate the presence of oxygen vacancies, which are commonly observed in ZnO nanostructures and are known to play a significant role in enhancing gas sensing performance by acting as active sites for gas adsorption. Furthermore, the relatively uniform distribution of Zn and O elements across the analyzed region suggests good homogeneity of the thin films. The absence of significant impurity peaks indicates that the PBM fabrication and subsequent deposition processes did not introduce unwanted contaminants. These results validate the effectiveness of the fabrication process in producing high-purity ZnO nanoink films.

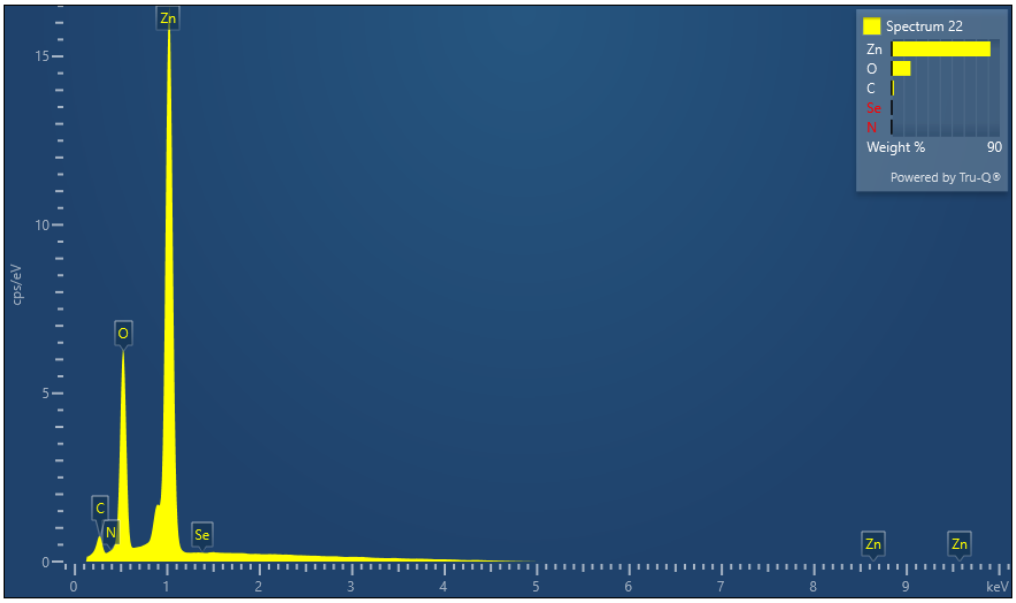

Figure 4.6: EDX measurement of elemental composition and chemical purity of the fabricated ZnO thin films (DI 200-10) on paper substrate.

Spectrum details									
Element	Signal Type	Line	Apparent Concentration	Intensity Correction	k Ratio	Wt%	Wt% Sigma	Atomic %	Standard Name
C	EDS	K series	0.15	0.64	0.00148	2.01	0.09	6.95	Pure Element
N	EDS	K series	0.00	1.26	0.00000	0.00	0.10	0.00	BN
O	EDS	K series	2.16	1.19	0.01890	15.80	0.13	40.94	SiO2
Zn	EDS	L series	8.55	0.91	0.08546	82.19	0.15	52.12	Pure Element
Se	EDS	L series	0.00	0.69	0.00000	0.00	0.18	0.00	Pure Element
Total						100.00		100.00	

Table 4.1: Spectrum details from the EDX analysis of the ZnO thin film, showing the weight percent (wt%) and atomic ratios of the relevant elements (Zn, O and C).

AFM

Tapping-mode atomic force microscopy (AFM) was used to analyze and determine the particle size distribution in bulk ZnO powder, as well as in thin films fabricated from nanoinks centrifuged under varying conditions (speed and time). This technique was essential in validating the theoretical predictions of ZnO nanoparticle sedimentation during centrifugation, which is critical

for the fabrication of thin films with controlled nanoparticle sizes to enhance gas sensing performance. The centrifuging time needed and the speed for a given size (e.g., 100 nm) ZnO particle sedimentation is given by Stoke's law;

$$v = \frac{w^2 r(p - L)d^2}{18n} \tag{9}$$

where w is radius speed of particles at radius r, p is particle density, L is density of solvent, d is diameter of particle, n is viscosity of solvent.

ZnO dispersed in ethylene glycol (EG) nanoink was used for this study. Sedimentation times for different particle sizes (100 nm, 500 nm, and 1000 nm) were calculated and experimentally verified. As illustrated in (table 4.2) below, images of extracted supernatant in vials and sediment of ZnO in epi tubes after completion of centrifugation process for the respective ZnO calculated particle sizes.

ZnO supernatant			
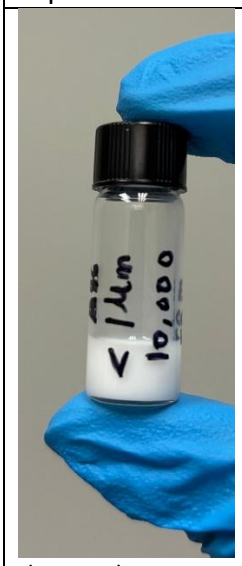			
(< 1 µm)	(< 500 nm)	(< 250 nm)	(< 100 nm)
ZnO sediment			

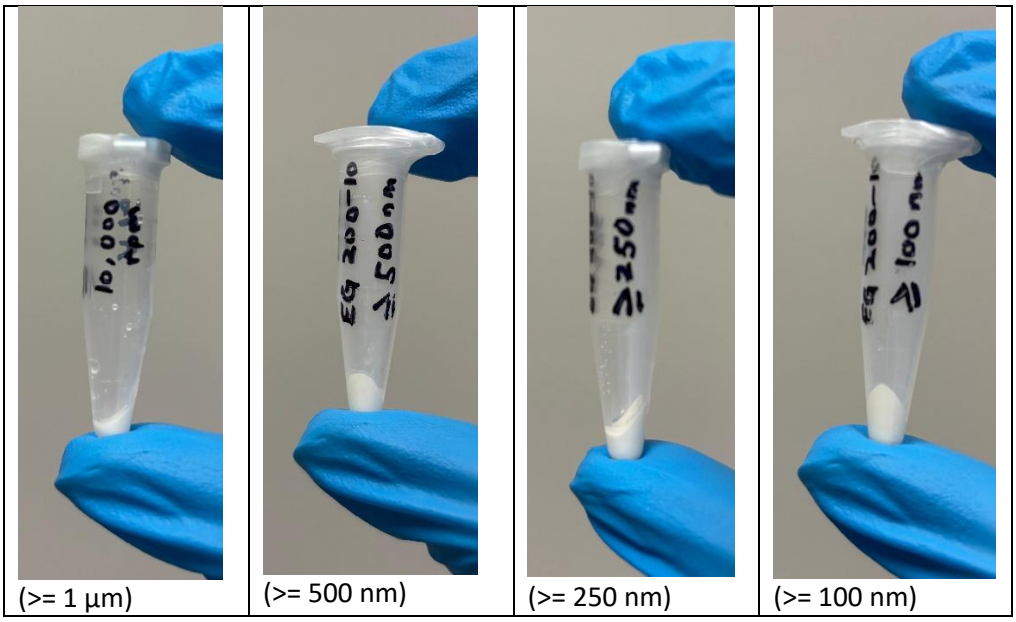

(>= 1 µm) (>= 500 nm) (>= 250 nm) (>= 100 nm)

Table 4.2: Labelled ZnO supernatant and sediment particle sizes after completion of centrifugation process.

Thin films were subsequently fabricated using the supernatants containing particles smaller than 100 nm, 500 nm, and 1000 nm, respectively. AFM analysis was then employed to confirm the resulting particle size distributions. As shown in (figure 4.7), AFM imaging revealed the formation of aggregated ZnO nanoparticles that assemble into continuous films bridging adjacent regions. The observed morphology suggests that nanoparticles self-organize during solvent evaporation, forming dense films interspersed with localized defect regions. Figures 4.7; (a), (b), and (c) present the AFM scanned images (left) and corresponding processed images (right), analyzed using WSxM software, for ZnO thin films with particle size distributions of <100 nm, <500 nm, and <1000 nm, respectively.

a)

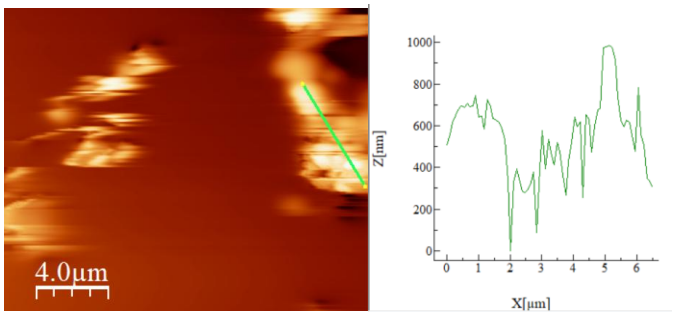

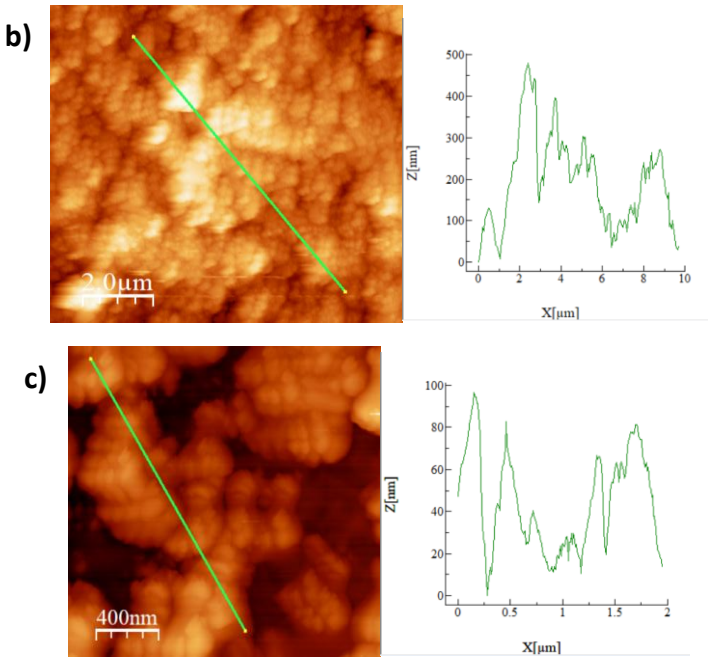

Figure 4.7: AFM analysis to determine the particle size distribution in bulk ZnO powder, as well as thin films fabricated from nanoinks centrifuged under varying conditions (speed and time). (a) ZnO bulk powder thin film (b) thin film particle size distribution for <500 nm (centrifuging: 5,000 rpm for 6.95 mins), and (c) thin film particle size distribution for <100 nm (centrifuging: 10,000 rpm for 43.5 mins).

Quantitative height analysis from the AFM measurements (green lines represent the area selected for height analysis) shows that the nanostructured features exhibit thicknesses consistent with theoretical predictions, with the largest particle sizes (corresponding to peak heights) measured to be approximately ~97 nm, ~480 nm, and ~990 nm for the <100 nm, <500 nm, and <1000 nm samples, respectively. Furthermore, AFM cross-sectional analysis highlights the presence of non-uniformities and defect regions within the films, where the height decreases significantly, in some cases to below ~5–10 nm. These gaps or discontinuities may arise from incomplete surface coverage during deposition or variations in solvent evaporation dynamics. While such defects can negatively affect film uniformity and electrical continuity, they may also enhance gas sensing performance by providing additional pathways for gas diffusion.

4.2. Gas Sensing Measurements

4.2.1 Sensing mechanism

The gas sensing mechanism in ZnO is a complex interplay between surface chemistry and electronic transport. The modulation of the electron depletion layer and potential barriers through adsorption–desorption dynamics and defect-mediated interactions form the fundamental basis for its sensing behavior. However, an excessive concentration of defects may also introduce instability or noise in the sensor response. Therefore, controlling the type and density of defects through mechanochemical fabrication and post-treatment processes is crucial for optimizing sensor performance. Surface states can also trap charge carriers, influencing both the baseline conductivity and the magnitude of response to gas exposure.

4.2.2 Initial gas sensing data

Preliminary sensing performance of the fabricated gas sensors were evaluated by monitoring the variation in electrical current under exposure to different gaseous environments (both continuous and static flow systems). The sensors exhibited distinct responses depending on the nature of the target gas and concentration, reflecting its sensitivity and selectivity characteristics. In dry air atmosphere, minimal increase in current was observed and a baseline established. This stable baseline confirms that any significant electrical variation in other environments arises from chemical interactions rather than external disturbances. In contrast, exposure to reducing gases such as hydrogen resulted in a pronounced increase in sensor current. This behavior is consistent with the reduction of adsorbed oxygen species on the sensor surface, leading to the release of electrons back into the conduction band and a consequent decrease in resistance. Other gases exhibited varying degrees of response depending on their reactivity and interaction strength with the sensing surface.

Prior to the gas sensing measurement, initial I-V measurement was performed on the sensors in a sweeping mode by sweeping voltage (-2.5 V to +2.5 V at 0.05 V step) and measuring current. As illustrated in (figure 4.8), I-V curve of our fabricated sensor (milled at 200 rpm for 10 mins in EG with film thickness of 20 microns on glass slide) in ambient light.

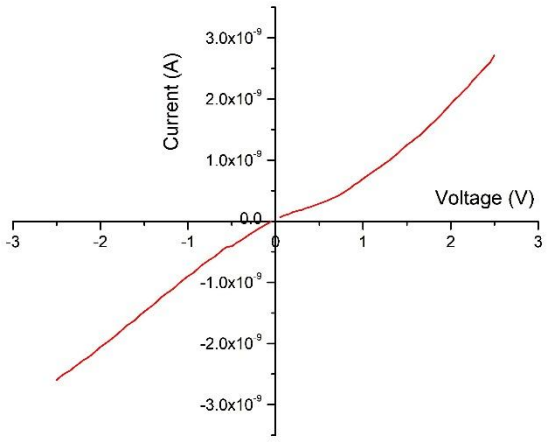

Figure 4.8: I-V curve of the ZnO thin film sensor by sweeping voltage (-2.5 V to +2.5 V at 0.05 V step) and measuring current.

After, a gas sensing recipe was programmed and the gas sensing experiment carried out. As illustrated in (figure 4.9), a continuous gas flow system was utilized and a flow recipe (air (45 mins)-pure hydrogen (45 mins)-air (45 mins)) at 500 sccm flow rate (with Ar purge in the beginning of recipe, 10,000 sccm) for the fabricated sensor (milled at 200 rpm for 10 mins in EG with film thickness of 20 microns on paper substrate)

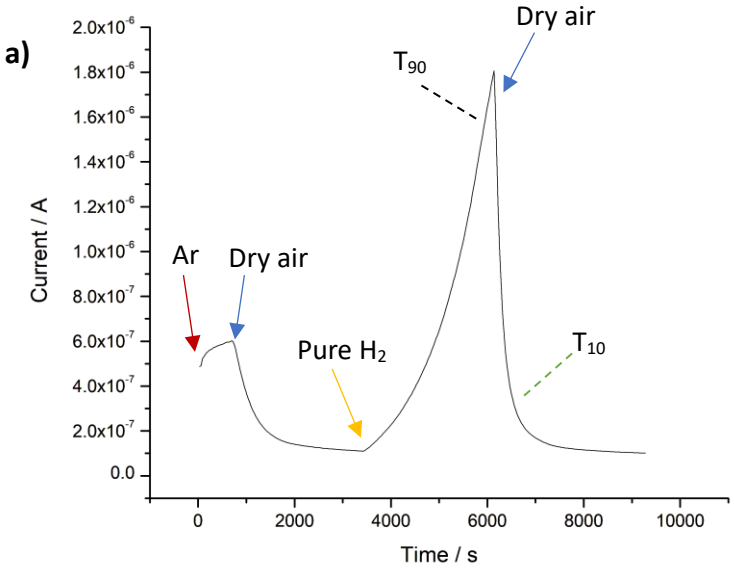

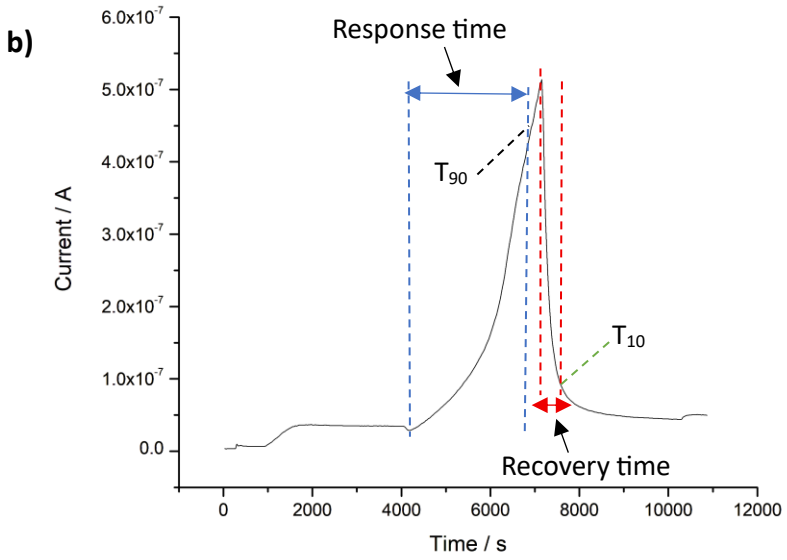

Figure 4.9: Electrical measurements of gas sensing in the ZnO thin film under a continuous gas flow system, following the sequence: air (45 min) – pure hydrogen (45 min) – air (45 min), at a flow rate of 500 sccm, with an initial Ar purge at 10,000 sccm. (a) EG 200-10 at 50 µm film thickness, on glass slide (b) EG 200-10 at 20 µm film thickness, on glass slide.

The transient response of the sensor provides important insights into its dynamic performance. Upon introduction of the target gas (H_2), the sensor current increased rapidly in time and this response time is governed by the rate of gas diffusion, adsorption kinetics, and surface reaction processes. Similarly, when the gas supply was removed and the sensor was re-exposed to air, the current returned toward its baseline value. The recovery time reflects the desorption of reaction products and re-adsorption of oxygen species. In general, faster response and recovery times are desirable for real-time sensing applications, and these parameters were found to vary depending on the sensor type, gas type and concentration, flow rates and operating conditions.

Different concentrations of the test gas (H_2) were also tested to determine the sensor's ability to detect low concentrations of analyte gas. As illustrated in (figure 4.10), a static gas flow system was utilized by flowing (for 120 seconds) and trapping a given volume of test gas into the tube furnace (of volume 5.56 litres) and a flow recipe (hydrogen (50 sccm, 100 sccm and 200 sccm respectively with Ar purge in the beginning of recipe, 10,000 sccm) for the fabricated sensor (milled at 200 rpm for 10 mins in EG with film thickness of 20 microns on paper substrate).

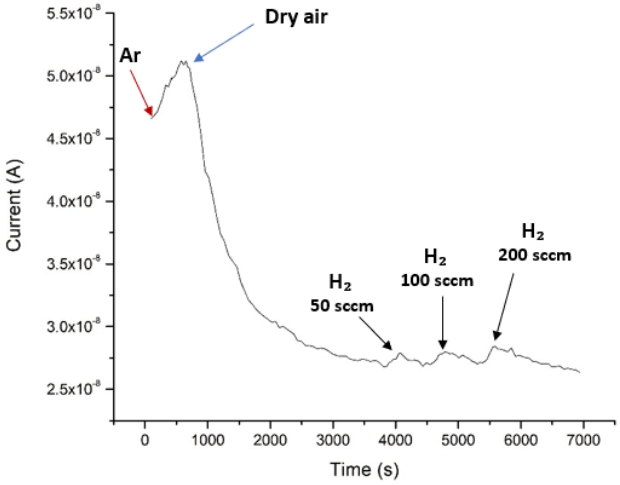

Figure 4.10: Electrical measurements of gas sensing in the ZnO thin film under a static gas flow system, following the sequence: (hydrogen (50 sccm, 100 sccm and 200 sccm respectively with Ar purge in the beginning of recipe, 10,000 sccm)).

At different flow rates of the target gas, a corresponding sensor response was observed. This relationship was generally nonlinear, particularly at higher concentrations (200 sccm). At low concentration (50 sccm), the sensor demonstrated measurable responses, enabling the estimation of detection limits. The minimum detectable concentration is determined by the signal-to-noise ratio and the stability of the baseline current, both of which are crucial for reliable sensing. Overall, the gas sensor data demonstrate an observable dependence of electrical response on gas type, concentration, and material properties. The observed trends highlight the importance of optimizing both the sensing material and operating conditions to achieve high sensitivity, fast response, and recovery time.

Effects of Light on Sensor Electrical Characteristics

Under dark conditions, the sensor exhibits very low current across the entire voltage range, indicating high resistance. This behavior is typical of semiconducting metal oxides such as ZnO, where charge carriers are limited due to the presence of surface-adsorbed oxygen species that trap free electrons. As a result, the conduction is suppressed, and the I–V curve remains nearly flat with minimal slope. When the sensor is illuminated with light of appropriate wavelength, a dramatic increase in current is observed, along with a much steeper and more linear I–V response. The electrical characteristics of the ZnO-based gas sensor are strongly influenced by optical excitation which further increases conductivity. In this study, ambient fluorescence broadband illumination light irradiation with an intensity of approximately (~ 3.0×10^{-2} W/m²) was used while taking gas sensing measurements. The broadband source, characterized by discrete emission peaks across the visible and near-UV regions, provides sufficient photon energy to interact with

the ZnO band structure. When the incident photon energy approaches or exceeds the bandgap (~3.26 eV), electron–hole pairs are generated within the material. The photogenerated holes migrate toward the surface and neutralize adsorbed oxygen species, while the electrons contribute to increased carrier concentration in the conduction band as illustrated in equation (10 and 11)[143] below;

$$O_2 + e^- \rightarrow O_2^-(\text{ads}) \quad \text{under dark conditiion} \tag{10}$$

$$h^+ + O_2^- \rightarrow O_2(\text{gas}) \quad \text{under illumination} \tag{11}$$

This process effectively reduces the width of the surface depletion layer and lowers the intergranular potential barrier, leading to an increase in conductivity. As a result, the baseline current of the sensor under illumination is elevated compared to dark conditions, reflecting enhanced charge transport across the nanostructured film. In addition to modifying the baseline electrical properties, light irradiation also impacts the dynamic gas sensing behavior. The presence of photogenerated carriers accelerates the adsorption–desorption kinetics by facilitating faster surface reactions between adsorbed oxygen ions and target gas molecules. This leads to improved response and recovery characteristics, as charge transfer processes occur more rapidly under illumination. Furthermore, the combination of nanoscale morphology, high defect density (e.g., oxygen vacancies), and porous film structure enhance light absorption and carrier generation efficiency, amplifying this effect. However, the relatively low illumination intensity suggests that the observed enhancement is moderate, primarily assisting in reducing response times rather than drastically altering sensitivity. Overall, optical activation introduces an additional degree of control over sensor performance, enabling improved electrical conductivity and faster dynamic response without the need for elevated operating temperatures.

4.2.3 Discussion and Analysis

Film Morphology and characterization analysis

The results presented in this work demonstrate a relationship between mechanochemical processing parameters, nanostructure formation, and gas sensing performance of ZnO thin films. This analysis quantitatively correlates particle size, defect density, and film morphology with sensor response characteristics. Atomic force microscopy (AFM) provided direct quantitative validation of particle size control through centrifugation. The extracted nanoparticle height distributions show maximum feature sizes of approximately ~97 nm, ~480 nm, and ~990 nm for the <100 nm, <500 nm, and <1000 nm heights, respectively. These values closely match theoretical sedimentation predictions based on Stokes' law, confirming that the centrifugation process effectively separates particles by size. Importantly, AFM cross-sectional analysis also

revealed localized regions with thicknesses as low as ~5–10 nm, indicating incomplete film coverage and nanoscale porosity. While such non-uniformities may degrade electrical continuity, they significantly enhance gas diffusion pathways and increase the density of active adsorption sites. Transmission electron microscopy (TEM) further supports these findings, showing the platelet-like structures of the ZnO nanoinks with particle sizes predominantly within the ~10 –100 nm range, depending on solvent and milling conditions. Additionally, solvent-dependent dispersion was observed: IPA-based inks produced sub-200 nm, well-dispersed particles, whereas DI water also produced sub-200 nm particles in larger agglomerates. This directly explains differences in film morphology observed in SEM, where higher milling speeds (750 rpm in EG) yielded porous, interconnected networks on paper, while lower speeds (200 rpm in EG) on foil produced denser, more compact films. Raman spectroscopy provided further quantitative insight into defect formation. Raman spectra of ZnO thin films printed from EG-based nanoinks under varying milling sequences were taken as shown in (figure 4.11). For samples milled at a constant speed of 200 rpm with different milling times (10 – 120 min), all spectra consistently exhibit the characteristic E_2(low) (~99 cm^{-1}) and E_2(high) (~437–440 cm^{-1}) modes, confirming the preservation of the wurtzite hexagonal structure. Minor variations in peak intensity and slight broadening with increasing milling time (figure 4.11a), suggest gradual changes in crystallite size and defect concentration. Similarly, for samples milled at a constant time of 10 minutes and 30 minutes with varying speeds (200 – 800 rpm and 200 – 750 rpm, respectively), the same characteristic peaks are observed, indicating structural stability across conditions. However, higher milling speeds result in reduced peak intensity and increased peak broadening (figure 4.11b and 4.11c), implying increased lattice disorder and defect formation due to more energetic milling. The intensity and broadening shoulder of the defect-related peaks indicated a substantial rise in oxygen vacancies and zinc interstitials with increasing milling energy. These defects act as electron donors and adsorption sites, playing a critical role in gas sensing and can be strategically exploited to enhance and tune gas sensing performance.

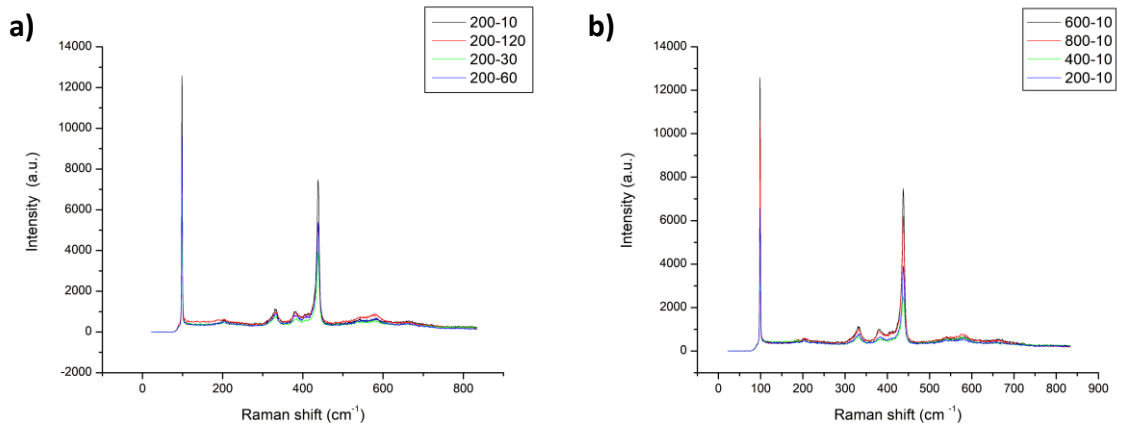

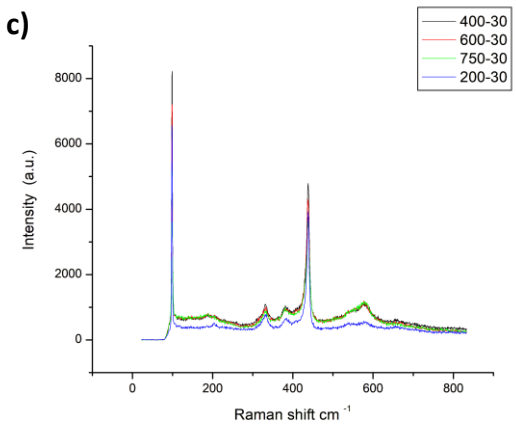

Figure 4.11: Raman spectra of printed films (EG) from different milling speed and time sequence (a) Constant milling speed 200 rpm at different milling times (b) Constant milling time 10 mins at different milling speeds (c) Constant milling time 30 mins at different milling speeds.

The Raman spectroscopy also allowed the analysis of ZnO bulk powder and ZnO thin films of different purities (99% and 99.9% powder purity). The quantitative analysis shows that peak positions remain essentially unchanged between 99% and 99.9% purity ZnO for both bulk powders and thin films. The fundamental E_2(high) and E_2 (low) modes were consistently observed at ~437– 438.85 cm^{-1} and ~99.02– 99.26 cm^{-1}, while second-order phonon modes appear at ~330–334 cm^{-1} and ~380–384 cm^{-1}, respectively, with negligible variation. Correspondingly the Raman intensity ratios from peaks coordinates were determined as shown in (figure 4.11). The intensity ratios show modest but noticeable differences, particularly in thin films. For bulk powders, the intensity ratios remain very similar between purities with YA/YB ≈7.10 –7.12 indicating minimal sensitivity to purity and defects. However, in thin films, the lower purity samples consistently exhibit reduced intensity ratios with YA/YB ≈ ~ 4.96 vs 6.55 (for 99% and 99.9% purities respectively), suggesting slightly higher defect density or reduced crystallinity. Overall, increasing purity from 99% to 99.9% leads to subtle improvements in crystallinity and grain refinement, reflected primarily in intensity variations rather than peak position shifts, indicating that Raman intensity ratios are more sensitive indicators of material quality.

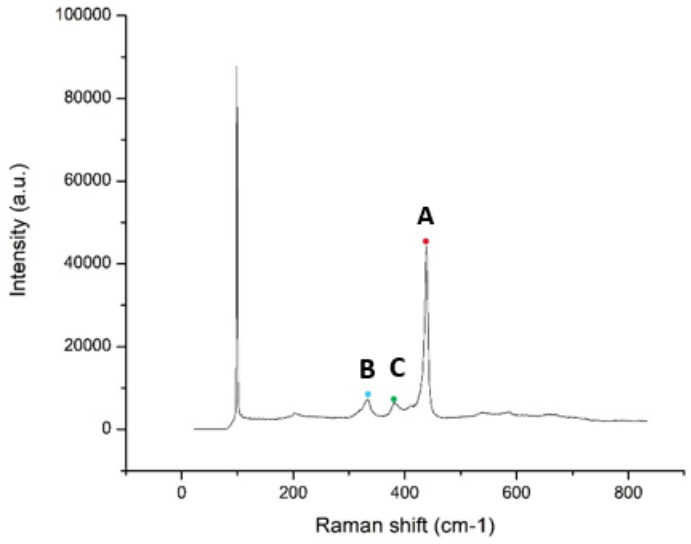

Figure 4.12: ZnO Raman spectra (A = fundamental first order optical mode, B = second order phonon mode and C = second order phonon mode)

This is supported by EDX results, which show a Zn-rich composition (~82.19 wt% Zn vs ~15.80 wt% O), further suggesting the presence of oxygen vacancies. UV–Vis spectroscopy revealed an absorption edge at ~380 nm corresponding to a bandgap of 3.26 eV, close to bulk ZnO (~3.3 eV) for nanoink milled in EG at 200 rpm for 10 mins. This indicates that while the material is nanostructured, quantum confinement effects are minimal, and the electronic properties remain suitable for stable semiconductor operation. Optical characterization allowed the estimation of ZnO particle sizes as a function of milling parameters (speed and time) as illustrated in (figure 4.12)

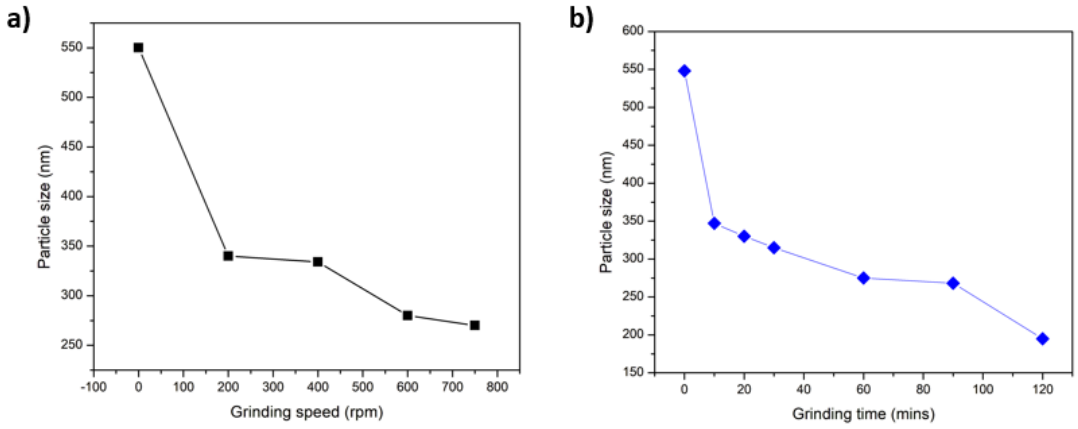

Figure 4.13: ZnO particle sizes as a function of milling speed and time (a) Average particle size of ZnO PBM nanoinks ground in EG at different speeds. (b) Average particle size of ZnO PBM nanoinks ground in EG at different grinding time.

Preliminary gas sensing data analysis

Response

The dynamic sensing performance of the ZnO-based chemiresistive sensor was evaluated from the transient current response curve. The response and recovery time, and gas response were determined. To calculate the gas response from the gas sensing plots, we use the response definition for n-type ZnO with a reducing gas (H_2); (Ra / Rg) and for normalized response (Ra - Rg / Ra = 1 – (Ia / Ig), at constant applied voltage). Using (figure 4.9) as worked example;

Baseline current in air (Ia); stable region before (H_2) gas exposure ~2500–3500 s: 0.12 × 10^{-6} A

Peak current during gas exposure (Ig); maximum at ~6000 s: 1.8 × 10^{-6} A

$$Response = 1 - \frac{0.12}{1.8} = 0.933$$

Response time

During response (rising edge): $I_{90\%}$ = 1.632 × 10^{-6} A

Gas exposure begins: ~ 3900 s

Current reaches 1.632 × 10^{-6} A: ~ 5800 s

T_{90} = 5800 s – 3900 s = 1900 s

Recovery time

During recovery (falling edge): $I_{10\%}$ = 0.288 × 10^{-6} A

Gas removed (peak): ~ 6000 s

Current drops to 0.288 × 10^{-6} A: 6500 s

T_{10} = 6500 s – 6000 s = 500 s

From the baseline region prior to gas exposure, the current in air was estimated to be approximately 0.12 × 10^{-6} A, while the maximum current under (H_2) gas exposure reached about 1.8 × 10^{-6} A, corresponding to a total current change of 1.68 × 10^{-6} A. Using the relation (Response = 1 – (Ia / Ig)) the sensor exhibited a response of approximately 0.933 (93.3%), indicating a significant change of resistance upon exposure to the reducing gas. For the transient analysis, the sensor reached the 90% response level at approximately 5800 s, relative to the beginning of gas

flow at around 3900 s, yielding a response time of about 1900 s. Upon gas removal at approximately 6000 s, the current decayed to the 10% level near 6500 s, corresponding to a recovery time of roughly 500 s. These results indicate a gradual response process, likely governed by adsorption kinetics and gas diffusion within the sensing layer, while the comparatively faster recovery suggests efficient desorption and good reversibility of the sensor.

Sample (milling condition and substrate)	Gas flow rates (sccm)	Response time (seconds)	Recovery time (seconds)
EG 200-10, 50 µm, film on glass slide	500 (dry air); 50, 100, 200 (H_2) (static flow)	~610 s	~560 s
EG 200-10, 20 µm, film on glass slide	500 (dry air); 50, 100, 200 (H_2) (static flow)	~670 s	~585 s
EG 200-10, 20 µm, film on paper substrate	500 and 690 in some tests (dry air); 50, 100, 200 (H_2) (static flow)	~750 s	~660 s
EG 750-90, 20 µm, film on paper	500 (dry air); 500 (H_2) (continuous flow)	~2100 s	~760 s
EG 400-10, 50 µm, film on glass slide	500 (dry air); 50, 100, 200 (H_2) (static flow)	~655 s	~570 s

Table 4.3: Summary of H_2 sensing response time, and recovery behavior across different film fabrication conditions.

The response and recovery characteristics for the various fabricated ZnO sensors on different substrates of different film thicknesses were also calculated and analyzed as summarized in (table 4.3). The ZnO thin film sensors fabricated under different milling conditions, thicknesses, substrates, and gas flow systems exhibited measurable responses to hydrogen, with response values ranging approximately from 0.03 to 0.95. Under continuous air–hydrogen–air flow conditions, higher responses were generally observed, particularly for films on glass substrates (up to ~0.93) and paper substrates (up to ~0.81). In co-flow hydrogen–air conditions, the response increased with gas flow rate (50 – 200 sccm), reaching up to ~0.95 for paper-based sensors, indicating improved sensing performance at higher hydrogen concentrations. Response times (T_{90}) varied between ~520 s and 2600 s, while recovery times (T_{10}) ranged from ~280 s to 760 s, depending on substrate type, film thickness, and operating conditions. Sensors on glass substrates generally showed faster recovery times, while paper-based sensors demonstrated good response magnitudes but slower recovery behavior. In static flow systems, both response magnitude and sensitivity decreased compared to continuous flow conditions, confirming the importance of gas delivery dynamics in sensor performance. More information on the individual sensor measurement is summarized in table A.1 in appendix-A.

Target gas concentration

Static system (trapped test gas in chamber)

For pure stock gas (H_2; concentration (C) of 10^6 ppm) injected into the furnace at 50 sccm (0.05 L/min), 100 sccm (0.1 L/min) and 200 sccm (0.2 L/min) respectively, given that $V_{chamber}$ is 5.56 L, hence, for 2 minutes, gas concentration at equilibrium is calculated as such;

$$\mathrm{C(H_2)}_{\,50\ \mathrm{sccm}} = 10^6\ \mathrm{ppm} \times \frac{0.05 \times 2}{5.56} = 17{,}986\ ppm$$

$$\mathrm{C(H_2)}_{\,100\ \mathrm{sccm}} = 10^6\ \mathrm{ppm} \times \frac{0.1 \times 2}{5.56} = 35{,}971\ ppm$$

$$\mathrm{C(H_2)}_{\,200\ \mathrm{sccm}} = 10^6\ \mathrm{ppm} \times \frac{0.05 \times 2}{5.56} = 71{,}942\ ppm$$

Continuous flow system

For pure stock gas (H_2; concentration (C) of 10^6 ppm) flowing constantly through the chamber, at equilibrium, the stock gas concentration is equal to the concentration of test gas flowing through chamber (). And for a co-flow continuous gas flow system of constant dry air flow at 500 sccm and H_2 at 50 sccm, 100 sccm and 200 sccm respectively, test gas concentration at equilibrium is calculated as such;

$$\mathrm{C(H_2)}_{\,50\ \mathrm{sccm}} = 10^6\ \mathrm{ppm} \times \frac{50}{550} = 90{,}909\ ppm$$

$$\mathrm{C(H_2)}_{\,100\ \mathrm{sccm}} = 10^6\ \mathrm{ppm} \times \frac{100}{600} = 166{,}667\ ppm$$

$$\mathrm{C(H_2)}_{\,200\ \mathrm{sccm}} = 10^6\ \mathrm{ppm} \times \frac{200}{700} = 285{,}714\ ppm$$

Based on the experimental results obtained in this work, the sensors demonstrate a dependence of response dynamics on processing conditions (film thickness, milling conditions, substrate, gas concentration and flow system). Films derived from moderate milling conditions exhibit improved response behavior due to an optimal balance between particle size reduction and surface accessibility. At lower milling intensities, larger particles result in reduced surface area, while excessive milling can lead to nanoparticle agglomeration, limiting effective porosity and slowing gas interaction. Consequently, an intermediate range of milling parameters provides the most favorable response and recovery characteristics by maximizing active surface sites while maintaining sufficient pore channels for gas transport. Further gas sensing measurements at even lower concentrations and with other test gases, could be used to determine the LOD, selectivity

of the sensors and also ascertain the effect of milling parameters on the performance of the fabricated sensors.

Sensing Mechanism and Material Behavior

The gas sensing behavior of ZnO thin films is primarily governed by surface adsorption and charge transfer processes typical of n-type metal oxide semiconductors. In ambient air, oxygen molecules are adsorbed onto the ZnO surface, capturing electrons from the conduction band and forming negatively charged oxygen species. This process creates an electron depletion layer near the surface, increasing the potential barrier at grain boundaries and reducing the overall conductivity of the material. Upon exposure to a reducing gas such as hydrogen, the adsorbed oxygen species react with the gas molecules, releasing trapped electrons back into the conduction band as shown in equations (12 and 13) [144]. This reduces the depletion region and lowers the barrier height, resulting in a measurable increase in conductivity (or decrease in resistance).

$$O_{2(g)} + e^- \rightarrow O_2{}^-(ads) \quad \text{at ambient conditions} \tag{12}$$

$$2H_{2(g)} + O_2{}^-(ads) \rightarrow 2H_2O_{(g)} + e^- \quad \text{at ambient conditions} \tag{13}$$

The sensing performance is closely linked to the structural properties of the ZnO thin films, particularly particle size, defect density, and porosity. Reduction in particle size through milling increases the surface-to-volume ratio, thereby enhancing the number of active adsorption sites and improving sensitivity. However, excessive milling can introduce a high density of bulk defects and promote particle agglomeration, which reduces effective surface area and limits gas diffusion. Additionally, surface defects act as active sites for gas adsorption and charge trapping, while bulk defects may facilitate recombination processes that diminish sensor performance. Therefore, the observed sensing behavior reflects a balance between increased surface activity and the effects of excessive structural disorder.

4.3 Chapter Summary

This chapter presents an investigation of the structural, morphological, optical, and gas sensing properties of ZnO thin films fabricated from mechanochemically fabricated nanoinks. The results demonstrate that PBM is an effective and scalable approach for tuning nanoparticle characteristics and, consequently, sensor performance. Material characterization confirmed the successful formation of ZnO nanostructures with preserved wurtzite crystal structure and high purity. Techniques such as SEM, TEM, and AFM revealed that milling parameters and solvent choice strongly influence particle size, dispersion, and film morphology. Higher milling speeds produced smaller particles and more porous, interconnected networks, while lower speeds resulted in denser and more compact films. These morphological differences play a critical role in gas sensing by affecting surface area, gas diffusion pathways, and electrical continuity. Raman spectroscopy and EDX analysis further confirmed structural integrity and compositional purity, while also indicating increased defect density (e.g., oxygen vacancies) with higher milling energy. These defects act as active sites for gas adsorption and contribute significantly to sensing performance. Optical characterization showed a bandgap of approximately 3.26 eV, validating the suitability of the nanoinks for optoelectronic and sensing applications. Preliminary gas sensing measurements demonstrated that the fabricated ZnO thin film sensors exhibit reproducible responses to varying gas concentrations under both static and continuous flow conditions as a proof of concept. Sensor response increased with gas concentration, with measurable signals even at low concentrations, indicating promising detection capabilities. The sensing mechanism was governed by surface adsorption–desorption processes involving oxygen species, which modulate charge carrier concentration and electrical conductivity. Additionally, the influence of external factors such as light illumination was examined. Optical activation enhanced electrical conductivity and improved response and recovery times by promoting charge carrier generation and accelerating surface reactions, enabling effective sensing at or near room temperature. This chapter establishes a correlation between processing parameters, nanostructure properties, and gas sensing performance. The findings highlight that an optimal balance between particle size, defect density, and film morphology is essential for achieving high sensitivity, fast response, and reliable operation. These results validate the potential of PBM-derived ZnO nanoinks as a low-cost, scalable platform for flexible and environmentally friendly gas sensing applications.

Chapter 5

5. Conclusions and Future Work

5.1 Summary and Conclusion

This work has demonstrated the successful development and application of planetary ball milling (PBM)-derived ZnO nanoinks for the fabrication of low-cost, solution-processed thin-film gas sensors. The study establishes a low input energy, scalable and environmentally friendly approach to producing functional nanomaterials and depositing them onto a wide range of substrates using a simple adjustable blade-coating technique. By integrating material fabrication, thin-film deposition, and sensor characterization, this research provides a good understanding of how processing parameters influence structural, morphological, and sensing properties. A key outcome of this work is the validation of PBM as an effective and versatile method for producing ZnO nanostructures suitable for room temperature sensing applications. Through controlled variation of milling parameters including milling speed, duration, solvent medium, and ball-to-powder ratio it was shown that the physical characteristics of ZnO nanoparticles can be tuned. These parameters directly influence particle size, degree of agglomeration, and defect density, all of which play a critical role in determining the performance of the resulting gas sensors. For instance, increased milling duration and higher rotational speeds were generally associated with reduced particle size and improved dispersion, leading to enhanced surface area.

The fabricated ZnO nanoinks exhibited good compatibility with solution-based deposition technique, enabling the formation of uniform thin films with thicknesses in the range of approximately 20–50 µm. The adjustable blade applicator method proved to be a simple yet effective approach for controlling film thickness and achieving reproducible coatings across various substrates. Importantly, the ability to deposit ZnO films on both rigid and flexible substrates highlights the adaptability of this fabrication method and its potential for low-cost, large-area sensor production. A wide variety of substrates including glass slides, silicon wafers, anodized alumina, foil, filter paper, plain paper, lined paper, cardboard, sticky notes, ceramic and polymer transparencies were explored in this study. Rigid substrates such as glass and wafers provided smooth, stable platforms for fundamental material characterization and reproducible sensing behavior. In contrast, porous and flexible substrates like paper and cardboard demonstrated the feasibility of disposable, low-cost sensing platforms. This diversity of substrates underscores the versatility of ZnO nanoinks and opens new opportunities for application-specific sensor design.

Material characterization techniques including SEM, TEM, AFM, Raman spectroscopy, UV–Vis spectroscopy, and EDX provided detailed insights into the structural, morphological, optical, and

compositional properties of the fabricated films. TEM analysis confirmed polyhedral nanoscale particle (sizes typically ~100 nm) and revealed well-defined crystalline structures with lattice spacings consistent with the wurtzite phase of ZnO. SEM imaging showed the morphology of films (sub-micron sizes), interconnected nanoparticle networks and porous morphologies, which are advantageous for gas sensing due to increased surface area. Raman spectroscopy further verified the crystalline quality and phase purity of ZnO, with characteristic vibrational modes confirming the presence of the wurtzite structure. UV–Vis analysis demonstrated strong UV absorption and bandgap values of ~3.26 eV, consistent with ZnO's semiconducting properties. EDX results confirmed the elemental composition and purity of the films.

Preliminary gas sensing performance of the fabricated ZnO thin films was evaluated under controlled conditions as proof of concept. The sensors exhibited measurable and reproducible responses to various test gases, including hydrogen and other relevant (Ar) gas, under different concentrations and environmental conditions. The data showed that the ZnO thin-film sensors exhibit response times on the order of several minutes, with values ranging from approximately 610 s to 750 s for samples milled at lower speeds (200 rpm) under static flow conditions, and up to ~2100 s for the higher-energy milled sample (750 rpm, 90 min) under continuous flow. Recovery times were generally faster with less variations, falling within ~560 s to ~660 s for most samples, with a slightly longer recovery (~760 s) observed for the high-speed milled sample. Glass-based films (e.g., 50 µm and 20 µm at 200 rpm) demonstrate relatively faster response and recovery compared to paper-based substrates, which show slower kinetics. The sensing mechanism can primarily be attributed to the adsorption and desorption of oxygen species on the ZnO surface, leading to the formation of electron depletion layers. Upon exposure to reducing gases, reactions with adsorbed oxygen species release electrons back into the conduction band, resulting in a measurable change in electrical resistance. The results demonstrate that sensor performance is dependent on nanostructure properties and fabrication conditions. Film thickness likely played a critical role, as excessively thick films can hinder gas diffusion, while very thin films may lack sufficient conductive pathways. Additionally, substrate choice influenced both electrical behavior and mechanical stability, further emphasizing the importance of optimizing the entire fabrication system. A significant achievement of this work is the demonstration of room-temperature gas sensing, which represents a major advantage over conventional metal oxide sensors that typically require elevated operating temperatures. This not only reduces power consumption but also enhances safety and enables integration into flexible and wearable platforms making them disposable. The use of simple electrode configurations, including pencil-drawn, silver-pen drawn interdigitated electrodes and conductive paints, further contributes to the low-cost and accessible nature of the sensor design.

Overall, this research validates PBM ZnO nanoink-based thin films as a room temperature process and a promising platform for next-generation gas sensors. The combination of low-cost materials, scalable fabrication techniques, low input energy and tunable performance characteristics positions this approach as a viable solution for applications in environmental monitoring, industrial safety, and IoT-based sensing systems.

5.2 Future Work

While this study has demonstrated the feasibility and effectiveness of PBM-derived ZnO nanoinks for gas sensing applications, several avenues remain for further research and development to enhance performance, expand functionality, and enable practical deployment.

Improving and enhancing the current sensor results

Future work will focus on conducting more detailed and extended gas sensing studies to fully evaluate sensor performance under practical conditions. This will include testing against specific workplace-relevant gases such as ammonia (NH_3), hydrogen sulfide (H_2S), nitrogen dioxide (NO_2), carbon monoxide (CO), and volatile organic compounds (e.g. benzene, xylene, formaldehyde), with controlled variation of gas concentrations to establish calibration curves and determine key performance metrics such as the limit of detection (LOD) and sensitivity. Although pure ZnO gas sensors exhibit promising characteristics, they are often constrained by limitations such as low sensitivity, limited selectivity, and relatively high operating temperatures. To overcome these drawbacks, the introduction of dopants and the development of composite materials have proven to be effective approaches for improving sensing performance. Doping introduces additional active sites on the ZnO surface, enabling stronger and more selective adsorption of target gas molecules. This enhances surface reactions that directly influence the electrical conductivity of the material. In particular, noble metals such as Pd, Pt, Au, and Ag serve as catalytic agents that promote gas dissociation and accelerate charge transfer, thereby improving sensitivity, selectivity, and response speed. Additionally, rare-earth oxides (e.g., CeO_2, Y_2O_3) and transition metal oxides (e.g., TiO_2, SnO_2, In_2O_3) have been widely investigated for their ability to modify the electronic structure and provide stable, cost-effective doping alternatives [145]. In addition to elemental doping, combining ZnO with other materials to form composites offers further enhancements through synergistic effects. Incorporating materials such as graphene, carbon nanotubes, conductive polymers, or other semiconducting oxides can improve electrical conductivity, increase surface area, and facilitate more efficient gas adsorption and desorption processes [146]. The formation of heterojunctions, homojunctions, or Schottky junctions within these composite systems reduces potential barriers at grain boundaries and enhances electron transport across the sensing layer. As a result, these hybrid structures can achieve improved sensing performance, including higher sensitivity, faster dynamics, and the potential for lower-temperature operation. While this work focuses on pure ZnO thin films, these findings highlight the importance of exploring doped and composite systems in future studies to further advance gas sensor capabilities.

An important aspect that remains also to be investigated is the selectivity of the ZnO-based gas sensors toward specific target gases. While the current study demonstrates good sensitivity and reproducible response characteristics, the ability of the sensor to distinguish between different gases (e.g., hydrogen, carbon monoxide, nitrogen dioxide, and volatile organic compounds) is

critical for practical applications. Future work should focus on performing controlled exposure experiments using multiple gases at varying concentrations under identical operating conditions. Quantitative comparison of sensor response, response/recovery times, and baseline stability for each gas will enable the identification of selective sensing behavior. Additionally, evaluating cross-sensitivity effects in mixed-gas environments will provide insight into real-world performance, where multiple interfering species are often present. To further enhance selectivity, future studies should explore material modification strategies such as doping and composite formation. Incorporating catalytic noble metals (e.g., Pd, Pt, Au) or forming heterostructures with other metal oxides and carbon-based materials can tailor the surface chemistry and preferential adsorption of specific gas molecules. These modifications can introduce selective reaction pathways, alter activation energies, and improve discrimination between gases. Moreover, integrating light activation or temperature modulation techniques may provide an additional degree of selectivity by selectively enhancing reactions for certain gases. Overall, a combination of gas testing and material engineering will be essential to optimize selectivity and advance the ZnO sensor toward practical deployment.

ZnO-cellulose paper nanocomposite thin film sensor

A promising direction for future work involves the development of ZnO–cellulose paper nanocomposites for low-cost and flexible sensing platforms. Cellulose paper, being abundant, biodegradable, lightweight, and highly porous, provides an excellent scaffold for incorporating ZnO nanostructures through green fabrication like PBM. As illustrated in (figure 5.1), initial and preliminary ZnO-cellulose paper nanocomposite thin deposition trials were carried out after nano-grinding PBM fabrication. The intrinsic porosity and fibrous network of cellulose facilitate uniform dispersion of ZnO nanoparticles while significantly increasing the effective surface area available for gas adsorption or photoactive interactions. This composite structure is expected to enhance sensor sensitivity and response dynamics by improving gas diffusion pathways and promoting stronger interaction between analyte molecules and the ZnO surface. Additionally, the mechanical flexibility of paper substrates enables the fabrication of bendable and wearable sensing devices, aligning well with emerging applications in portable and IoT-based systems. Future studies should focus on optimizing the loading concentration of ZnO within the cellulose matrix, improving adhesion and film stability, and evaluating the electrical and sensing performance under varying environmental conditions such as humidity and temperature. Furthermore, surface functionalization or chemical modification of cellulose fibres may be explored to enhance compatibility with ZnO and tailor the composite properties for specific gas sensing or photodetection applications.

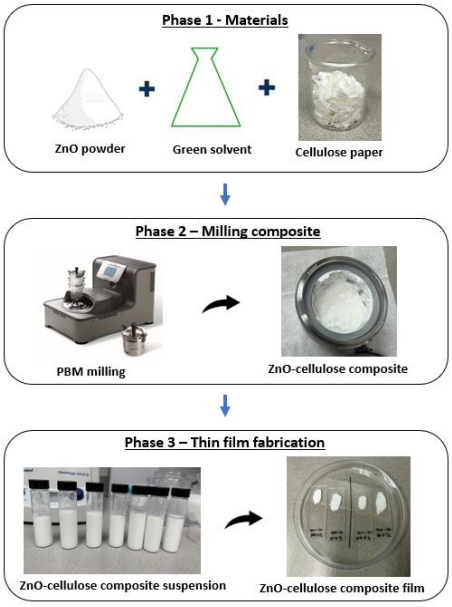

Figure 5.1: Schematic diagram showing the different phases followed during the ZnO-cellulose paper nanocomposite thin fabrication research work. Phase 1: Starting materials used (Bulk ZnO powder, solvent (e.g. DI water) and cellulose filter paper cut to 3 mm size); Phase 2: Fine colloidal suspension milling process; Phase 3: Thin film fabrication on glass slides by uniform coating of ZnO-cellulose paper nanocomposite thin film using suspension.

Computational simulation

Computational simulation is an essential tool for understanding and predicting the properties of nanomaterials, complementing experimental studies and enabling more efficient material design. In the context of ZnO-based thin films and gas sensors, computational modelling provides valuable insight into structural, electronic, and surface phenomena that are often challenging to probe directly. The work presented in this work can be further expanded through first-principles calculations based on density functional theory (DFT), which is widely recognized for its ability to accurately predict ground-state properties of materials. DFT is particularly advantageous due to its relatively low computational cost and its capability to model electronic structure, bandgap behavior, and defect states of ZnO with high reliability. In this study, preliminary simulations were carried out using the Materials Studio environment, employing on-the-fly generated ultrasoft pseudopotentials to describe electron–ion interactions. The optimized bulk ZnO structure obtained gave lattice parameters of a = 3.249 Å and c = 5.205 Å, with a c/a ratio of 1.602 and an internal parameter (u) of 0.3798. These values are in strong agreement with experimentally reported data, confirming the validity and accuracy of the computational approach. Beyond bulk properties, surface-level simulations can be performed to investigate the adsorption behavior of oxygen atoms on different sites of the Zn-terminated (001) surface of the wurtzite ZnO structure. Such studies are particularly important for gas sensing applications, as surface interactions govern

the adsorption and reaction of gas molecules, which in turn influence changes in electrical conductivity. By analyzing adsorption energies, charge transfer, and preferred binding configurations, these simulations provide a deeper understanding of the sensing mechanism at the atomic level. Further computational work can significantly expand on these findings by exploring a broader range of gas molecules, such as hydrogen sulfide, carbon monoxide, and volatile organic compounds, to evaluate their interaction with ZnO surfaces. Additionally, the effects of defects, doping with noble metals (e.g., Pd, Pt, Au), and the formation of composite materials can be studied to predict enhancements in sensitivity and selectivity. Coupling computational results with experimental data will enable a better understanding of structure–property relationships and accelerate the development of optimized ZnO-based sensing devices. Overall, computational simulation serves as a powerful predictive and interpretive tool, bridging the gap between theory and experiment in the advancement of nanomaterial-based technologies.

Device Fabrication Improvements

Further optimization of device fabrication is essential for improving sensor performance and reliability. Future work should focus on refining thin-film deposition techniques to achieve better uniformity, controlled thickness, and improved adhesion. Advanced methods such as spin coating, inkjet printing, or spray coating [147] could be explored as alternatives or complements to blade coating. Integration with microfabricated electrodes represents another important step toward practical device implementation. The use of lithographically defined interdigitated electrodes can provide improved electrical contact, reduced noise, and enhanced reproducibility. Additionally, encapsulation strategies and packaging solutions should be developed to protect the sensors from environmental degradation and ensure long-term stability. Future studies on ASTM D3359 adhesion tape test should investigate other substrates, different PBM processed nanoinks, nanocomposites, substrate surface treatments to improve adhesion of film and different film curing and annealing conditions.

Effects of temperature and humidity on sensor electrical characteristics

In addition to structural factors, the sensing response of ZnO thin films is influenced by external conditions such as temperature and humidity. Although this study primarily focuses on room-temperature operation, it is well understood that temperature and humidity affect both surface reaction kinetics and gas diffusion processes. At lower temperatures, adsorption dominates but proceeds slowly, while at elevated temperatures, enhanced reaction rates and ionized oxygen species improve sensor response [148]. Furthermore, environmental factors such as humidity can significantly alter sensor behavior. Water molecules adsorbed on the ZnO surface can either donate electrons or displace oxygen species, thereby modifying the charge carrier concentration and affecting the overall conductivity. These interactions highlight the importance of considering

real operating conditions when evaluating sensor performance. Humidity, in particular, plays a critical role in modulating the sensing mechanism and can introduce both beneficial and detrimental effects depending on its level [149]. At moderate relative humidity, adsorbed water molecules can enhance conductivity by releasing electrons into the conduction band or by forming hydroxyl groups that facilitate surface reactions with target gases. However, at higher humidity levels, excessive water adsorption can lead to the formation of a physisorbed water layer, which blocks active sensing sites and hinders gas diffusion to the ZnO surface. This results in reduced sensitivity, slower response times, and potential signal instability. Additionally, competitive adsorption between water molecules and target gas species can further suppress sensor response. Therefore, controlling or compensating for humidity effects is essential for achieving reliable and reproducible sensor performance, particularly for practical applications in ambient environments.

Additional Improvements

Future work should also explore advanced techniques for improving gas sensing set-up for better sensor performance and optimized functionality. Optical activation methods, such as UV illumination, enhance gas sensing at room temperature by generating additional charge carriers and promoting surface reactions and our current measuring set-up utilizes a quartz chamber which although is somewhat transparent, seems to attenuate some amount of the incident light on the sensor. By seeking others set-up designs and gas sensing strategies compactible with light-induced photon activation of the sensor which further decrease response times and improve sensitivity. Improvements in the gas testing system to includes better control of environmental parameters such as humidity, temperature, and gas flow rates are also necessary to achieve more accurate and reproducible measurements. The development of automated and integrated testing platforms would facilitate large-scale sensor evaluation and data collection.

5.3 Potential Applications

ZnO nanoink-based sensors have strong potential for real-world deployment across environmental monitoring, industrial safety, and public health sectors. In practical settings, these sensors can be used for continuous air quality monitoring in urban areas, detecting pollutants such as NO_2, CO, and volatile organic compounds (VOCs) in real time. In industrial environments, they can be integrated into safety systems to detect hazardous gas leaks, helping to prevent accidents in factories, chemical plants, and mining operations. Their low-cost and scalable fabrication also make them suitable for distributed sensing networks, where multiple sensors can be deployed over large areas to provide better environmental data. In healthcare and consumer applications, these ZnO nanoink sensors can be incorporated into wearable devices for breath analysis, enabling non-invasive monitoring of biomarkers related to respiratory conditions or

metabolic disorders. They also have promising applications in smart packaging, where they can detect spoilage gases and indicate food freshness, improving food safety and reducing waste. Additionally, their compatibility with flexible substrates allows integration into portable electronics and IoT-enabled systems for real-time data collection and wireless transmission. These real-world applications highlight the versatility of the ZnO nanoink-based sensors and their potential to transition from laboratory research to commercially viable technologies.

Photodetection

Another promising direction for potential application is the exploration of mechanochemically fabricated ZnO thin films for photodetection applications. Due to its wide bandgap and strong UV absorption, ZnO is inherently suitable for ultraviolet photodetectors. In this research, preliminary measurement of photodetection was carried out on ZnO thin film sensor (EG 200-10 on glass slide). As shown in (figure 5.2 (a) and (b)), Current-voltage curves for ZnO thin film sensor printed on paper upon exposure to different wavelengths light and photocurrent versus time response of ZnO thin film under ON/OFF pulse. As shown in (figure 5b), a sharp increase in photocurrent is observed upon illumination (ON), followed by a decay when the light is switched off (OFF), demonstrating the photoresponse and recovery behavior of the ZnO film. The current–voltage (I–V) characteristics shown in (a) demonstrate the significant influence of optical illumination on the electrical behavior of the sensor. Three conditions are compared: dark (no illumination), exposure to 400 nm light, and exposure to 650 nm light. The results highlight how light of different wavelengths modulates the conductivity of the sensing material.

Under dark conditions, the sensor exhibits very low current across the entire voltage range, indicating high resistance. This behavior is typical of semiconducting metal oxides such as ZnO, where charge carriers are limited due to the presence of surface-adsorbed oxygen species that trap free electrons. As a result, the conduction is suppressed, and the I–V curve remains nearly flat with minimal slope. When the sensor is illuminated with 400 nm light, a dramatic increase in current is observed, along with a much steeper and more linear I–V response. This wavelength lies in the near-ultraviolet region and has sufficient photon energy to excite electrons from the valence band to the conduction band of ZnO. The generation of electron–hole pairs significantly increase the carrier concentration, thereby enhancing electrical conductivity. Additionally, photogenerated holes migrate to the surface and facilitate the desorption of adsorbed oxygen species by neutralizing the negatively charged oxygen ions. This process releases trapped electrons back into the conduction band, further amplifying the current. The combined effect of photogeneration and oxygen desorption leads to a pronounced photoresponse, as evidenced by the large current values reaching over 20 nA at about 2.5 volts. In contrast, illumination with 650 nm light produces only a slight increase in current compared to the dark condition. This wavelength falls within the visible red region and has lower photon energy, which is insufficient to efficiently excite electrons across the wide bandgap of ZnO. As a result, the generation of electron–hole pairs are limited, and the impact on conductivity is minimal. The small increase in

current observed may be attributed to sub-bandgap absorption mechanisms, such as defect states or surface-related energy levels, which can weakly interact with lower-energy photons. This is further supported by the inset graph, where the response under 650 nm illumination shows only a modest deviation from the dark condition. The linearity of the I–V curves under illumination also provides insight into the contact behavior of the device. The symmetric and linear characteristics, particularly under 400 nm light, suggest ohmic contacts between the electrodes and the ZnO sensing material. This ensures that the observed changes in current are primarily due to intrinsic material properties rather than contact resistance effects. These results demonstrate that the ZnO sensor exhibits strong wavelength-dependent photoresponse, with significantly higher sensitivity under shorter wavelength (higher energy). The enhanced conductivity under UV illumination can be leveraged to improve gas sensing performance, as increased carrier density and surface activity facilitate faster and more pronounced reactions with target gas molecules. Conversely, the weak response under longer wavelengths highlights the importance of matching the light source to the material's bandgap for optimal performance. Future studies should investigate the photoresponse of ZnO thin films under other illumination conditions, including different wavelengths, light intensities, and modulation frequencies. Key performance metrics such as photocurrent generation, response time, recovery time, and sensitivity should be analyzed. The influence of material properties including particle size, defect density, and film morphology on photodetection performance should also be examined. Additionally, the role of substrates in light interaction and charge transport presents an interesting area of study, particularly for flexible and transparent devices.

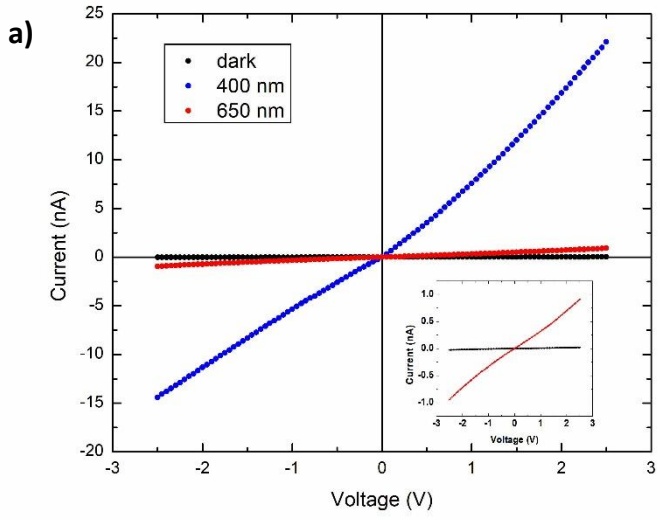

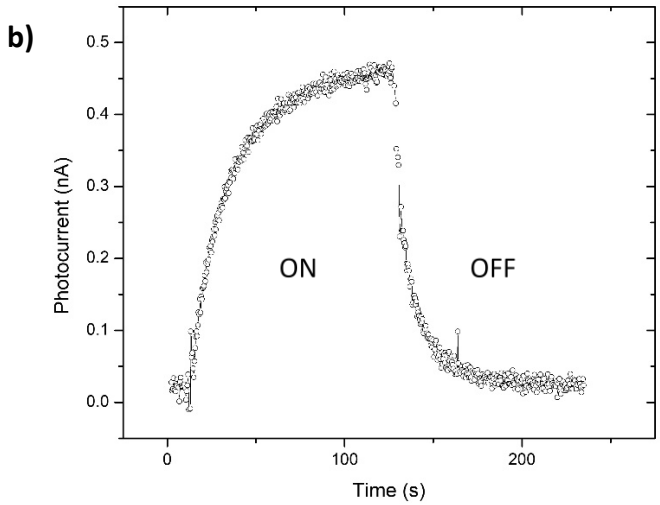

Figure 5.2: (a) Current-voltage curves for ZnO thin film sensor printed on paper upon exposure to different wavelength light. (b) Transient photocurrent response of the ZnO thin film under ON/OFF illumination.

Appendix-A

Sample (ZnO thin film)	Gas flow system	Response	Response time (T_{90})	Recovery Time (T_{10})
EG (200 – 10) at 50 µm, film on glass slide	Continuous flow: air-hydrogen-air (10 mins)	0.77	730 s	310 s
	Continuous flow air-hydrogen-air (45 mins)	0.93	1900 s	500 s
EG (750 – 90) at 20 µm, film on paper substrate	Continuous flow air-hydrogen-air (45 mins)	0.81	2100 s	760 s
EG (200 – 10) at 20 µm, film on glass slide	Continuous flow air-hydrogen-air (45 mins)	0.86	2050 s	280 s
EG (200 – 10) at 20 µm, film on paper substrate	Continuous flow air-hydrogen-air (45 mins)	0.72	2600 s	580 s
EG (200 – 10) at 20 µm, film on glass slide	H_2 (50 sccm)	0.110	640 s	560 s
	H_2 (100 sccm)	0.121	590 s	410 s
Continuous flow (co-flow; hydrogen-air)	H_2 (200 sccm)	0.128	520 s	355 s
EG (200 – 10) at 20 µm, film on paper	H_2 (50 sccm)	0.07	725 s	620 s
	H_2 (100 sccm)	0.82	700 s	590 s
Continuous flow (co-flow; hydrogen-air)	H_2 (200 sccm)	0.95	595 s	480 s
EG (200 – 10) at 20 µm, film on glass slide	H_2 (50 sccm)	0.066	680 s	590 s
	H_2 (100 sccm)	0.063	670 s	585 s
Static flow system (trapped test gas)	H_2 (200 sccm)	0.051	610 s	560 s
EG (200 – 10) at 20 µm, film on paper	H_2 (50 sccm)	0.045	750 s	660 s
	H_2 (100 sccm)	0.036	670 s	620 s
Static flow system (trapped test gas)	H_2 (200 sccm)	0.032	655 s	570 s

Table A.1: Sensitivity, response time and recovery time of the fabricated different ZnO sensor samples.

Sample labels definition

Sample labels are defined as follows: “EG 750-90” corresponds to ethylene glycol (EG) as the solvent, a milling speed of 750 rpm, and a milling duration of 90 minutes.

Sample labels are defined as follows: “EG 400-10” corresponds to ethylene glycol (EG) as the solvent, a milling speed of 400 rpm, and a milling duration of 10 minutes.

Sample labels are defined as follows: “IPA 200-10” corresponds to isopropyl alcohol (IPA) as the solvent, a milling speed of 200 rpm, and a milling duration of 10 minutes.

Sample labels are defined as follows: “DI 200-10” corresponds to DI water (DI) as the solvent, a milling speed of 200 rpm, and a milling duration of 10 minutes.

Sample labels are defined as follows: “DI 600-10” corresponds to DI water (DI) as the solvent, a milling speed of 600 rpm, and a milling duration of 10 minutes.

References

[1] L. Pokrajac *et al.*, "Nanotechnology for a Sustainable Future: Addressing Global Challenges with the International Network4Sustainable Nanotechnology," *ACS Nano,* vol. 15, no. 12, pp. 18608-18623, 2021/12/28 2021, doi: 10.1021/acsnano.1c10919.

[2] S. Bayda, M. Adeel, T. Tuccinardi, M. Cordani, and F. Rizzolio, "The History of Nanoscience and Nanotechnology: From Chemical–Physical Applications to Nanomedicine," *Molecules*, vol. 25, no. 1*,* p. 112doi: 10.3390/molecules25010112.

[3] R. Boyle, *The Sceptical Chymist; Or, Chymico-physical Doubts & Paradoxes: Touching the Spagyrist's Principles Commonly Call'd Hypostatical, as They are Wont to be Propos'd and Defended by the Generality of Alchymists. Whereunto is Præmis'd Part of Another Discourse Relating to the Same Subject*. Dawson of Pall Mall, 2007.

[4] M. Faraday, "X. The Bakerian Lecture.—Experimental relations of gold (and other metals) to light," *Philosophical transactions of the Royal Society of London,* no. 147, pp. 145-181, 1857.

[5] R. P. Feynman, "There's plenty of room at the bottom [data storage]," *Journal of microelectromechanical systems,* vol. 1, no. 1, pp. 60-66, 1992.

[6] C. P. Poole Jr, "Frank J. Owens, introduction to nanotechnology," ed: John Wiley & Sons, Inc., Hoboken, New Jersey, 2003.

[7] W. F. Brinkman, D. E. Haggan, and W. W. Troutman, "A history of the invention of the transistor and where it will lead us," *IEEE journal of solid-state circuits,* vol. 32, no. 12, pp. 1858-1865, 2002.

[8] "IBM Research. “Introducing the World’s First 2 nm Node Chip.” IBM Research Blog. https://research.ibm.com/blog/2-nm-chip," ed, 2021.

[9] "Intel Corporation, 14 nm Process Technology: Opening New Horizons. Intel Developer Forum (IDF). https://www.intel.com/content/dam/www/public/us/en/documents/technology-briefs/bohr-14nm-idf-2014-brief.pdf," ed, 2014.

[10] "Samsung Electronics. (n.d.). GAA structure transistors: A next-generation process for next-generation semiconductors. Samsung Semiconductor. https://semiconductor.samsung.com/support/tools-resources/dictionary/gaa-transistors-a-next-generation-process-for-next-generation-semiconductors/," ed.

[11] "Precedence Research Nanotechnology Market Size, Share and Trends (2025 to 2034) https://www.precedenceresearch.com/nanotechnology-market," ed, 2025.

[12] A. Bedoya-Pinto, K. Chang, M. G. Samant, and S. Sp Parkin, "Material Preparation and Thin Film Growth," in *Handbook of Magnetism and Magnetic Materials*: Springer, 2021, pp. 1153-1202.

[13] S. Parakatawella, A. P. G. M. V. Samaraweera, and T. M. Gunathilaka, "Vapor-Phase Production of Nanomaterials," in *Industrial Scale Production of Nanoparticles*, N. M. Adassooriya, A. Manipura, and A. Husen Eds. Singapore: Springer Nature Singapore, 2025, pp. 87-113.

[14] J.-W. Jo, S.-H. Kang, J. S. Heo, Y.-H. Kim, and S. K. Park, "Flexible Metal Oxide Semiconductor Devices Made by Solution Methods," *Chemistry – A European Journal,* vol. 26, no. 42, pp. 9126-9156, 2020/07/27 2020, doi: https://doi.org/10.1002/chem.202000090.

[15] E. Kabir, V. Kumar, K.-H. Kim, A. C. K. Yip, and J. R. Sohn, "Environmental impacts of nanomaterials," *Journal of Environmental Management,* vol. 225, pp. 261-271, 2018/11/01/ 2018, doi: https://doi.org/10.1016/j.jenvman.2018.07.087.

[16] B. Zong, S. Wu, Y. Yang, Q. Li, T. Tao, and S. Mao, "Smart Gas Sensors: Recent Developments and Future Prospective," *Nano-Micro Letters,* vol. 17, no. 1, p. 54, 2024/11/04 2024, doi: 10.1007/s40820-024-01543-w.

[17] O. V. Kharissova, B. I. Kharisov, C. M. Oliva González, Y. P. Méndez, and I. López, "Greener synthesis of chemical compounds and materials," *Royal Society Open Science,* vol. 6, no. 11, p. 191378, 2019, doi: 10.1098/rsos.191378.

[18] R. Sapkota, P. Duan, T. Kumar, A. Venkataraman, and C. Papadopoulos, "Thin Film Gas Sensors Based on Planetary Ball-Milled Zinc Oxide Nanoinks: Effect of Milling Parameters on Sensing Performance," *Applied Sciences*, vol. 11, no. 20, p. 9676doi: 10.3390/app11209676.

[19] H. Lyu, B. Gao, F. He, C. Ding, J. Tang, and J. C. Crittenden, "Ball-Milled Carbon Nanomaterials for Energy and Environmental Applications," *ACS Sustainable Chemistry & Engineering,* vol. 5, no. 11, pp. 9568-9585, 2017/11/06 2017, doi: 10.1021/acssuschemeng.7b02170.

[20] A. P. Onivefu and O. Imarhiagbe, "Types of Air Pollutants," in *Air Pollutants in the Context of One Health			: Fundamentals, Sources, and Impacts*, S. C. Izah, M. C. Ogwu, and A. Shahsavani Eds. Cham: Springer Nature Switzerland, 2024, pp. 123-160.

[21] S. J. Pai, T. S. Carter, C. L. Heald, and J. H. Kroll, "Updated World Health Organization Air Quality Guidelines Highlight the Importance of Non-anthropogenic PM2.5," *Environmental Science & Technology Letters,* vol. 9, no. 6, pp. 501-506, 2022/06/14 2022, doi: 10.1021/acs.estlett.2c00203.

[22] "UNICEF 2024 Air pollution accounted for 8.1 million deaths globally in 2021, becoming the second leading risk factor for death, including for children under five years. https://www.unicef.ca/en/press-release/air-pollution-accounted-81-million-deaths-globally-2021-becoming-second-leading-risk," ed.

[23] S. Palagati and J. Reddy, "Synthesis by top-down and Bottom-Up," *Adv. Mater.: Prod. Char. Multidiscip. App,* vol. 201, 2024.

[24] B. K. Teo and X. H. Sun, "From Top-Down to Bottom-Up to Hybrid Nanotechnologies: Road to Nanodevices," *Journal of Cluster Science,* vol. 17, no. 4, pp. 529-540, 2006/12/01 2006, doi: 10.1007/s10876-006-0086-5.

[25] N. M. Noah, "Design and Synthesis of Nanostructured Materials for Sensor Applications," *Journal of Nanomaterials,* vol. 2020, no. 1, p. 8855321, 2020/01/01 2020, doi: https://doi.org/10.1155/2020/8855321.

[26] J. K. Patel, A. Patel, and D. Bhatia, "Introduction to Nanomaterials and Nanotechnology," in *Emerging Technologies for Nanoparticle Manufacturing*, J. K. Patel and Y. V. Pathak Eds. Cham: Springer International Publishing, 2021, pp. 3-23.

[27] Y.-F. Sun *et al.*, "Metal Oxide Nanostructures and Their Gas Sensing Properties: A Review," *Sensors*, vol. 12, no. 3, pp. 2610-2631doi: 10.3390/s120302610.

[28] H. D. Salaudeen, R. D. Akinniranye, M. I. Kolawole, and S. Yahaya, "Nanomaterials in electronics: Advancements and challenges in high-performance devices," *World Journal of Advanced Research and Reviews,* vol. 24, no. 1, pp. 830-845, 2024.

[29] M. S. Yaghmaee, B. Shokri, and M. R. Rahimipour, "Size Dependence Surface Activity of Metallic Nanoparticles," *Plasma Processes and Polymers,* vol. 6, no. S1, pp. S876-S882, 2009/06/01 2009, doi: https://doi.org/10.1002/ppap.200932203.

[30] M. Pozzi *et al.*, "Visualization of the High Surface-to-Volume Ratio of Nanomaterials and Its Consequences," *Journal of Chemical Education,* vol. 101, no. 8, pp. 3146-3155, 2024/08/13 2024, doi: 10.1021/acs.jchemed.4c00089.

[31] K. Takei *et al.*, "Quantum Confinement Effects in Nanoscale-Thickness InAs Membranes," *Nano Letters,* vol. 11, no. 11, pp. 5008-5012, 2011/11/09 2011, doi: 10.1021/nl2030322.

[32] P. M. Visakh and M. J. M. Morlanes, *Nanomaterials and nanocomposites: zero-to three-dimensional materials and their composites*. John Wiley & Sons, 2016.

[33] M. B. Kulkarni, N. H. Ayachit, and T. M. Aminabhavi, "Recent Advancements in Nanobiosensors: Current Trends, Challenges, Applications, and Future Scope," *Biosensors*, vol. 12, no. 10, p. 892doi: 10.3390/bios12100892.

[34] M. Di Ventra, *Electrical transport in nanoscale systems*. Cambridge University Press, 2008.

[35] L. H. Madkour, "Properties of Nanostructured Materials (NSMs) and Physicochemical Properties of (NPs)," in *Nanoelectronic Materials: Fundamentals and Applications*, L. H. Madkour Ed. Cham: Springer International Publishing, 2019, pp. 479-564.

[36] H. Li *et al.*, "Zinc Oxide as a Model Transparent Conducting Oxide: A Theoretical and Experimental Study of the Impact of Hydroxylation, Vacancies, Interstitials, and Extrinsic Doping on the Electronic Properties of the Polar ZnO (0002) Surface," *Chemistry of Materials,* vol. 24, no. 15, pp. 3044-3055, 2012/08/14 2012, doi: 10.1021/cm301596x.

[37] E. C. Dreaden, A. M. Alkilany, X. Huang, C. J. Murphy, and M. A. El-Sayed, "The golden age: gold nanoparticles for biomedicine," *Chemical Society Reviews,* 10.1039/C1CS15237H vol. 41, no. 7, pp. 2740-2779, 2012, doi: 10.1039/C1CS15237H.

[38] "Fraunhofer Nanotechnology FNT Introduction to nanotechnology. https://www.nano.fraunhofer.de/en/what-is-nanotechnology/introduction.html," ed, 2024.

[39] J. Hou, J. A. Lartey, C. Y. Lee, and J.-H. Kim, "Light-enhanced catalytic activity of stable and large gold nanoparticles in homocoupling reactions," *Scientific Reports,* vol. 14, no. 1, p. 1352, 2024/01/16 2024, doi: 10.1038/s41598-024-51695-3.

[40] C. Liang *et al.*, "Size-Dependent Catalytic Behavior of Gold Nanoparticles," *Advanced Materials Interfaces,* vol. 9, no. 4, p. 2100867, 2022/02/01 2022, doi: https://doi.org/10.1002/admi.202100867.

[41] S. T. Kim, K. Saha, C. Kim, and V. M. Rotello, "The Role of Surface Functionality in Determining Nanoparticle Cytotoxicity," *Accounts of Chemical Research,* vol. 46, no. 3, pp. 681-691, 2013/03/19 2013, doi: 10.1021/ar3000647.

[42] M.-A. Shahbazi *et al.*, "The mechanisms of surface chemistry effects of mesoporous silicon nanoparticles on immunotoxicity and biocompatibility," *Biomaterials,* vol. 34, no. 31, pp. 7776-7789, 2013/10/01/ 2013, doi: https://doi.org/10.1016/j.biomaterials.2013.06.052.

[43] A. H. Abdelmohsen, W. M. A. E. Rouby, N. Ismail, and A. A. Farghali, "Morphology Transition Engineering of ZnO Nanorods to Nanoplatelets Grafted Mo8O23-MoO2 by Polyoxometalates: Mechanism and Possible Applicability to other Oxides," *Scientific Reports,* vol. 7, no. 1, p. 5946, 2017/07/19 2017, doi: 10.1038/s41598-017-05750-x.

[44] W. Zhang, P. Wang, X. Fei, Y. Xiu, and G. Jia, "Growth Mechanism and Morphologies Tuning of ZnO Nanostructures," *International Journal of Electrochemical Science,* vol. 10, no. 6, pp. 4688-4695, 2015/06/01/ 2015, doi: https://doi.org/10.1016/S1452-3981(23)06656-7.

[45] A. N. Solodov, J. R. Shayimova, E. A. Burilova, and R. R. Amirov, "Polyethyleneimine-modified iron oxide nanoparticles: their synthesis and state in water and in solutions of ligands," *Colloid and Polymer Science,* vol. 296, no. 12, pp. 1983-1993, 2018/12/01 2018, doi: 10.1007/s00396-018-4425-5.

[46] A. Mittal, I. Roy, and S. Gandhi, "Magnetic Nanoparticles: An Overview for Biomedical Applications," *Magnetochemistry*, vol. 8, no. 9*,* p. 107doi: 10.3390/magnetochemistry8090107.

[47] L. Kafrouni and O. Savadogo, "Recent progress on magnetic nanoparticles for magnetic hyperthermia," *Progress in Biomaterials,* vol. 5, no. 3, pp. 147-160, 2016/12/01 2016, doi: 10.1007/s40204-016-0054-6.

[48] H.-J. Krause and U. M. Engelmann, "Fundamentals and Applications of Dual-Frequency Magnetic Particle Spectroscopy: Review for Biomedicine and Materials Characterization," *Advanced Science,* vol. 12, no. 13, p. 2416838, 2025/04/01 2025, doi: https://doi.org/10.1002/advs.202416838.

[49] G. T. Colombo *et al.*, "Magnetic Nanoparticles in Theranostics: From Controlled Synthesis and Surface Engineering to Biological Performance and Clinical Translation," *Journal of Nanotheranostics*, vol. 7, no. 1*,* p. 7doi: 10.3390/jnt7010007.

[50] K. S. Das *et al.*, "Recent Advances in Nanostructured Materials: Applications in Biosensors, Gas Sensors, and Chemical Sensors," *Electroanalysis,* vol. 37, no. 8, p. e70027, 2025/08/01 2025, doi: https://doi.org/10.1002/elan.70027.
[51] "Introduction: Nanoparticle Chemistry," *Chemical Reviews,* vol. 116, no. 18, pp. 10343-10345, 2016/09/28 2016, doi: 10.1021/acs.chemrev.6b00566.
[52] M. Saeed, H. M. Marwani, U. Shahzad, A. M. Asiri, and M. M. Rahman, "Recent Advances, Challenges, and Future Perspectives of ZnO Nanostructure Materials Towards Energy Applications," *The Chemical Record,* vol. 24, no. 1, p. e202300106, 2024/01/01 2024, doi: https://doi.org/10.1002/tcr.202300106.
[53] A. Rae, "Real life applications of nanotechnology in electronics," *OnBoard Technol,* vol. 2006, p. 28, 2006.
[54] S. Bhatia, "Nanotechnology and its drug delivery applications," in *Natural Polymer Drug Delivery Systems: Nanoparticles, Plants, and Algae*: Springer, 2016, pp. 1-32.
[55] M. N. F. Norrrahim *et al.*, "Nanocellulose: the next super versatile material for the military," *Materials Advances,* 10.1039/D0MA01011A vol. 2, no. 5, pp. 1485-1506, 2021, doi: 10.1039/D0MA01011A.
[56] S. H. Chae and Y. H. Lee, "Carbon nanotubes and graphene towards soft electronics," *Nano Convergence,* vol. 1, no. 1, p. 15, 2014/04/25 2014, doi: 10.1186/s40580-014-0015-5.
[57] N. Sharma, H. Ojha, A. Bharadwaj, D. P. Pathak, and R. K. Sharma, "Preparation and catalytic applications of nanomaterials: a review," *RSC Advances,* 10.1039/C5RA06778B vol. 5, no. 66, pp. 53381-53403, 2015, doi: 10.1039/C5RA06778B.
[58] R. Kabir, M. A. Saifullah, A. Z. Ahmed, S. M. Masum, and M. A. Molla, "Synthesis of N-Doped ZnO Nanocomposites for Sunlight Photocatalytic Degradation of Textile Dye Pollutants," *Journal of Composites Science*, vol. 4, no. 2, p. 49doi: 10.3390/jcs4020049.
[59] C. Santhosh, V. Velmurugan, G. Jacob, S. K. Jeong, A. N. Grace, and A. Bhatnagar, "Role of nanomaterials in water treatment applications: A review," *Chemical Engineering Journal,* vol. 306, pp. 1116-1137, 2016/12/15/ 2016, doi: https://doi.org/10.1016/j.cej.2016.08.053.
[60] Y. Tu, "Moore's Law," in *Insights into Semiconductor Technologies: Transistor, Interconnect, Packaging, Lithography and Memory*, Y. Tu Ed. Cham: Springer Nature Switzerland, 2026, pp. 1-16.
[61] "Taiwan Semiconductor Manufacturing Company (TSMC) Logic technology. https://www.tsmc.com/english/dedicatedFoundry/technology/logic," ed, 2026.
[62] S. Kumar and D. K. Aswal, "Recent Advances in Thin Films," 2020.
[63] L. O. Orzari *et al.*, "Screen-Printing vs Additive Manufacturing Approaches: Recent Aspects and Trends Involving the Fabrication of Electrochemical Sensors," *Analytical Chemistry,* vol. 97, no. 3, pp. 1482-1494, 2025/01/28 2025, doi: 10.1021/acs.analchem.4c05786.
[64] J. Zikulnig *et al.*, "Printed Electronics Technologies for Additive Manufacturing of Hybrid Electronic Sensor Systems," *Advanced Sensor Research,* vol. 2, no. 7, p. 2200073, 2023/07/01 2023, doi: https://doi.org/10.1002/adsr.202200073.
[65] G. Jung *et al.*, "Reconfigurable Manipulation of Oxygen Content on Metal Oxide Surfaces and Applications to Gas Sensing," *ACS Nano,* vol. 17, no. 18, pp. 17790-17798, 2023/09/26 2023, doi: 10.1021/acsnano.3c03034.
[66] N. Goel, K. Kunal, A. Kushwaha, and M. Kumar, "Metal oxide semiconductors for gas sensing," *Engineering Reports,* vol. 5, no. 6, p. e12604, 2023/06/01 2023, doi: https://doi.org/10.1002/eng2.12604.
[67] K. Ravichandran and A. Manivasaham, "Enhanced ammonia sensing by Sn doped ZnO films prepared by a low-cost fully automated nebulizer spray technique," *Journal of Materials Science: Materials in Electronics,* vol. 28, no. 8, pp. 6335-6344, 2017/04/01 2017, doi: 10.1007/s10854-016-6317-0.

[68] A. Kumar *et al.*, "Application of gas monitoring sensors in underground coal mines and hazardous areas," *International Journal of Computer Technology and Electronics Engineering,* vol. 3, no. 3, pp. 9-23, 2013.
[69] S. F. Sulthana *et al.*, "Investigations of Materials and Technologies Behind Environmental Pollution Monitoring Sensors for Global Health," *ACS Omega,* vol. 10, no. 27, pp. 28499-28514, 2025/07/15 2025, doi: 10.1021/acsomega.4c09790.
[70] R. Sapkota, P. Duan, T. Kumar, A. Venkataraman, and C. Papadopoulos, "Thin Film Gas Sensors Based on Planetary Ball-Milled Zinc Oxide Nanoinks: Effect of Milling Parameters on Sensing Performance," *Applied Sciences*, vol. 11, no. 20*,* doi: 10.3390/app11209676.
[71] S. Kanth, S. Choudhury, S. Kumar, R. Rao, A. K. Debnath, and C. A. Betty, "Reliable NO2 sensing and alert system based on Pd-PdO thin film with sub ppm level detection at room temperature," *Sensors and Actuators B: Chemical,* vol. 403, p. 135145, 2024/03/15/ 2024, doi: https://doi.org/10.1016/j.snb.2023.135145.
[72] M. Sung *et al.*, "Metal-Oxide-Decorated Mesoporous Silica Chemiresistors for Exhaled Biomarker Detection," *ACS Omega,* vol. 10, no. 15, pp. 15629-15636, 2025/04/22 2025, doi: 10.1021/acsomega.5c00912.
[73] B. Nabet, *Photodetectors: Materials, Devices and Applications*. Woodhead publishing, 2023.
[74] S. I. Inamdar and K. Y. Rajpure, "High-performance metal–semiconductor–metal UV photodetector based on spray deposited ZnO thin films," *Journal of Alloys and Compounds,* vol. 595, pp. 55-59, 2014/05/15/ 2014, doi: https://doi.org/10.1016/j.jallcom.2014.01.147.
[75] A. J. Gimenez, J. M. Yáñez-Limón, and J. M. Seminario, "ZnO−Paper Based Photoconductive UV Sensor," *The Journal of Physical Chemistry C,* vol. 115, no. 1, pp. 282-287, 2011/01/13 2011, doi: 10.1021/jp107812w.
[76] A. Rasool, M. C. Santhosh Kumar, M. H. Mamat, C. Gopalakrishnan, and R. Amiruddin, "Analysis on different detection mechanisms involved in ZnO-based photodetector and photodiodes," *Journal of Materials Science: Materials in Electronics,* vol. 31, no. 9, pp. 7100-7113, 2020/05/01 2020, doi: 10.1007/s10854-020-03280-3.
[77] R. Khokhra, B. Bharti, H.-N. Lee, and R. Kumar, "Visible and UV photo-detection in ZnO nanostructured thin films via simple tuning of solution method," *Scientific Reports,* vol. 7, no. 1, p. 15032, 2017/11/08 2017, doi: 10.1038/s41598-017-15125-x.
[78] W. Si *et al.*, "Recent Advances in Broadband Photodetectors from Infrared to Terahertz," *Micromachines*, vol. 15, no. 4*,* p. 427doi: 10.3390/mi15040427.
[79] A. B. U. Rahman *et al.*, "IR photodetector capabilities of p-NiO/n-ZnO heterojunction structure," *Materials Today: Proceedings,* vol. 92, pp. 775-778, 2023/01/01/ 2023, doi: https://doi.org/10.1016/j.matpr.2023.04.322.
[80] G. Boakye, A. Venkataraman, and C. Papadopoulos, "Low-cost sensors printed using mechanochemically synthesized nanoinks.," presented at the Institute of Electrical and Electronics Engineers Nanotechnology Materials and Devices Conference (IEEE-NMDC), 2025.
[81] G. A. Boakye, E. Trotta, N. Ambagahawatta, A. Venkataraman, N. Cheeptham, and C. Papadopoulos, "Nanoscale plastic pollution: sources, identification and potential mitigation," *Nanotechnology,* vol. 36, no. 42, p. 422001, 2025/10/15 2025, doi: 10.1088/1361-6528/ae0c1b.
[82] Z. L. Wang, "Nanostructures of zinc oxide," *Materials Today,* vol. 7, no. 6, pp. 26-33, 2004/06/01/ 2004, doi: https://doi.org/10.1016/S1369-7021(04)00286-X.
[83] P. Uthirakumar, H. G. Kim, and C.-H. Hong, "Zinc oxide nanostructures derived from a simple solution method for solar cells and LEDs," *Chemical Engineering Journal,* vol. 155, no. 3, pp. 910-915, 2009/12/15/ 2009, doi: https://doi.org/10.1016/j.cej.2009.09.025.
[84] Ü. Özgür *et al.*, "A comprehensive review of ZnO materials and devices," *Journal of Applied Physics,* vol. 98, no. 4, p. 041301, 2005, doi: 10.1063/1.1992666.

[85] Y. Han, J. Guo, Q. Luo, and C.-Q. Ma, "Solution-Processable Zinc Oxide for Printed Photovoltaics: Progress, Challenges, and Prospect," *Advanced Energy and Sustainability Research,* vol. 4, no. 10, p. 2200179, 2023/10/01 2023, doi: https://doi.org/10.1002/aesr.202200179.

[86] J. A. Röhr, J. Sá, and S. J. Konezny, "The role of adsorbates in the green emission and conductivity of zinc oxide," *Communications Chemistry,* vol. 2, no. 1, p. 52, 2019/05/02 2019, doi: 10.1038/s42004-019-0153-0.

[87] D. Vogel, P. Krüger, and J. Pollmann, "Self-interaction and relaxation-corrected pseudopotentials for II-VI semiconductors," *Physical Review B,* vol. 54, no. 8, pp. 5495-5511, 08/15/ 1996, doi: 10.1103/PhysRevB.54.5495.

[88] A. Janotti and C. G. Van de Walle, "Fundamentals of zinc oxide as a semiconductor," *Reports on Progress in Physics,* vol. 72, no. 12, p. 126501, 2009/10/22 2009, doi: 10.1088/0034-4885/72/12/126501.

[89] D. Mora-Fonz, T. Lazauskas, M. R. Farrow, C. R. A. Catlow, S. M. Woodley, and A. A. Sokol, "Why Are Polar Surfaces of ZnO Stable?," *Chemistry of Materials,* vol. 29, no. 12, pp. 5306-5320, 2017/06/27 2017, doi: 10.1021/acs.chemmater.7b01487.

[90] L. Xu *et al.*, "ZnO with Different Morphologies Synthesized by Solvothermal Methods for Enhanced Photocatalytic Activity," *Chemistry of Materials,* vol. 21, no. 13, pp. 2875-2885, 2009/07/14 2009, doi: 10.1021/cm900608d.

[91] S. Raha and M. Ahmaruzzaman, "ZnO nanostructured materials and their potential applications: progress, challenges and perspectives," *Nanoscale Advances,* 10.1039/D1NA00880C vol. 4, no. 8, pp. 1868-1925, 2022, doi: 10.1039/D1NA00880C.

[92] C. Zhu and X. Wang, "Nanomaterial ZnO Synthesis and Its Photocatalytic Applications: A Review," *Nanomaterials*, vol. 15, no. 9*,* p. 682doi: 10.3390/nano15090682.

[93] W. H. Hirschwald, "Zinc oxide: an outstanding example of a binary compound semiconductor," *Accounts of Chemical Research,* vol. 18, no. 8, pp. 228-234, 1985.

[94] P. Dasgupta and J. Mitra, "Comparative Evaluation of Functional Properties and Thermal Stability of Nanochitosan Synthesized Via Ionotropic Gelation and Ball Milling," *Food Biophysics,* vol. 20, no. 4, p. 159, 2025/10/21 2025, doi: 10.1007/s11483-025-10040-5.

[95] C. N. Corp., "Understanding planetary ball milling and its industrial applications. https://www.calnanocorp.com/nanotechnologies-news-corner/understanding-planetary-ball-milling-and-its-industrial-applications," ed, 2025.

[96] C. Burmeister, L. Titscher, S. Breitung-Faes, and A. Kwade, "Dry grinding in planetary ball mills: Evaluation of a stressing model," *Advanced Powder Technology,* vol. 29, no. 1, pp. 191-201, 2018/01/01/ 2018, doi: https://doi.org/10.1016/j.apt.2017.11.001.

[97] "Fritsch Milling and Sizing Inc. Planetary mills. https://fritsch-us.com/milling/planetary-mills/," ed, 2026.

[98] B. Doroszuk, P. Bortnowski, M. Ozdoba, and R. Król, "Scaling Energy Transfer in Ball Mills: A Scale-Agnostic Approach through a Universal Scaling Constant," *Energies*, vol. 17, no. 11*,* p. 2693doi: 10.3390/en17112693.

[99] S. B. Akçay *et al.*, "Effect of mechanical milling parameters on the properties of electrolytic pure copper powders and hot pressed billets fabricated from recycled copper wastes," *Materials Chemistry and Physics,* vol. 346, p. 131367, 2025/12/01/ 2025, doi: https://doi.org/10.1016/j.matchemphys.2025.131367.

[100] M. A. Butt, "Thin-Film Coating Methods: A Successful Marriage of High-Quality and Cost-Effectiveness—A Brief Exploration," *Coatings*, vol. 12, no. 8*,* p. 1115doi: 10.3390/coatings12081115.

[101] W. Li, H. Hao, M. He, J. Xing, H. Gao, and J. Dong, "ZnO:Al/Al back reflector with good adhesion on a flexible polyimide substrate for thin film silicon solar cells," *Surface and Coatings Technology,* vol. 258, pp. 991-995, 2014/11/15/ 2014, doi: https://doi.org/10.1016/j.surfcoat.2014.07.045.

[102] T. Sander, S. Eisermann, B. K. Meyer, and P. J. Klar, "Raman tensor elements of wurtzite ZnO," *Physical Review B,* vol. 85, no. 16, p. 165208, 04/23/ 2012, doi: 10.1103/PhysRevB.85.165208.

[103] M. Hansen, J. Truong, T. Xie, and J.-i. Hahm, "Spatially distinct Raman scattering characteristics of individual ZnO nanorods under controlled polarization: intense end scattering from forbidden modes," *Nanoscale,* 10.1039/C7NR02672B vol. 9, no. 24, pp. 8470-8480, 2017, doi: 10.1039/C7NR02672B.

[104] Z. Tan *et al.*, "Thinning ferroelectric films for high-efficiency photovoltaics based on the Schottky barrier effect," *NPG Asia Materials,* vol. 11, no. 1, p. 20, 2019/04/26 2019, doi: 10.1038/s41427-019-0120-3.

[105] X. B. Wang, C. Song, K. W. Geng, F. Zeng, and F. Pan, "Photoluminescence and Raman scattering of Cu-doped ZnO films prepared by magnetron sputtering," *Applied Surface Science,* vol. 253, no. 16, pp. 6905-6909, 2007/06/15/ 2007, doi: https://doi.org/10.1016/j.apsusc.2007.02.013.

[106] M. Yoshikawa, K. Inoue, T. Nakagawa, H. Ishida, N. Hasuike, and H. Harima, "Characterization of ZnO nanoparticles by resonant Raman scattering and cathodoluminescence spectroscopies," *Applied Physics Letters,* vol. 92, no. 11, p. 113115, 2008, doi: 10.1063/1.2901159.

[107] U. Kaiser *et al.*, "Transmission electron microscopy at 20kV for imaging and spectroscopy," *Ultramicroscopy,* vol. 111, no. 8, pp. 1239-1246, 2011/07/01/ 2011, doi: https://doi.org/10.1016/j.ultramic.2011.03.012.

[108] D. H. Anjum, "Characterization of nanomaterials with transmission electron microscopy," *IOP Conference Series: Materials Science and Engineering,* vol. 146, no. 1, p. 012001, 2016/08/01 2016, doi: 10.1088/1757-899X/146/1/012001.

[109] A. Bagabas, A. Alshammari, M. F. A. Aboud, and H. Kosslick, "Room-temperature synthesis of zinc oxide nanoparticles in different media and their application in cyanide photodegradation," *Nanoscale Research Letters,* vol. 8, no. 1, p. 516, 2013/12/06 2013, doi: 10.1186/1556-276X-8-516.

[110] B. K. Wilson and R. K. Prud'homme, "Nanoparticle size distribution quantification from transmission electron microscopy (TEM) of ruthenium tetroxide stained polymeric nanoparticles," *Journal of Colloid and Interface Science,* vol. 604, pp. 208-220, 2021/12/15/ 2021, doi: https://doi.org/10.1016/j.jcis.2021.04.081.

[111] A. Datye and A. DeLaRiva, "Scanning Electron Microscopy (SEM)," in *Springer Handbook of Advanced Catalyst Characterization*, I. E. Wachs and M. A. Bañares Eds. Cham: Springer International Publishing, 2023, pp. 359-380.

[112] B. Freeland, I. U. Ahad, G. Foley, and D. Brabazon, "Advanced Characterization Techniques for Nanostructures," in *Micro and Nanomanufacturing Volume II*, M. J. Jackson and W. Ahmed Eds. Cham: Springer Nature Switzerland, 2025, pp. 53-89.

[113] T. R. Ray, B. Lettiere, J. de Rutte, and S. Pennathur, "Quantitative Characterization of the Colloidal Stability of Metallic Nanoparticles Using UV–vis Absorbance Spectroscopy," *Langmuir,* vol. 31, no. 12, pp. 3577-3586, 2015/03/31 2015, doi: 10.1021/la504511j.

[114] S. Khan, M. Sadiq, N. Muhammad, A. Noor, S. Qayyum, and M. Farhan, "NiCd/ZnO nanocomposites: novel materials for photocatalytic degradation of Allura Red dye," *Scientific Reports,* vol. 16, no. 1, p. 5204, 2026/01/14 2026, doi: 10.1038/s41598-026-36010-6.

[115] P. Makuła, M. Pacia, and W. Macyk, "How To Correctly Determine the Band Gap Energy of Modified Semiconductor Photocatalysts Based on UV–Vis Spectra," *The Journal of Physical Chemistry Letters,* vol. 9, no. 23, pp. 6814-6817, 2018/12/06 2018, doi: 10.1021/acs.jpclett.8b02892.

[116] C. Barth, A. S. Foster, C. R. Henry, and A. L. Shluger, "Recent Trends in Surface Characterization and Chemistry with High-Resolution Scanning Force Methods," *Advanced Materials,* vol. 23, no. 4, pp. 477-501, 2011/01/25 2011, doi: https://doi.org/10.1002/adma.201002270.

[117] F. El Feninat, S. Elouatik, T. H. Ellis, E. Sacher, and I. Stangel, "Quantitative assessment of surface roughness as measured by AFM: application to polished human dentin," *Applied Surface Science,* vol. 183, no. 3, pp. 205-215, 2001/11/28/ 2001, doi: https://doi.org/10.1016/S0169-4332(01)00558-X.

[118] D. Hector, S. Olivero, F. Orange, E. Duñach, and J.-F. Gal, "Quality Control of a Functionalized Polymer Catalyst by Energy Dispersive X-ray Spectrometry (EDX or EDS)," *Analytical Chemistry,* vol. 91, no. 3, pp. 1773-1778, 2019/02/05 2019, doi: 10.1021/acs.analchem.8b04170.

[119] A. Sahai and N. Goswami, "Probing the dominance of interstitial oxygen defects in ZnO nanoparticles through structural and optical characterizations," *Ceramics International,* vol. 40, no. 9, Part B, pp. 14569-14578, 2014/11/01/ 2014, doi: https://doi.org/10.1016/j.ceramint.2014.06.041.

[120] H. Rai, Prashant, and N. Kondal, "A review on defect related emissions in undoped ZnO nanostructures," *Materials Today: Proceedings,* vol. 48, pp. 1320-1324, 2022/01/01/ 2022, doi: https://doi.org/10.1016/j.matpr.2021.08.343.

[121] S. Vyas, "A short review on properties and applications of zinc oxide based thin films and devices: ZnO as a promising material for applications in electronics, optoelectronics, biomedical and sensors," *Johnson Matthey Technology Review,* vol. 64, no. 2, pp. 202-218, 2020.

[122] H. Liu, V. Avrutin, N. Izyumskaya, Ü. Özgür, and H. Morkoç, "Transparent conducting oxides for electrode applications in light emitting and absorbing devices," *Superlattices and Microstructures,* vol. 48, no. 5, pp. 458-484, 2010/11/01/ 2010, doi: https://doi.org/10.1016/j.spmi.2010.08.011.

[123] B.-Z. Dong, G.-J. Fang, J.-F. Wang, W.-J. Guan, and X.-Z. Zhao, "Effect of thickness on structural, electrical, and optical properties of ZnO: Al films deposited by pulsed laser deposition," *Journal of Applied Physics,* vol. 101, no. 3, p. 033713, 2007, doi: 10.1063/1.2437572.

[124] P. Bhattacharyya, P. K. Basu, B. Mondal, and H. Saha, "A low power MEMS gas sensor based on nanocrystalline ZnO thin films for sensing methane," *Microelectronics Reliability,* vol. 48, no. 11, pp. 1772-1779, 2008/11/01/ 2008, doi: https://doi.org/10.1016/j.microrel.2008.07.063.

[125] T. Wu, Z. Wang, M. Tian, J. Miao, H. Zhang, and J. Sun, "UV excitation NO2 gas sensor sensitized by ZnO quantum dots at room temperature," *Sensors and Actuators B: Chemical,* vol. 259, pp. 526-531, 2018/04/15/ 2018, doi: https://doi.org/10.1016/j.snb.2017.12.101.

[126] X. Yang *et al.*, "One step synthesis of branched SnO2/ZnO heterostructures and their enhanced gas-sensing properties," *Sensors and Actuators B: Chemical,* vol. 281, pp. 415-423, 2019/02/15/ 2019, doi: https://doi.org/10.1016/j.snb.2018.10.138.

[127] A. Tabib *et al.*, "Structural and optical properties of Na doped ZnO nanocrystals: Application to solar photocatalysis," *Applied Surface Science,* vol. 396, pp. 1528-1538, 2017/02/28/ 2017, doi: https://doi.org/10.1016/j.apsusc.2016.11.204.

[128] A. Elbrolesy, Y. Abdou, F. A. Elhussiny, and R. Morsy, "Novel Green Synthesis of UV-Sunscreen ZnO Nanoparticles Using Solanum Lycopersicum Fruit Extract and Evaluation of Their Antibacterial and Anticancer Activity," *Journal of Inorganic and Organometallic Polymers and Materials,* vol. 33, no. 12, pp. 3750-3759, 2023/12/01 2023, doi: 10.1007/s10904-023-02744-3.

[129] R. Bharti, M. M. Butt, and A. Dey, "Advanced multilayer thin films for stealth applications: optical, electrical, and thermal enhancements—a comprehensive study," *Journal of Optics,* 2025/10/08 2025, doi: 10.1007/s12596-025-02919-w.

[130] J. F. Fennell Jr *et al.*, "Nanowire Chemical/Biological Sensors: Status and a Roadmap for the Future," *Angewandte Chemie International Edition,* vol. 55, no. 4, pp. 1266-1281, 2016/01/22 2016, doi: https://doi.org/10.1002/anie.201505308.

[131] X. Liu, S. Cheng, H. Liu, S. Hu, D. Zhang, and H. Ning, "A Survey on Gas Sensing Technology," *Sensors*, vol. 12, no. 7, pp. 9635-9665doi: 10.3390/s120709635.

[132] Y. Tu *et al.*, "Ammonia Gas Sensor Response of a Vertical Zinc Oxide Nanorod-Gold Junction Diode at Room Temperature," *ACS Sensors,* vol. 5, no. 11, pp. 3568-3575, 2020/11/25 2020, doi: 10.1021/acssensors.0c01769.

[133] H. Liu *et al.*, "Tin oxide films for nitrogen dioxide gas detection at low temperatures," *Sensors and Actuators B: Chemical,* vol. 177, pp. 460-466, 2013/02/01/ 2013, doi: https://doi.org/10.1016/j.snb.2012.11.051.

[134] D. Kumar *et al.*, "Effect of single wall carbon nanotube networks on gas sensor response and detection limit," *Sensors and Actuators B: Chemical,* vol. 240, pp. 1134-1140, 2017/03/01/ 2017, doi: https://doi.org/10.1016/j.snb.2016.09.095.

[135] P. Srinivasan, M. Ezhilan, A. J. Kulandaisamy, K. J. Babu, and J. B. B. Rayappan, "Room temperature chemiresistive gas sensors: challenges and strategies—a mini review," *Journal of Materials Science: Materials in Electronics,* vol. 30, no. 17, pp. 15825-15847, 2019/09/01 2019, doi: 10.1007/s10854-019-02025-1.

[136] S. Wicker, K. Großmann, N. Bârsan, and U. Weimar, "Co3O4—A systematic investigation of catalytic and gas sensing performance under variation of temperature, humidity, test gas and test gas concentration," *Sensors and Actuators B: Chemical,* vol. 185, pp. 644-650, 2013/08/01/ 2013, doi: https://doi.org/10.1016/j.snb.2013.05.057.

[137] P. M. Bulemo *et al.*, "Selectivity in Chemiresistive Gas Sensors: Strategies and Challenges," *Chemical Reviews,* vol. 125, no. 8, pp. 4111-4183, 2025/04/23 2025, doi: 10.1021/acs.chemrev.4c00592.

[138] A. Shrivastava and V. B. Gupta, "Methods for the determination of limit of detection and limit of quantitation of the analytical methods," *Chron. Young Sci,* vol. 2, no. 1, pp. 21-25, 2011.

[139] J. R. Saffell and N. A. Martin, "Measurements of the Limit of Detection for Electrochemical Gas Sensors," *Journal of Testing and Evaluation,* vol. 52, no. 5, pp. 2675-2684, 2024, doi: 10.1520/JTE20230675.

[140] Y. Niu *et al.*, "A Photovoltaic Self-Powered Gas Sensor Based on All-Dry Transferred MoS2/GaSe Heterojunction for ppb-Level NO2 Sensing at Room Temperature," *Advanced Science,* vol. 8, no. 14, p. 2100472, 2021/07/01 2021, doi: https://doi.org/10.1002/advs.202100472.

[141] B.-J. Kim and J.-S. Kim, "Gas sensing characteristics of MEMS gas sensor arrays in binary mixed-gas system," *Materials Chemistry and Physics,* vol. 138, no. 1, pp. 366-374, 2013/02/15/ 2013, doi: https://doi.org/10.1016/j.matchemphys.2012.12.002.

[142] V. E. Bochenkov and G. B. Sergeev, "Sensitivity, selectivity, and stability of gas-sensitive metal-oxide nanostructures," *Metal oxide nanostructures and their applications,* vol. 3, pp. 31-52, 2010.

[143] Y. Takahashi, M. Kanamori, A. Kondoh, H. M. Hideki Minoura, and Y. O. Yutaka Ohya, "Photoconductivity of Ultrathin Zinc Oxide Films," *Japanese Journal of Applied Physics,* vol. 33, no. 12R, p. 6611, 1994/12/01 1994, doi: 10.1143/JJAP.33.6611.

[144] S. Öztürk, N. Kılınç, İ. Torun, A. Kösemen, Y. Şahin, and Z. Z. Öztürk, "Hydrogen sensing properties of ZnO nanorods: Effects of annealing, temperature and electrode structure," *International Journal of Hydrogen Energy,* vol. 39, no. 10, pp. 5194-5201, 2014/03/26/ 2014, doi: https://doi.org/10.1016/j.ijhydene.2014.01.066.

[145] X.-T. Yin and X.-M. Guo, "Sensitivity and selectivity of (Au, Pt, Pd)-loaded and (In, Fe)-doped SnO2 sensors for H2 and CO detection," *Journal of Materials Science: Materials in Electronics,* vol. 25, no. 11, pp. 4960-4966, 2014/11/01 2014, doi: 10.1007/s10854-014-2258-7.

[146] M. Yadav, M. Kumar, S. Chaudhary, K. Yadav, and A. Sharma, "A Review on Chemiresistive Hybrid Zinc Oxide and Nanocomposites for Gas Sensing," *Industrial & Engineering Chemistry Research,* vol. 62, no. 29, pp. 11259-11278, 2023/07/26 2023, doi: 10.1021/acs.iecr.3c00242.

[147] K. X. Steirer *et al.*, "Ultrasonically sprayed and inkjet printed thin film electrodes for organic solar cells," *Thin Solid Films,* vol. 517, no. 8, pp. 2781-2786, 2009/02/27/ 2009, doi: https://doi.org/10.1016/j.tsf.2008.10.124.

[148] T. V. K. Karthik *et al.*, "Sprayed ZnO thin films for gas sensing: effect of substrate temperature, molarity and precursor solution," *Journal of Materials Science: Materials in Electronics,* vol. 31, no. 10, pp. 7470-7480, 2020/05/01 2020, doi: 10.1007/s10854-020-02987-7.

[149] R. Kumar, P. Ghosh, A. Gupta, H. Agrawal, and C. S. Prajapati, "Advancing stability enhanced hydrogen detection using Sn-doped ZnO thin films via thermally regulated zeolite humidity filtration," *Ceramics International,* vol. 52, no. 4, pp. 4399-4412, 2026/02/01/ 2026, doi: https://doi.org/10.1016/j.ceramint.2025.12.214.